Investigation of bone response to implant materials by electron microscopy and computer simulation

by

Hao Wang

Bachelor of Engineering, Materials Science and Engineering
Tsinghua University, 1996

Master of Engineering, Materials Science and Engineering
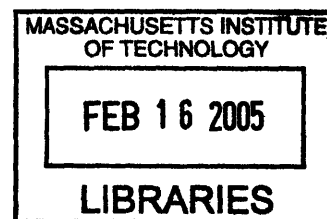Tsinghua University, 1998

Submitted to the Department of Materials Science and Engineering in Partial
Fulfillment of the Requirements for the Degree of

Doctor of Philosophy in Materials Science

at the

MASSACHUSETTS INSTITUTE OF TECHNOLOGY

SEPTEMBER 2004

Signature of Author..
Department of Materials Science and Engineering
August 31, 2004

Certified by...
Linn W. Hobbs
Professor of Materials Science and Professor of Nuclear Engineering
Thesis supervisor

Certified by...
W. Craig Carter
Lord Foundation Professor of Materials Science and Engineering
Thesis supervisor

Accepted by...
Carl V. Thompson II
Stavros Salapatas Professor of Materials Science and Engineering
Chair, Departmental Committee on Graduate Students

Abstract

Initial fixation with bone and the long term bone loss are two main problems associated with total hip replacement (THR), which are studied by electron microscope and computer simulation in this thesis.

Bare Titanium-6 wt% Aluminum- 4 wt% Vanadium (Ti64) implants, Ti64 implants with plasma-sprayed hydroxyapatite (PSHA), and Ti64 implants with electrochemically-deposited hydroxyapatite (EDHA) were implanted into canine trabecular bone for 6 hours, 7 days, and 14 days to study the initial bone formation on these implant materials. Scanning electron microscope (SEM) results showed that at 7 days PSHA had a higher bone apposition ratio than Ti64 and EDHA samples; however, at 14 days, the bone apposition on EDHA increased to be similar to PSHA, much higher than that on Ti64. By transmission electron microscope (TEM), a layer of new bone tissue was observed on PSHA coating surface; in contrast, no much bone was found on EDHA surface. At 14 days, substantial bone was found on both EDHA and EDHA coating surface.

Technetium-99m-methylene-diphosphonate (Tc-99m-MDP) labeling was used to quantify mineralization of cultures of MC3T3 osteoblast-like cells *in vitro* on tissue culture polystyrene (TCPS). The gamma signal from labeled samples was imaged with a gamma camera and compared with the calcium content in the same samples determined by inductively coupled plasma. The high correlation (0.88) between these two values validated that radiotracer uptake method as a quantitative analytical tool for certain mineralization studies *in vitro*. There was an association between mineralization and radionuclide uptake in the MC3T3 cultures on titanium alloy, but the attenuation of the gamma photons by the metal resulted in a less robust correlation. The results warrant implementation of this scintigraphic method for quantitative studies of osteoblast-mediated mineralization *in vitro*.

A 2-D truss finite element model is used to study the remodeling of trabecular bone. Using strain energy density (SED) as the optimization object and the trabecular width as the optimization variable, an optimal structure with minimum SED was achieved. This structure is similar to real bone in the dense outside, porous inside, and orientation of the trabeculae. The bone density distribution pattern also matched with previous result by other people. Different implants were introduced to simulate the replacement for the femoral head. It has been proved that the difference in Young's modulus between bone and implant materials is the main reason for the long-term bone loss (stress screening). This problem can be alleviated by proper implant design and resurfacing instead of replacing the whole femoral head.

Acknowledgement

It is impossible for me to finish my Ph.D. without the help from a lot of people--too many to list here. However, please remember, no matter if your name is here or not, your help and my appreciation are always in my heart, and won't change with time.

Professor Linn W. Hobbs, my advisor, for all your advice in my study and going over my thesis in both language and science. You let me know what the real meaning of research is.

Professor W. Craig Carter, my co-advisor, you not only teach me how to program, tackle hard problems, but also teach me how to be optimistic and amiable, which I know I cannot be as good as you are, but it is good enough to benefit me for the lifetime.

Professor Myron Spector, you opened the door of biomaterials for me, which made my life much harder. I don't regret but appreciate, for you pointed what I really like. You indeed are also my advisor.

Professor Ortiz for being in my thesis committee, reading my thesis, and giving helpful suggestions.

Prof. Sandra Burkett for bringing me to MIT and supporting me in the first year. You left MIT after I came here, and I wish that you are happy no matter where you are.

My collaborators, I hope you think our collaboration a happy one. Dr. Hu-Ping Hsu, for getting up at 5 am for all the animal experiments; I know doctors can get up early, but it was really hard for me; Dr. Zhou Xiang, for the processing of animal samples and electron microscope work; Dr. Bernd Kinner, for your patience on teaching me how to culture cells; Dr. Paulo Ferreiro, for your turning electron microscopy into an art instead of science only; Dr. Debbie Chachra, for sharing all the failure and success in cell cultures; and Dr. Noam Eliaz, for providing us the EDHA samples.

People in the CMSE EM center: Mike Frongillo, Patrick Boisvert, Anthony Garratt-Reed, for training me to use the facility there.

Lisa Mellen, Dr. Susan Woods, Professor Ken Czerwinski, and Professor Charlie Langmuir, for helping me on my ICP.

Tim McClure for teaching me the profilometer.

Kerri Cozine for providing me neonatal mice.

Table of Contents

6

List of Figures

List of Tables

Chapter 1 Introduction

1.1 Clinical background

During the last several decades, artificial joints have proven a successful treatment for primary and secondary osteoarthritis particularly of hip, knee, and shoulder joints[1]. Candidates for joint arthroplasty include patients who exhibit excessive pain of dysfunction in either the hip or knee due to fracture of the femoral head, arthritis, or other conditions[2, 3]. More than 500,000 joint replacements are performed each year in the United States alone, with many more hundreds of thousands being performed worldwide[4, 5]. Due to the change in demographics, the total demand will increase about 30% during the next 20 years[6].

Many devices have been proposed for repair or replacement of both the hip and the knee. The prosthetic design for the hip most commonly used today incorporates a ball component that is attached to the femur via a stem that is inserted into the marrow cavity, as shown in Figure 1-1. The most common attachment vehicle for total hip arthroplasty (THA) is poly-methylmethacrylate (PMMA), which serves as a "bone cement", providing mechanical fixation by both penetrating the interstices of the surrounding bone and adapting to surface features of the metal stem[7]. The overall clinical results in a large series of cemented THA and total knee arthroplasty (TKA) were good, with 5-10% risk of revision within 10 years after surgery. However, for young patients the risk of implant failure and revision of the prosthesis is unsatisfactorily high: rates of 20-25% have been experienced[1]. The cementless technique, which relies on biological fixation provided by insertion and initial press fit, followed by bone in-growth into a textured or porous implant surface, is an alternative that may prove to be more reliable. However, with respect to cementless femoral components for THA, it has been shown that thigh pain is a significant problem and that osteolysis around the implant may be present in up to 40% of cases within ten years after surgery[8]. In addition, retrieval studies have revealed that the

17

majority of femoral stems and acetabular components become fixed by fibrous tissue instead of bone ingrowth[9]. Thus, adjuvant therapies are called for in order to enhance bony implant fixation. Calcium phosphate based (Ca-P) coatings were introduced clinically for that specific purpose and with the intention of improving the survival rate of cementless joint prostheses.
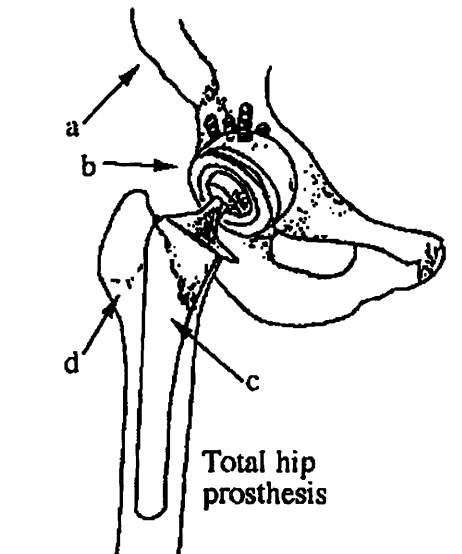
a: pelvis; b: acetabular component of hip prosthesis and prosthetic ball; c: prosthetic stem; d: femur.

Figure 1-1 Schematic drawing of cementless total hip replacement[2]

1.2 Hydroxyapatite coatings

While many calcium phosphate ceramics have been developed as bone bonding materials, the most common coating for orthopedic implants continues to be hydroxyapatite (HA). The nominal chemical composition of HA is $Ca_{10}(PO_4)_6(OH)_2$ (hexagonal crystal system, space group $P6_3/m$). It is the main inorganic component of bone and teeth.

In the 1970's, it was found that living bone can form a mechanical bond with sintered HA. However, the biomechanical properties of sintered HA are poor. Although a compressive strength of up to 600-700 MPa may be achieved, the tensile strength is only about 200-250 MPa, which makes HA unsuitable for load-

bearing application[10]. In 1987, de Groot et al. applied the technique of plasma spraying to deposit a thin, dense layer of HA onto a titanium substrate. It was demonstrated that HA coating had osteoconductive properties and the mechanical fixation of HA-coated implants was better than for uncoated implants during optimal surgical conditions[10-13]. The bonding strength between bone/implants is too great to be explained by mechanical bonding alone, which suggests that biological bonding is occurring at the interface[14].

Although HA-coated implants have gained wide acceptance in orthopedic surgery, the mechanisms leading to formation of new bone remains a matter of conjecture. Two theories exist in the literature. The first hypothesis suggests that a granular, afibrillar zone exists directly at the bone-implant surface, and bone-derived cells generate calcified afibrillar accretions that may act as a substratum conditioning layer prior to overt bone formation. This extracellular matrix layer, which is less than 1 μm thick and contains calcium, phosphorous, and sulfur, is analogous to that of cement lines formed at discontinuities in natural bone tissue[15]. The second hypothesis suggests that an unmineralized collagen fiber matrix is first laid down at the implant-bone interface and subsequently is mineralized during osteogenesis. This fiber matrix layer is not encapsulating fiber, but rather thin area with apparent potential to undergo remodeling or mineralization. A thin 20-50 nm electron-dense deposit may exist and separate this mineralized matrix from the implant[16-18].

The nature of the processes that underlie the formation of these interfacial structures is unknown and, therefore, it is unclear whether they are related to early bone formation. In order to develop better understanding of the mechanism of new bone formation, both *in vivo* and *in vitro* experiments were performed in this study. Canine models were used for *in vivo* studies, using the protocols established in the previous study in our group[19]. HA-coated Ti-6Al-4V rods were implanted in the proximal and distal femora and proximal tibiae of dogs for different time periods and recovered after sacrifice. Scanning electron microscopy (SEM) and transmission electron microscopy (TEM) were used to

19

establish in these samples the apposition ratio of new bone to different implant surfaces and to study the ultrastructure between the implant/bone interfaces.

In vitro environments, that can be designed for different purposes and easily controlled, avoid the complexity associated with *in vivo* environment. In this study, bone-forming cells were also cultured on different implant materials. These cells were characterized by their synthesis of a type I collagen matrix that mineralized. The efficiency of a biomaterial could thus be characterized, in part, by the amount of mineral produced by the cells cultured on its surface. However, until now, there has been no ideal method to quantify the mineral produced by these cells. One goal of this study was to use Tc-99m-MDP radioactive labeling as a tool to quantify these minerals, in order to assist the understanding of bone cell mineralization kinetics and comparison between different implant materials.

1.3 Bone stress shielding

Another important problem associated with implant materials is bone stress shielding: stresses on the leg are not conducted from the implant to the surrounding bone in a physiological fashion. This problem is mainly caused by the difference of elastic modulus between implants and human bone: the most common stem materials are titanium-6 wt% aluminum-4 wt% vanadium (Ti-6Al-4V) and cobalt-chromium alloys, with Young's moduli of 105 and 230 GPa, respectively. In contrast, the cortical bone surrounding the implant has a modulus of 30 GPa; the trabecular bone at the ends of the femur has a modulus of 3 GPa. The consequent diminished mechanical stress on the bone tissue results in reduced activity of osteoblasts, the cells that are responsible for bone formation. In the presence of normal bone resorption by osteoclasts, this reduced osteoblastic activity results in a net loss of bone mass. The decrease in bone density puts the patient at the risk for both fracture and prosthesis failure, which would necessitate a revision arthroplasty to replace the prosthesis[2].

Evidently, orthopedic surgery will be greatly served if the adaptive changes around prostheses could be predicted. It is well known that bone can

modify its microstructure in response to local mechanical loading conditions (bone remodeling). Properly designed prostheses can create compatible stresses in the surrounding bone, and thereby utilize the remodeling potential of trabecular bone to achieve implant fixation. The microscopic stress patterns in bone/prosthesis structures are determined by the external loading conditions, and the geometry and material properties of the bones and the prosthesis. Given adequate quantitative descriptions of loading, geometry, material properties and boundary conditions in the structure, the degree of bone-stress abnormality relative to the intact bone can be predicted by finite element method (FEM)[20].

Using an algorithm that is based on the empirical observation of Wolff's law, a two-dimensional FEM model of bone was constructed for this study. Driven by the nonuniformity of the strain energy density (SED), the system evolved towards an optimal structure by proper mathematical algorithm. This optimal structure is similar to real bone with its dense outside shell and porous interior, which validates the further use of this model for implant study. The influence of different factors for implantation: the material's Young's modulus, the implant design, and the bone apposition ratio at implant surface are discussed in the context of this model.

1.4 Future: Tissue Engineering

Although joint replacement surgery for remediation of rheumatoid arthritis, osteoarthritis and osteoporosis has significantly improved the quality of life for many, biomaterial failure and incompatibility due to wear, corrosion or "stress shielding" have resulted in complications including detachment of the stem coating and/or fracture of the cement–stem or cement–bone interface[21]. Clearly, the next generation of bone replacement materials will need to more biologically and mechanically resemble real bone tissues. This major clinical requirement has stimulated interest in developing new therapies that involve bone regeneration and has led to the idea of bone tissue engineering: the application of scientific principles to the design, construction, modification and growth of living tissues using biomaterials, cells and factors, alone or in combination[22, 23].

A common strategy employed in bone tissue engineering as well as other tissues includes the *in vitro* expansion of stem cells or other progenitor cells into functionary tissue cells. Multipotential stromal stem cells located within the bone marrow can differentiate into fibroblastic, osteogenic, adipogenic and reticular cells[24]. Culture-expanded bone marrow cells can heal a segmental bone defect following reimplantation and can give rise to osteogenic tissue within diffusion chambers in a variety of animal species [25-27]. Other candidates for cells used in bone tissue engineering include collagenase-digested osteoblast-liked cells from fetal or neonatal mouse calvarial[28], cloned osteoblast-like cell lines[29], and osteoblast-like cells from organ cultures[30]. Cultured in 3-D matrices with/without growth factors, these cells can also form a structure similar to bone tissue comprising mineralized collagen.

Bone tissue engineering is attractive because it could provide suitable, efficacious alternative therapies for orthopedic applications. Current clinical applications include the augmentation of bone stock, in maxillo-facial surgery as well fracture and non-union fractures. However, it is clear that current

achievement is still unlikely to reach clinical evaluation for the most basic of structural, biological or safety issues and that this discipline is still in its infancy. Paramount in each case will be the need to reintroduce an appropriate angiogenic response within the construct from, and integrated, with the host tissue. The next few years will undoubtedly see dramatic technical innovations, doubtless accompanied by media and market hyperbole.

1.5 References

1. Malchau, H., P. Herberts, and L. Ahnfelt, *Prognosis of total hip replacement in Sweden. Follow-up of 92,675 operations performed 1978-1990.* Acta Orthop Scand, 1993. **64**(5): p. 497-506.

2. Harris, W.H. and C.B. Sledge, *Total hip and total knee replacement (1).* N Engl J Med, 1990. **323**(11): p. 725-31.

3. Harris, W.H. and C.B. Sledge, *Total hip and total knee replacement (2).* N Engl J Med, 1990. **323**(12): p. 801-7.

4. Langer, R. and J.P. Vacanti, *Tissue engineering.* Science, 1993. **260**(5110): p. 920-6.

5. Overgaard, S., *Calcium Phosphate coating for fixation of bone implants.* Acta Orthop Scand, 2000. **71**(Suppl. 297): p. 1-74.

6. Overgaard, S., H.M. Knudsen, L.N. Hansen, and N. Mossing, *Hip arthroplasty in Jutland, Denmark. Age and sex-specific incidences of primary operations.* Acta Orthop Scand, 1992. **63**(5): p. 536-8.

7. Spector, M., *Prostheses: materials, design, and strategies for implant fixation, Orthopedic knowledge update 3.* 1990, Amer Acad Orthop Surg. p. 185-205.

8. Berry, D.J., W.S. Harmsen, D. Ilstrup, D.G. Lewallen, and M.E. Cabanela, *Survivorship of uncemented proximally porous-coated femoral components.* Clin Orthop, 1995(319): p. 168-77.

9. Collier, J.P., T.W. Bauer, R.D. Bloebaum, J.D. Bobyn, S.D. Cook, J.O. Galante, W.H. Harris, W.C. Head, M.J. Jasty, M.B. Mayor, and et al., *Results of implant retrieval from postmortem specimens in patients with well-functioning, long-term total hip replacement.* Clin Orthop, 1992(274): p. 97-112.

10. de Groot, K., R. Geesink, C.P. Klein, and P. Serekian, *Plasma sprayed coatings of hydroxylapatite.* J Biomed Mater Res, 1987. **21**(12): p. 1375-81.

11. Cook, S.D., K.A. Thomas, J.F. Kay, and M. Jarcho, *Hydroxyapatite-coated titanium for orthopedic implant applications.* Clin Orthop, 1988(232): p. 225-43.

12. Cook, S.D., K.A. Thomas, J.F. Kay, and M. Jarcho, *Hydroxyapatite-coated porous titanium for use as an orthopedic biologic attachment system.* Clin Orthop, 1988(230): p. 303-12.

13. Kay, J.F., T.S. Golec, and R.L. Riley, *Hydroxyapatite-coated subperiosteal dental implants: design rationale and clinical experience.* J Prosthet Dent, 1987. **58**(3): p. 339-43.

14. Geesink, R.G., *Hydroxyapatite-coated total hip prostheses. Two-year clinical and roentgenographic results of 100 cases.* Clin Orthop, 1990(261): p. 39-58.

15. Davies, J.E., R. Chernecky, B. Lowenberg, and A. Shiga, *Deposition and Resorption of Calcified Matrix Invitro by Rat Marrow-Cells.* Cells and Materials, 1991. **1**(1): p. 3-15.

16. Linder, L., T. Albrektsson, P.I. Branemark, H.A. Hansson, B. Ivarsson, U. Jonsson, and I. Lundstrom, *Electron microscopic analysis of the bone-titanium interface.* Acta Orthop Scand, 1983. **54**(1): p. 45-52.

17. Steflik, D.E., A.L. Sisk, G.R. Parr, L.K. Gardner, P.J. Hanes, F.T. Lake, D.J. Berkery, and P. Brewer, *Osteogenesis at the dental implant interface: high-voltage electron microscopic and conventional transmission electron microscopic observations.* J Biomed Mater Res, 1993. **27**(6): p. 791-800.

18. Steflik, D.E., R.S. Corpe, F.T. Lake, T.R. Young, A.L. Sisk, G.R. Parr, P.J. Hanes, and D.J. Berkery, *Ultrastructural analyses of the attachment (bonding) zone between bone and implanted biomaterials.* J Biomed Mater Res, 1998. **39**(4): p. 611-20.

19. Benezra, V.I., Electron microscopic investigation of interfaces in materials for orthopedic applications, Thesis Ph.D. --Massachusetts Institute of Technology Dept. of Materials Science and Engineering 1998.

20. Huiskes, R., H. Weinans, H.J. Grootenboer, M. Dalstra, B. Fudala, and T.J. Slooff, *Adaptive bone-remodeling theory applied to prosthetic-design analysis.* J Biomech, 1987. **20**(11-12): p. 1135-50.

21. Spector, M., *Biomaterial failure.* Orthop Clin North Am, 1992. **23**(2): p. 211-7.

22. Nerem, R.M., *Cellular engineering.* Ann Biomed Eng, 1991. **19**(5): p. 529-45.

23. Rose, F.R. and R.O. Oreffo, *Bone tissue engineering: hope vs hype.* Biochem Biophys Res Commun, 2002. **292**(1): p. 1-7.

24. Bianco, P., M. Riminucci, S. Gronthos, and P.G. Robey, *Bone marrow stromal stem cells: nature, biology, and potential applications.* Stem Cells, 2001. **19**(3): p. 180-92.

25. Kadiyala, S., R.G. Young, M.A. Thiede, and S.P. Bruder, *Culture expanded canine mesenchymal stem cells possess osteochondrogenic potential in vivo and in vitro.* Cell Transplant, 1997. **6**(2): p. 125-34.

26. Gundle, R., C.J. Joyner, and J.T. Triffitt, *Human bone tissue formation in diffusion chamber culture in vivo by bone-derived cells and marrow stromal fibroblastic cells.* Bone, 1995. **16**(6): p. 597-601.

27. Nakahara, H., S.P. Bruder, S.E. Haynesworth, J.J. Holecek, M.A. Baber, V.M. Goldberg, and A.I. Caplan, *Bone and cartilage formation in diffusion chambers by subcultured cells derived from the periosteum.* Bone, 1990. **11**(3): p. 181-8.

28. Peck, W.A., S.J. Birge, Jr., and S.A. Fedak, *Bone Cells: Biochemical and Biological Studies after Enzymatic Isolation.* Science, 1964. **146**: p. 1476-7.

29. Kodama, H.A., Y. Amagai, H. Koyama, and S. Kasai, *A new preadipose cell line derived from newborn mouse calvaria can promote the proliferation of pluripotent hemopoietic stem cells in vitro.* J Cell Physiol, 1982. **112**(1): p. 89-95.

30. Jones, S.J. and A. Boyde, *The migration of osteoblasts.* Cell Tissue Res, 1977. **184**(2): p. 179-93.

Chapter 2 *In vivo* experiments

2.1 Introduction

Titanium and its alloys are widely used as implant materials because of their excellent mechanical properties and chemical stability in physiological environment. However, the difficulty in bonding with living bone directly and the release of corrosion product into surrounding tissues greatly restrict their application. A thin coating of hydroxyapatite (HA) is normally applied on the surface of titanium and its alloys, to take advantage of both the biocompatibility of HA and the strength of metals. Since its introduction in the 1980s, HA-coated implants have gained wide acceptance in orthopedic surgery[1]. It was demonstrated that HA had osteoconductive properties and the mechanical fixation of HA-coated implants was better than uncoated implants during optimal surgical conditions[2]. The research literature also supports the conclusion that the early bone growth is improved by HA-coatings[3].

However, the mechanism of how bone adherence to the HA-implants, as well as to other implants, is not yet clearly understood. Study is mainly impeded by the complexity of the implant/bone systems. The implants can vary greatly in terms of their surface chemical and physical properties: even for HA coatings, because of the different techniques and processing conditions used, they can have very different phase purity, crystal size, and surface roughness, all of which can influence new bone formation. As well, the bone side can change with: (1) the animal species; (2) the implantation sites; and (3) age and gender of the animal. The different sample processing and analysis technologies and human factors introduced by different research groups further complicate the situation. So it is not surprising that many research results are quite different and sometimes even contradictory. For example, even the underlying mechanisms leading to new bone formation still remains in debate. Two different theories exist in the literature. The first hypothesis suggests that a granular, afibrillar zone exists directly at the bone-implant surface, and bone-derived cells generate

calcified afibrillar accretions that may act as a substratum conditioning layer prior to overt bone formation. This extracellular matrix layer, which is alleged to be less than 1 μm thick and contains calcium, phosphorous, and sulfur, is analogous to that of cement lines formed at discontinuities in natural bone tissue[4]. The second hypothesis suggests that an unmineralized collagen fiber matrix is first laid down at the implant-bone interface and subsequently is mineralized during osteogenesis. This fiber matrix layer is not encapsulating fiber, but rather thin region with apparent potential to undergo remodeling or mineralization. An even thinner 20-50 nm electron-dense deposit may exist and separate this mineralized matrix from the implant[5-7]. Clearly, more work has needed to be done to fundamentally understand the bone/implant interface, so that better understanding on the bone formation mechanisms on implants can be obtained, which could further help the design of better implants.

2.1.1 HA coating technology

Plasma-spraying is still the most popular technology in industry for preparing HA coatings on titanium alloy and other metal implants. A plasma is a high-energy, high-temperature (>20,000 K) gaseous phase with an appreciable content of ionized atoms. De groot first used this technology to prepare HA coatings on titanium implant[8]. For coating, a plasma is generated in a small cylindrical chamber with an anode at one end and a cathode at the other. As electrons are accelerated through the chamber, they collide with gas atoms which are being pumped into it, ionizing the atoms. The ionized atoms move towards the anode, and when the plasma emerges, a powder is injected into it. The plasma both partially melts the particles and propels them towards the substrate, where they splat and cool[9]. The thickness of the coating obtained by this technology is normally around 40~200 μm.

However, plasma spraying is a high-temperature and line-of-sight process. Potential problems of this technology include intense heat on substrates, residual thermal stresses in coatings, and the impossibility of coating complex shapes with internal cavities[10]. Many other techniques have been explored to solve

these problems[11], such as ion-beam deposition[12], chemical deposition[10], metal-organic CVD[13], sol-gel[14], pulsed laser deposition[15], and electrophoresis[16]. Electrochemical deposition is one of the promising new methods[17, 18]. Compared to plasma spraying, the advantages of electrochemical deposition include good control of composition and structure of the coatings due to the relatively low processing temperature, the ability to deposit on porous or complex shapes, etc. Deposition of different calcium phosphates, including brushite[19], hydroxyapatite[17], and a mixture of them has been reported. The structure of the coating can be controlled by changing the composition, pH value, and temperature of the electrolyte solution. For example, a nano-structured hydroxyapatite coating has been reported to deposit from electrochemical formation[20].

2.1.2 Bone mineralization mechanism

Bone, despite its different shapes and internal structures, is made of the same material, a composite of hydroxyapatite (70 wt. %) and type I collagen (20 wt. %). Besides water (9 wt. %), other proteins, polysaccharides, and lipids are also present in small quantities. Collagen fibers cross-link with each other to form the matrix and the 3-D scaffold for bone. The HA crystals, present in the form of plates, are about 40–60 nm long, 20 nm wide, and 1.5–5 nm thick. They are deposited close to parallel with the collagen fibers, such that the [001] crystalline direction is along the long axis of the fiber[21-23]. It is worth mentioning that the mineral phase present in the bone is not a discrete aggregation of the HA crystals. It is rather made of a continuous phase which is evidenced by a very good strength of the bone after a complete removal of the organic phase[21].

Type I collagen, which comprises about one third of the total protein in a human, is the prominent member of the collagen family, which has more than 20 members. The key feature for a collagen is the presence of continuous or interrupted sequences in the individual polypeptide chains of repeated $(G-X-Y)_n$ amino acid sequence domains, in which G is glycine while X and Y maybe any amino acids. These domains on one polypeptide chain interact with similar

domains on two additional chains to form compound triple-helical units with characteristic "collagen fold". In bone, collagen molecules are secreted from osteoblast in the form of triple-helices and then cross-link with each other to form fibrils and further into higher structure. The length of a single collagen molecule is only 300 nm and width 1.5 nm, but the collagen fibers formed in this way can be as long as several tens of millimeters and as wide as 500 μm.

The process by which collagen matrix becomes mineralized, or how the HA deposits on collagen matrix, is very complicated, and current understanding of it is still very limited. Many studies have shown that a collagen fibril matrix by itself doesn't have the capacity to induce mineralization from a solution of calcium and phosphate ions at the physiological pH, concentration, and temperature. It is generally believed that many proteins, such as sialoprotein and osteopontin[24], osteocalcin[25], and fibronectin[26], are very important in this process. These proteins can incorporate into collagen matrix and then control the nucleation and growth of HA crystal through electronic charge, morphology match, and other factors. However, the detailed underlying mechanism is not yet clearly understood, and no direct experimental confirmation of mechanism has been found. One possible reason is that the control is not by a single protein but by the cooperative action of many proteins together. The separation of these proteins and duplication of their effects *in vitro* has not been fully achieved.

2.2 Materials and methods

2.2.1. Materials

Ti-6Al-4V ELI grade (ASTM F136-92) rod 3/16 inch (4.76 mm) in diameter was purchased from Titanium Industries, Inc., (Parsippany, NJ). This rod was machined into 10.0 mm long rods for further processing.

30 rods were plasma sprayed with hydroxyapatite (HA) by Bio-Coat, Inc., (Southfield MI) except for 2 mm left at one end, which was left uncoated. Hereafter these samples will be called as PSHA.

30 rods were electrochemically deposited with HA by Dr. Noam Eliaz at Tel Aviv University, Israel. The detailed process can be found in Appendix A. Hereafter these samples will be called EDHA.

30 rods were kept as-machined. Hereafter these samples will be called Ti64.

The near-surface phase compositions of these samples were studied by powder X-ray diffractometry (8-KW rotating-anode Cu source, 11-cm diameter powder diffractometer, Rigaku, Japan). The surface morphology was studied by an environmental scanning electron microscope (ESEM, XL30, FEI/Philips, Hillsboro, OR), and the surface roughness was studied with a surface profilmeter (P-10, Tencor, San Jose, CA). The solubilities of the coatings were tested by immersing a sample into 20 ml of distilled-water at room temperature. At 1, 24, 48, 72, 216, and 240 hours, 1 ml of solution was taken out at each time point and 1 ml of distilled water was added to keep the total volume of solution always at 20 ml. The 1 ml solution was diluted to 10 ml by distilled-water and the calcium concentration was measure by use of a direct-current plasma-atomic emission spectrometer, DCP-AES (SpectraSpan IIIA, Applied Research Laboratories Inc., Valencia, CA).

31

2.2.2. Sterilization

All the 90 rods were sealed in sterilization bags separately and sterilized by ethylene oxide at room temperature at Brigham & Women's hospital (Boston, MA), and then left at least 2 days for aeration before implantation.

2.2.3. Surgery

Samples were implanted for three different periods before sacrificing the animal for further analysis: 6 hours, 7 days, and 14 days, respectively. At each time point, there were 7 samples for TEM/SEM preparation for PSHA and EDHA materials groups and 6 samples for Ti64, so in total 60 samples were investigated in the animal study.

All surgeries were conducted at the animal facility center of the Veteran Administration Hospital (Boston). Permission from the Institutional Animal Care and Use Committee (IACUC) was obtained, and the NIH guidelines for the care and use of laboratory animals (NIH Publication #85-23 Rev. 1985) were observed.

All samples were implanted in the proximal and distal femora and proximal tibiae of the back legs of adult mongrel dogs (60-80 lbs.). Three drill holes were made: 1) an intramedullary drill hole, 4.7 mm in diameter and 20 mm deep (for 2 samples), was made at the trochanteric fossa of the proximal femur; 2) a drill hole of the same size (for 2 samples) was made in the distal femur, 10 mm proximal and 5 mm anterior to the femoral insertion of the MCL, and 3) a drill hole of 4.7 mm in diameter and 15 mm deep (for 1 sample) was made in the proximal tibia, 15 mm distal to the tibial plateau and 25 mm posterior to the tibial tuberosity. Two such surgeries were carried out on each dog: the first one was on the right side, while the second surgery on the left side was at least 7 days after the first one; all animals were sacrificed 7 or 14 days after the first surgery, as shown in Table 2-1 (the number of samples in parentheses).

32

Table 2-1 Surgical implantation of samples in canine model

		Proximal femora	Distal femora	Proximal tibiae
Dog 1	surgery 1	Ti14d(2)	Ti14d(2)	Ti14d(1)
	surgery 2	Ti6h(2)	Ti6h(2)	Ti6h(1)
Dog 2	surgery 1	PSHA14d(2)	PSHA14d(2)	PSHA14d(1)
	surgery 2	PSHA6h(2)	PSHA6h(2)	PSHA6h(1)
Dog 3	surgery 1	EDHA14d(2)	EDHA14d(2)	EDHA14d(1)
	surgery 2	EDHA7d(2)	EDHA7d(2)	EDHA7d(1)
Dog 4	surgery 1	PSHA14d(2)	EDHA14d(2)	Ti14d(1)
	surgery 2	PSHA7d(2)	EDHA7d(2)	Ti7d(1)
Dog 5	surgery 1	Ti7d(2)	Ti7d(2)	Ti7d(1)
	surgery 2	EDHA6h(2)	EDHA6h(2)	EDHA6h(1)
Dog 6	surgery 1	PSHA7d(2)	PSHA7d(2)	PSHA7d(1)
	surgery 2	EDHA6h(2)	PSHA6h(2)	Ti6h(1)

PSHA14d: PSHA samples, 14 days; PSHA7d: PSHA samples, 7 days; PSHA6h: PSHA samples, 6 hours.

Ti14d: Ti64 samples, 14 days; Ti7d: Ti64 samples, 7 days; Ti6h: Ti64 samples, 6 hours.

EDHA14d: EDHA samples, 14 days; EDHA7d: EDHA samples, 7 days; EDHA6h: EDHA samples, 6 hours.

2.2.4 SEM

SEM was used to study bone/implant interface morphology, by improving the protocols established in the previous study in our group[22]. The main focus of this SEM study was the new bone apposition ratio for different implants.

After sacrifice, tissues containing samples for SEM preparation were placed in 0.1M sodium cacodylate-buffered 4% paraformaldehyde and 2% glutaraldehyde solution. Then these tissues were trimmed using a coping saw and a ceramic cutoff wheel until the tissue around the rods was about 1-2 mm thick. The trimmed samples were fixed in the same buffered solution for 24 hours under vacuum at 4 °C. Next, the samples were washed by 0.1 M sodium cacodylate buffer solution twice for 10 minutes to remove the fixatives and then stored in such a solution at 4 °C overnight. The samples were subsequently fixed in 1% osmium tetraoxide aqueous solution for 4 °C at 2 hours. After rinsing in de-ionized water, the samples were dehydrated through a series of 50%, 75%, 95%, 100%, and 100% ethanol water solutions for 15 minutes each. The samples were agitated in 1:3, 1:2, 1:1, and 2:1 ratios of Spurr's resin dissolved in ethanol for 24 hours each and then vacuum infiltrated with pure Spurr's resin for 24 hours. They were then embedded in fresh Spurr's resin for 24 hours at 60 °C. The Spurr's resin was purchased from Ted Pella, Inc. (Redding, CA) and prepared with 10 g VCD, 4.5 g DER-736, 26 g NSA, and 0.4 g DMAE. The stiffness of the sample could be adjusted by changing the amount of DER-736.

After the Spurr's resin was totally cured, the embedded samples were cut into 0.5 mm thick slices with a slow speed diamond saw. All slices were ground on 1200 grit silicon carbide paper and then polished using 5 μm alumina paste and then 0.06 μm colloidal alumina in water. The polished specimens were subsequently sputter-coated with a thin layer (about 10 nm) of carbon and observed in an environmental SEM (ESEM, XL30, FEI/Philips, Hillsboro, OR).

Micrographs were recorded around each implant by ESEM with about 100X magnification, and for each implant there were about 20 such pictures. The

34

images taken by ESEM were stored in digital format with a 1424 X 968 byte dimension. The surface apposition ratio was calculated using Photoshop (Adobe, San Jose, CA) software from these images. A square grid was imposed on every image, and the size of grid squares was selected such that there were at least 30 squares at the bone/implant interface in each image. The apposition ratio in each image was calculated as the number of grid square at the bone/implant interface containing bone divided by the total number of grid squares at the interface. The apposition ratio for this implant was taken as the average ratio for all interface images of this implant.

2.2.5 TEM

The TEM samples followed the same fixation, dehydration, embedding, and slicing methods used for SEM samples.

After cutting into thin slices, samples were freeze-fractured to remove the titanium alloy rod. To introduce fracture, a 35 mm Petri dish was filled with liquid nitrogen, and the samples were then chilled in the liquid nitrogen pool in the dish for two minutes. Since titanium alloy has a much higher thermal expansion coefficient, a high thermal stress was produced at the metal/coating interface, which caused cracks to occur along this interface. Observation under a light microscope ensured that the coating/bone interface was maintained intact. After removing the titanium, the samples were embedded in Spurr's resin in BEEM vials (Ted Pella) under the same conditions used above.

The vials were then carefully removed from the outside of the sample, and the sample tip was trimmed to a 1 mm square to expose the coating/bone interface. At first, a thick section, about 500 nm thick, was cut with an ultramicrotome using a diamond knife, stained with methylene blue, and observed under a light microscope to confirm that the coating/bone interface was intact. Then "silver-to-gold" sections (60~80 nm thick) were cut via the same ultramicrotome, collected on parlodion-coated grids (Ted Pella) and air-dried. Some samples were stained in 2% uranyl citrate in 50% alcohol-water solution

for 2 hours and then in lead citrate aqueous solution for 30 minutes, to induce mass-thickness contrast in TEM. The other samples were left unstained for diffraction contrast study. The samples were initially screened in a JEOL 200CX TEM operated at 200 kV. If both the coating and some apposing tissue were visible in the TEM, the microtomed samples were further viewed in JEOL 2000FX or JEOL 2010 instruments with higher resolution capability. Elemental analysis was performed using an energy-dispersive X-ray detector attached to the 2010 TEM machine.

2.3 Coating Characterization

Comparison to the JCPDS standard x-ray diffraction file of HA (#09-0432) confirmed that both coatings were substantially composed of crystalline hydroxyapatite (Figure 2-1). The diffraction patterns were also compared to JCPDS files of other calcium phosphates; however, only HA could be identified. The crystallinity of HA coatings was analyzed by JADE software (Rigaku, Tokyo, Japan). A JADE analysis of the different pattern profiles estimated amorphous content about 10% for the PSHA and less than 5% for the EDHA coatings. The Bragg peaks from the titanium substrate were also found in both patterns. In the pattern for EDHA, the strong Bragg peaks were from the titanium substrate, while in the PSHA spectrum, the titanium Bragg peaks were much weaker than those of HA coating, because the coating thickness of EDHA was much thinner than that of PSHA, as established by ESEM (Figure 2-2 and Figure 2-3). In these ESEM micrographs, it was found that the thickness of EDHA coating was only about 5 μm. Higher magnification images (10,000X) showed that the EDHA coatings had two distinct layers. The first layer (about 500 nm) close to the titanium substrate was dense and uniform. The second layer was composed of crystals with different sizes: many of them were very tiny, however, some large ones grew through the whole coating layer (Figure 2-2). The thickness of PSHA coating was about 50 μm. Pores found in the PSHA coatings were as large as 5 μm (Figure 2-3). A crack between EDHA coating and the titanium substrate was also found in Figure 2-2. By contrast, PSHA coatings remained well attached to

36

the substrate. The bonding strength of EDHA apparently was lower than that of PSHA, even though the EDHA coating was much thinner.

The surface morphologies of these two coatings are shown in Figure 2-4. EDHA coatings were characterized by individually resolvable hydroxyapatite crystallites, with a plate-like shape, of typical width around several μm and thickness less than 1 μm, very similar to the hydroxyapatite crystals found in hydroxyapatite chemically-deposited at room temperature[27]. The morphologies suggest nucleation and growth of HA platelet crystallites from the electrolyte solution. An independent analysis by the collaborator who provided the EDHA coatings also confirmed that the EDHA coatings were highly crystalline (Dr. Noam Eliaz, private communication). The surface of PSHA showed a dramatically different morphology: large globules appeared at the surface and no HA crystallites were resolvable or found in PSHA coatings, suggesting that individual molten splats solidified as units with at least partly crystalline character (Figure 2-4(b)). The size of the surface globules ranged from several micrometers to about 100 nm. Few cracks were found on the surface, and the PSHA coating was much denser than the EDHA coating. The surface roughnesses (R_a) for these two coatings, measured by surface profilmeter, were found to be 480 ± 120 nm (EDHA) and 1.3 ± 0.4 μm (PSHA).
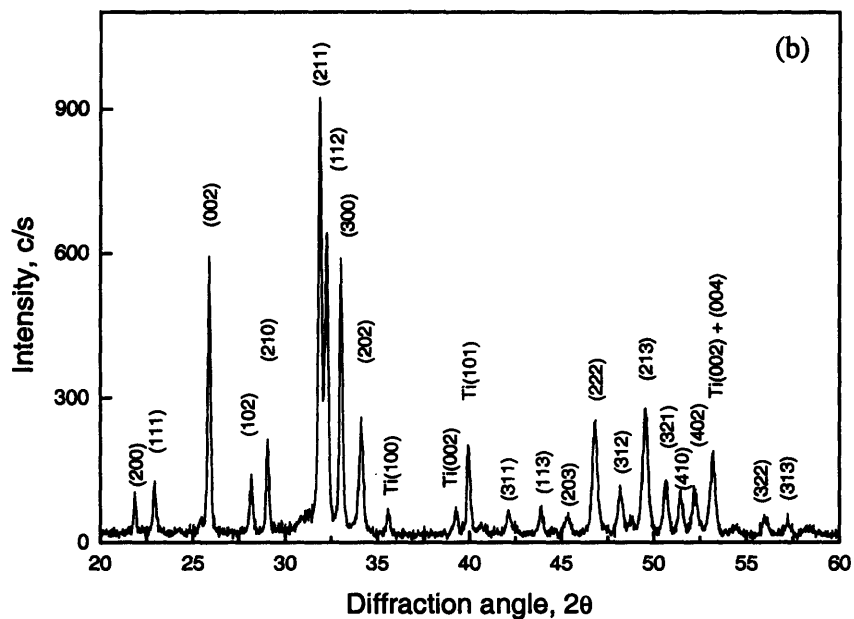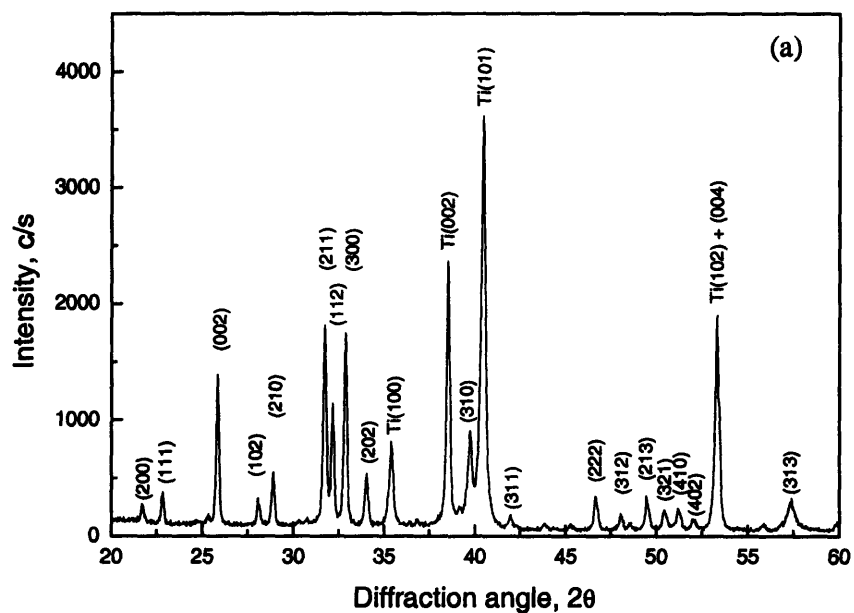
Figure 2-1 X-ray diffraction spectrum for (a) EDHA and (b) PSHA coatigs
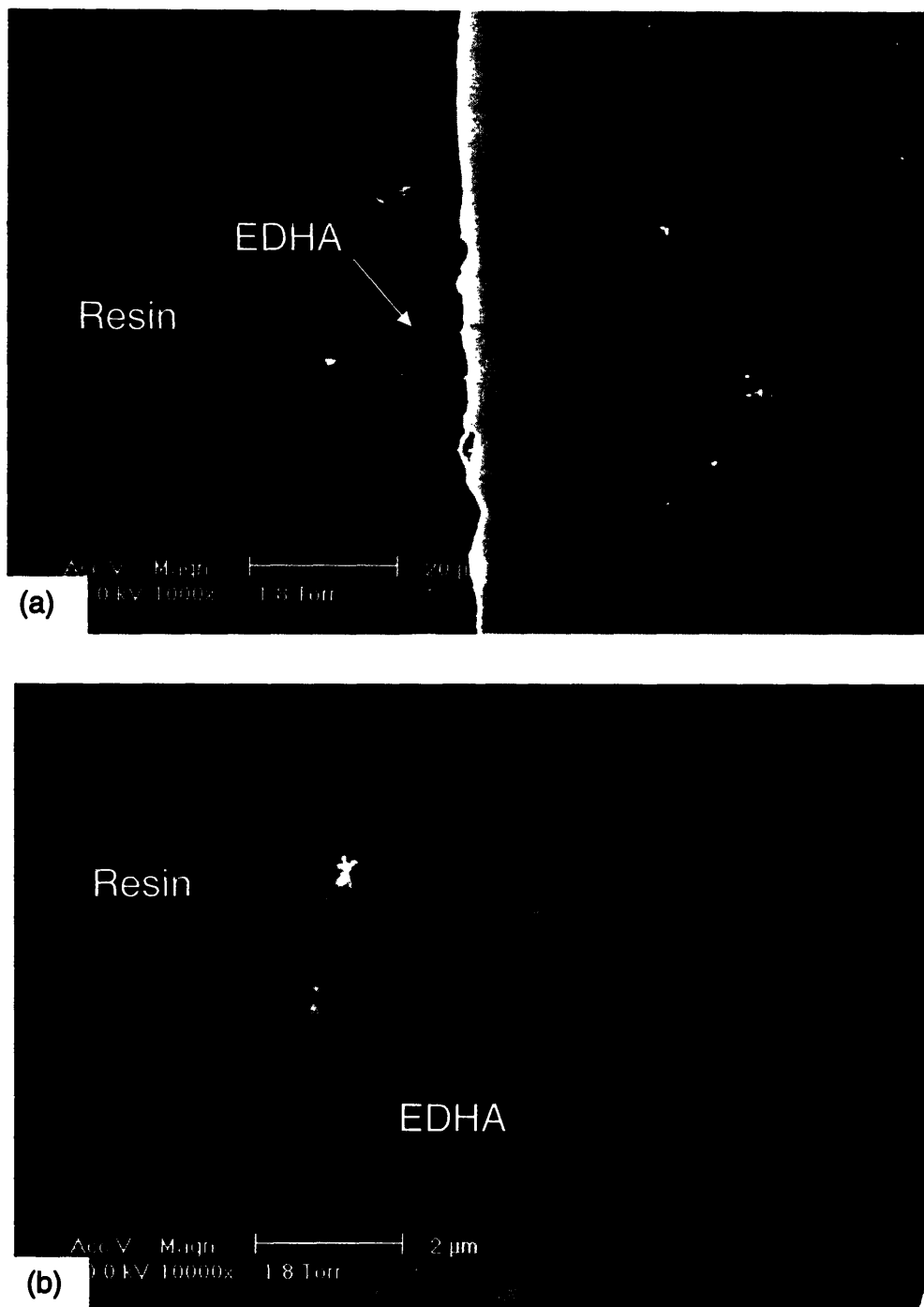
Figure 2-2 ESEM images from a cross section through EDHA coating: (a) 1,000X, (b) 10,000X

Resin

PSHA

Acc V Spot Magn   Det WD ├———————┤ 20 µm
(a) 0 kV 3.0   800x   GSE 12.4 1.3 Torr

Resin

PSHA

Acc V Spot Magn   Det WD ├———————┤ 10 µm
(b) 0 kV 3.0 2000x   GSE 10.5 1.3 Torr
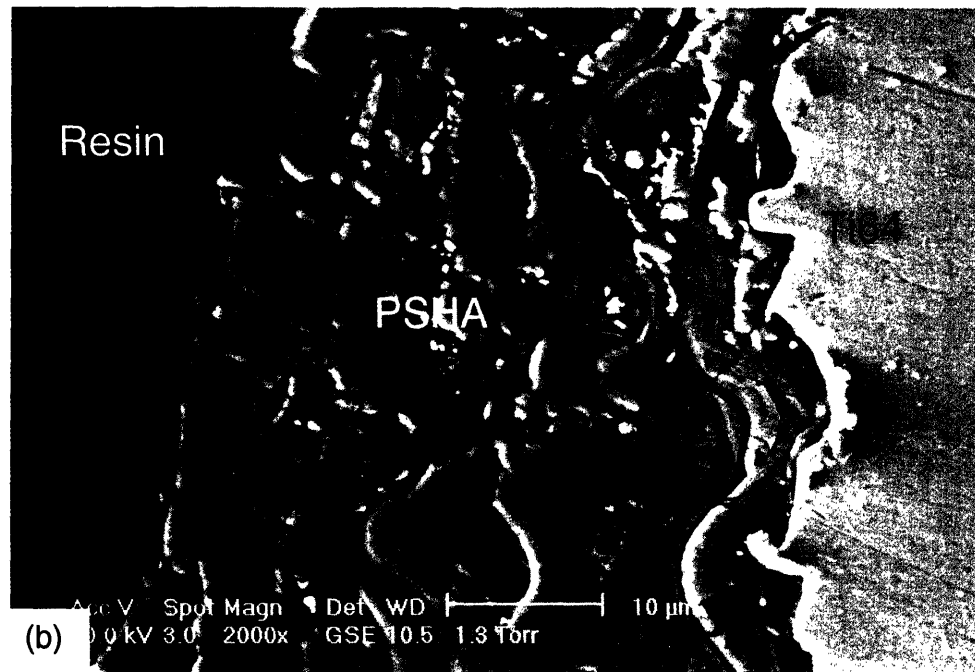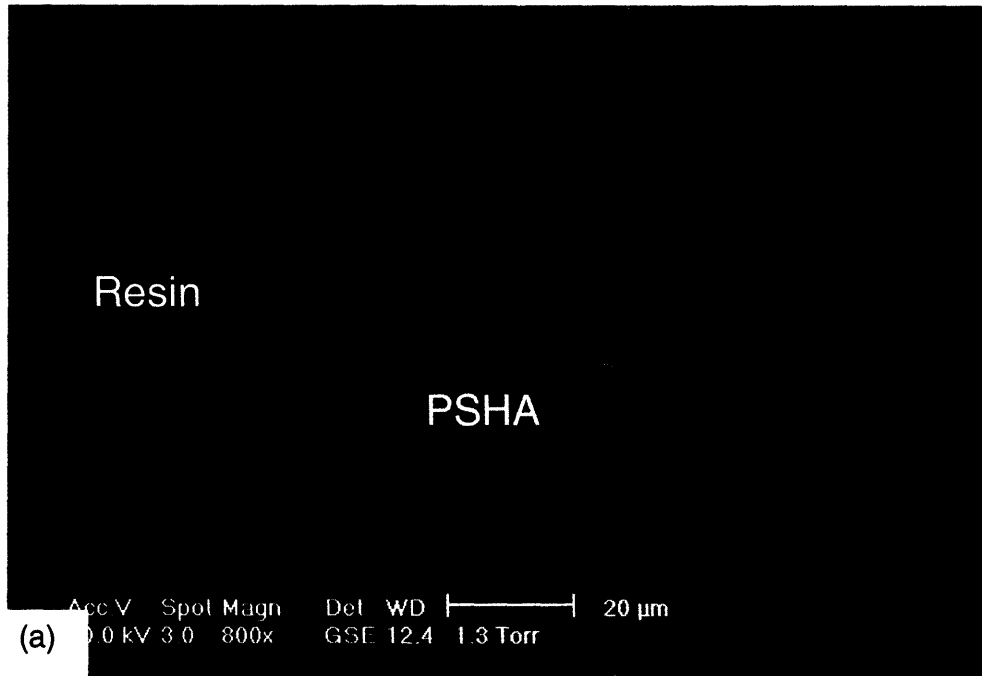
Figure 2-3 ESEM images from a cross section through EDHA coating: (a) 800X, (b) 2,000X
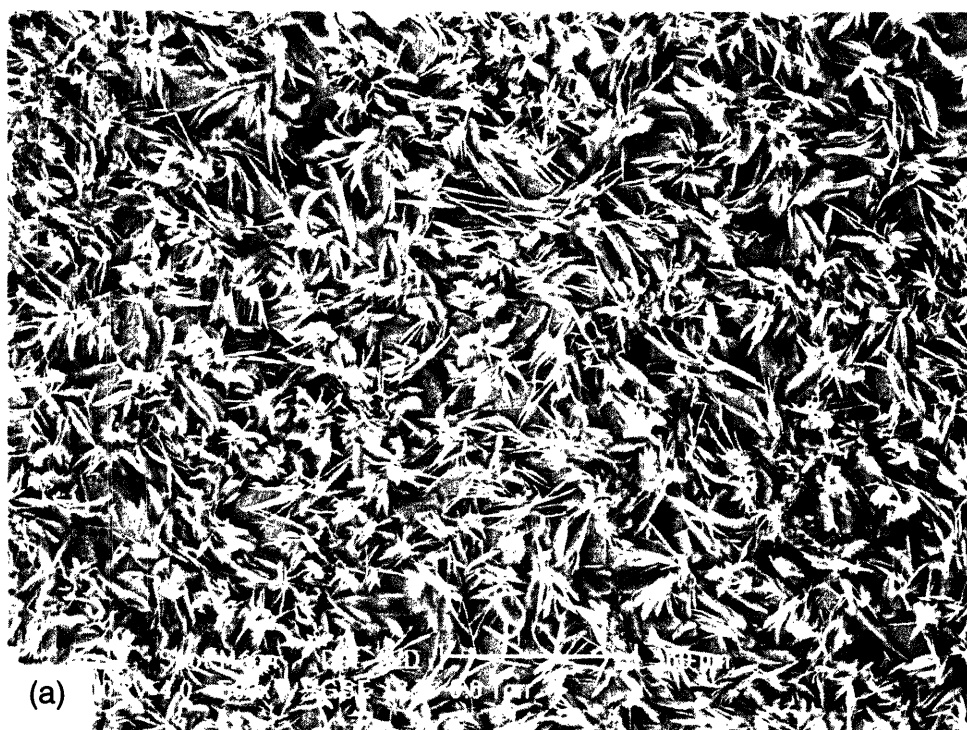
Figure 2-4 ESEM images of the surface morphologies of two coatings: (a) EDHA, (b) PSHA
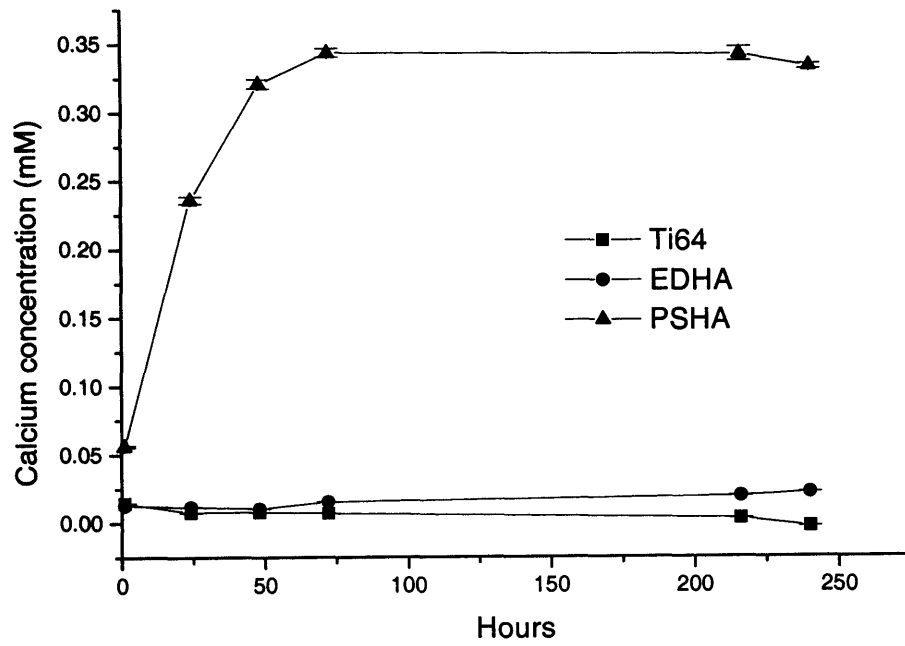
Figure 2-5 The aqueous solubilities of the two coatings. The bare Ti64 alloy serves as a reference.

2.4 ESEM result on bone apposition ratios

2.4.1 Six-hour Implantations

Both trabecular bone and its debris from the surgery was observed to remain around the implants 6 hours after the implantation, a feature found for all three types of implants (Figure 2-6). Some debris was very close to the implant surface and could have served as the source of osteoblast cells for the subsequent introduction of new bone apposing the implant. Due to the insert nature of the surgery, direct contact between bone and implants could also be observed (Figure 2-6(b)). However, 6 hours was too short for any meaningful new bone apposition on the implants, so the bone apposition ratio at 6 hours was not calculated.

(a)   200 μm

Bone

PSHA

Ti64

(b)

Ti64

Bone

EDHA

Acc V   Magn   Det WD ⊢————————————⊣   200 µm
0 kV 150x   GSE 17 7   1 4 Torr

(c)
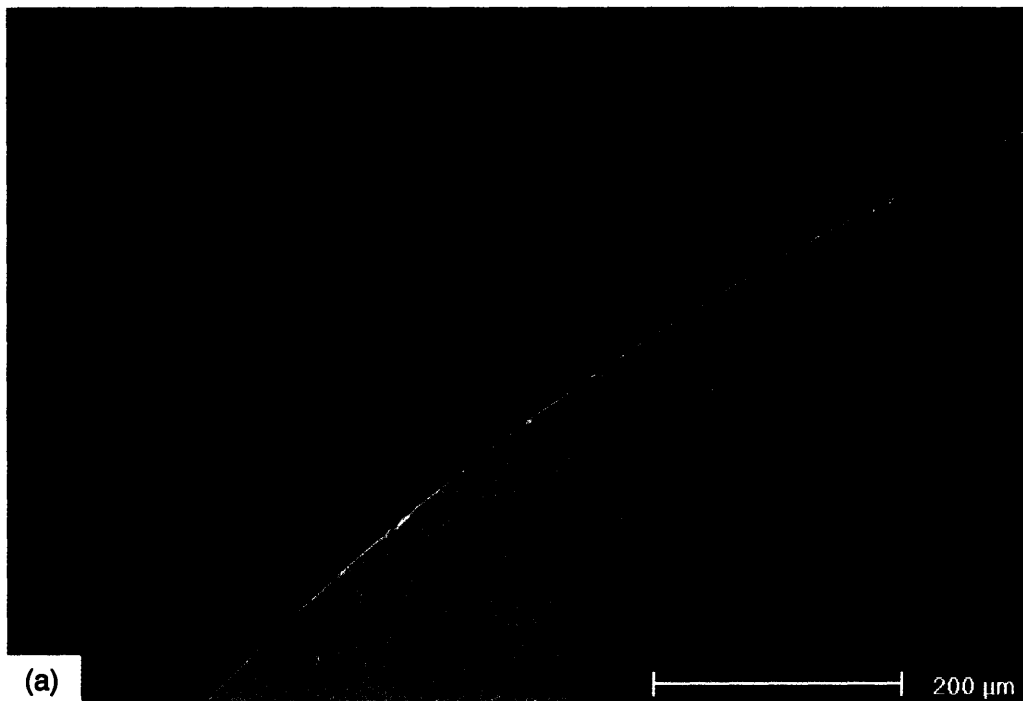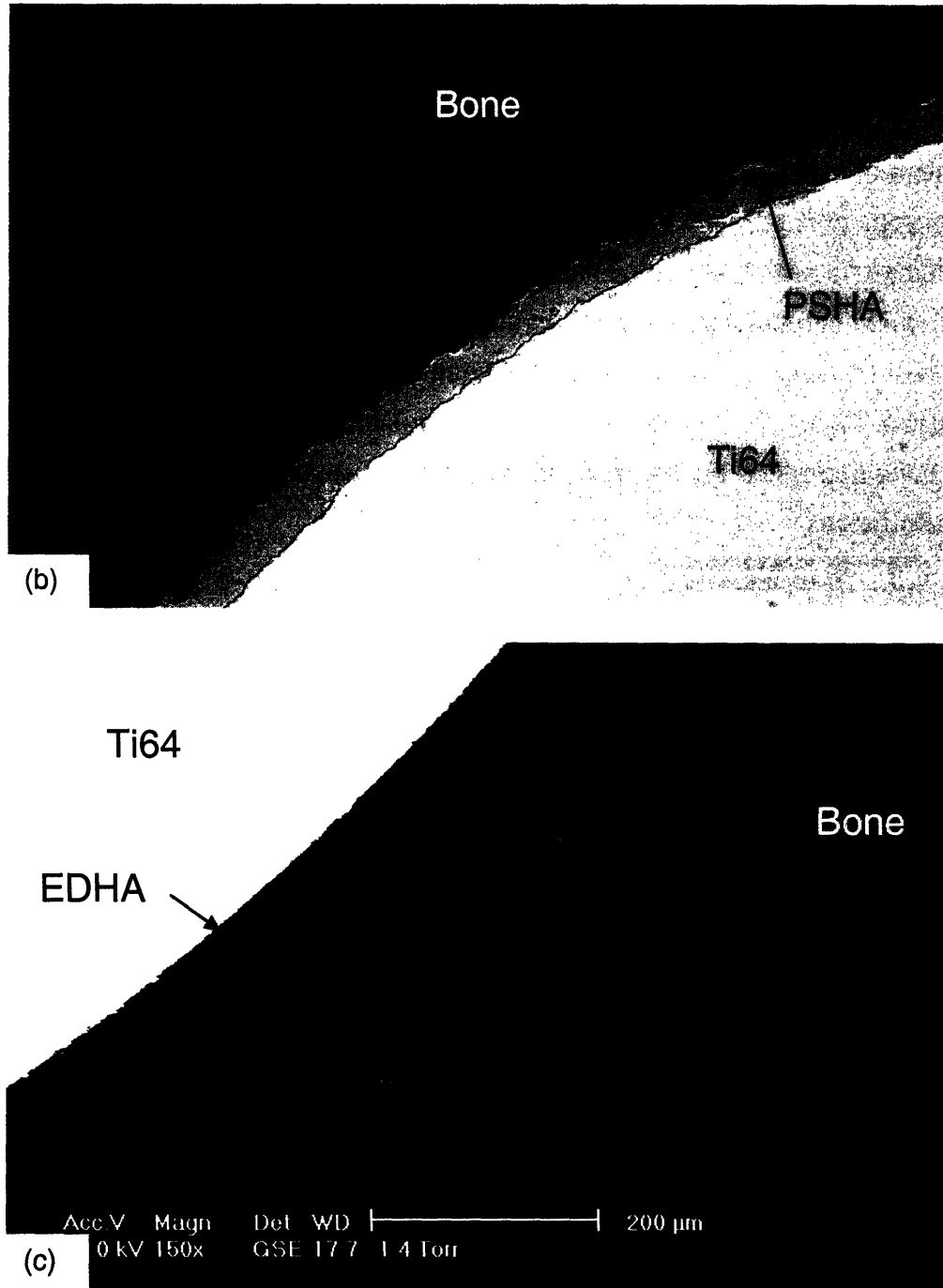
Figure 2-6 ESEM images from cross-sections through 6-hour implants and adjacent bone: (a) Ti64; (b) PSHA; (c) EDHA

44

2.4.2 Seven-day Implantations

Seven days after implantation, new bone tissue was observed on all three types of implants. The newly developed bone tissue was different from trabecular bone and its drillhole debris in that it closely contacted the implants and spread over on the coating surface. Cellular lacunae were clearly visible in the new bone tissue (Figure 2-7). However, PSHA showed much a higher surface bone apposition than the other two types of implants.

(a)
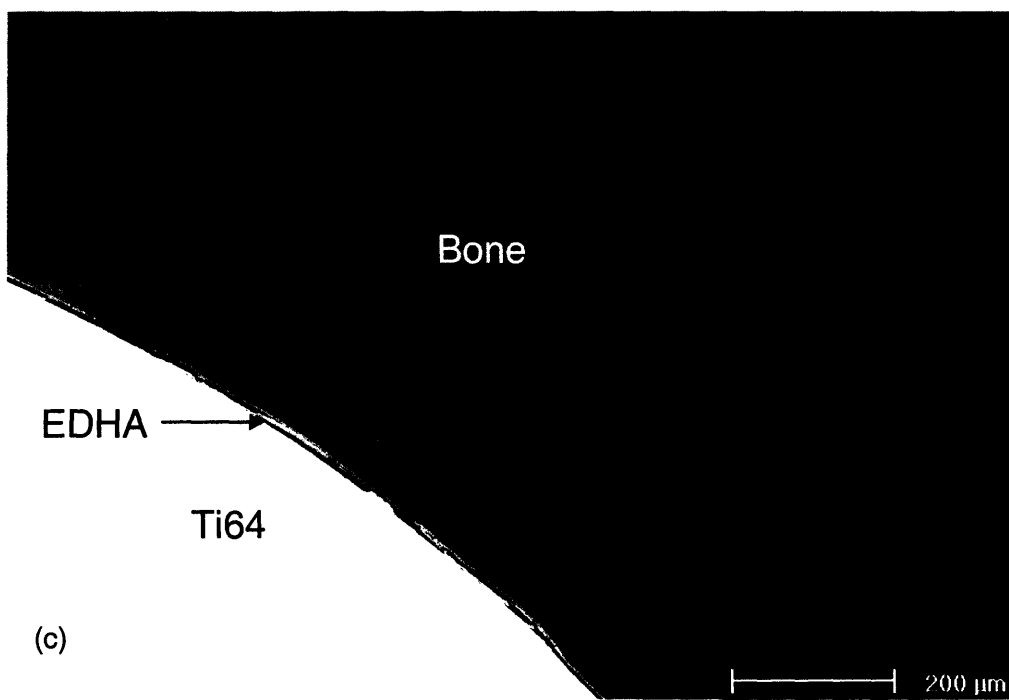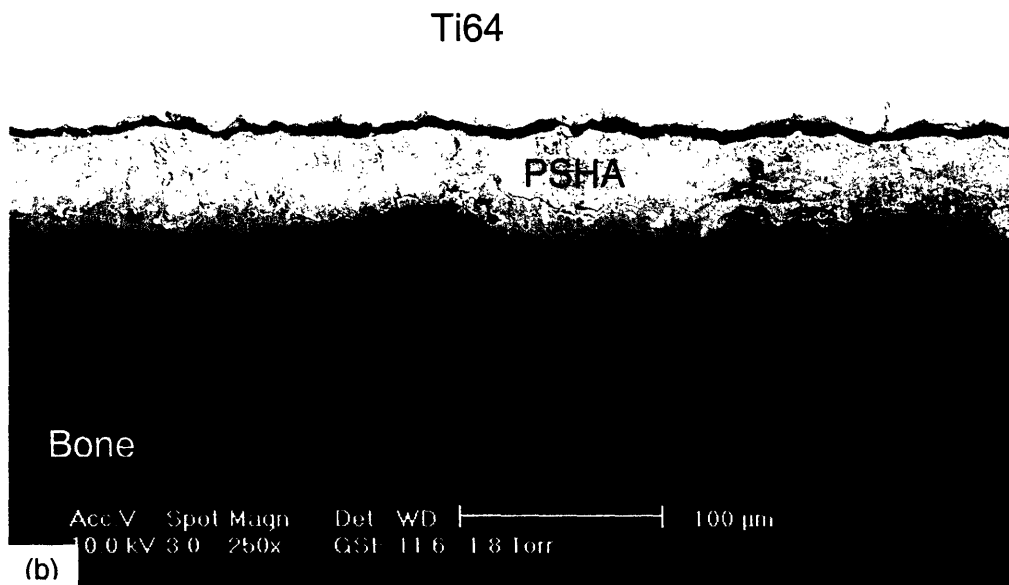
Ti64

Figure 2-7 ESEM images from cross-sections through 7-day implants and adjacent bone: (a) Ti64; (b) PSHA; (c) EDHA

2.4.3 Fourteen-day Implantations

After 14 days, the surface apposition of new bone tissue increased on all three types of implants (Figure 2-8). At the same time, the new bone tissue became much thicker, denser and very closely integrated with the coating surface; this was the most apparently for PSHA implants (Figure 2-8(b)). The surface apposition ratio for EDHA also increased dramatically, with new bone tissue covering much of the surface of the coating (Figure 2-8(c)). Ti64 coating showed the slowest relative increase of new bone tissue compared to the two coatings (Figure 2-8(a)).

Ti

Acc.V Magn   WD ├───────────┤ 100 µm
.0 kV 250x   10.5 1.4 Torr

(b)

Bone

100 µm

(c)
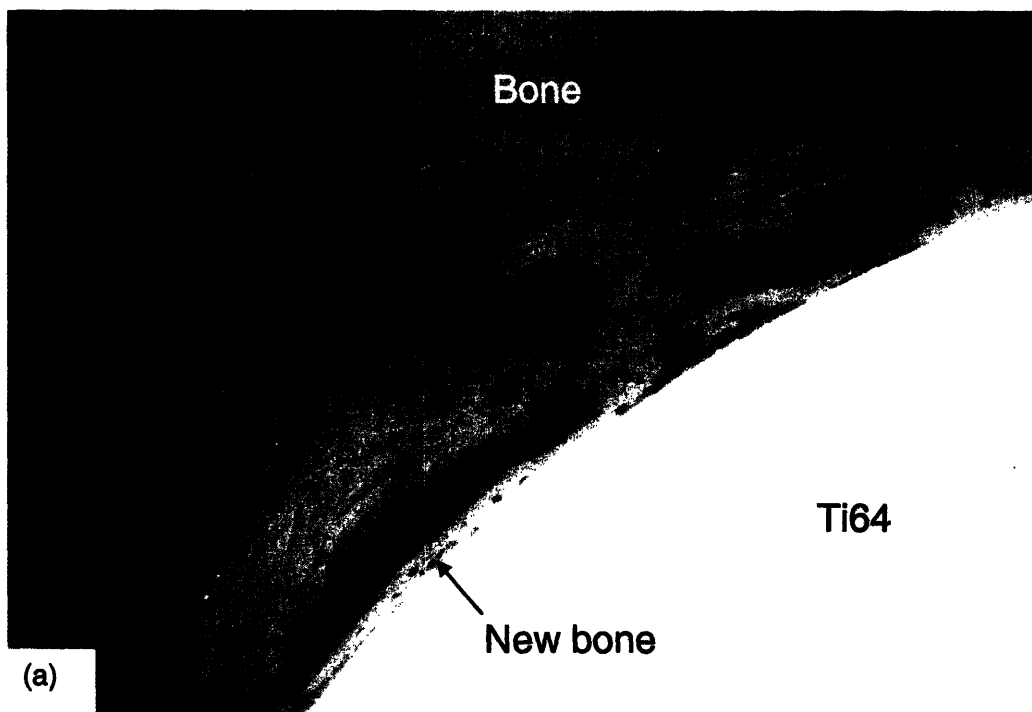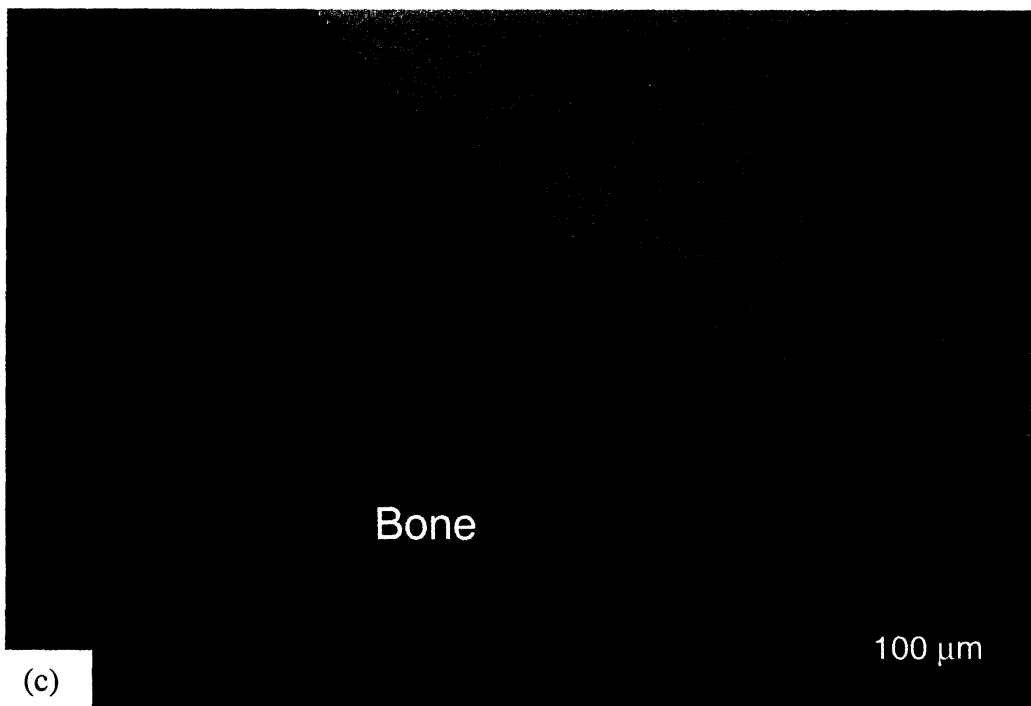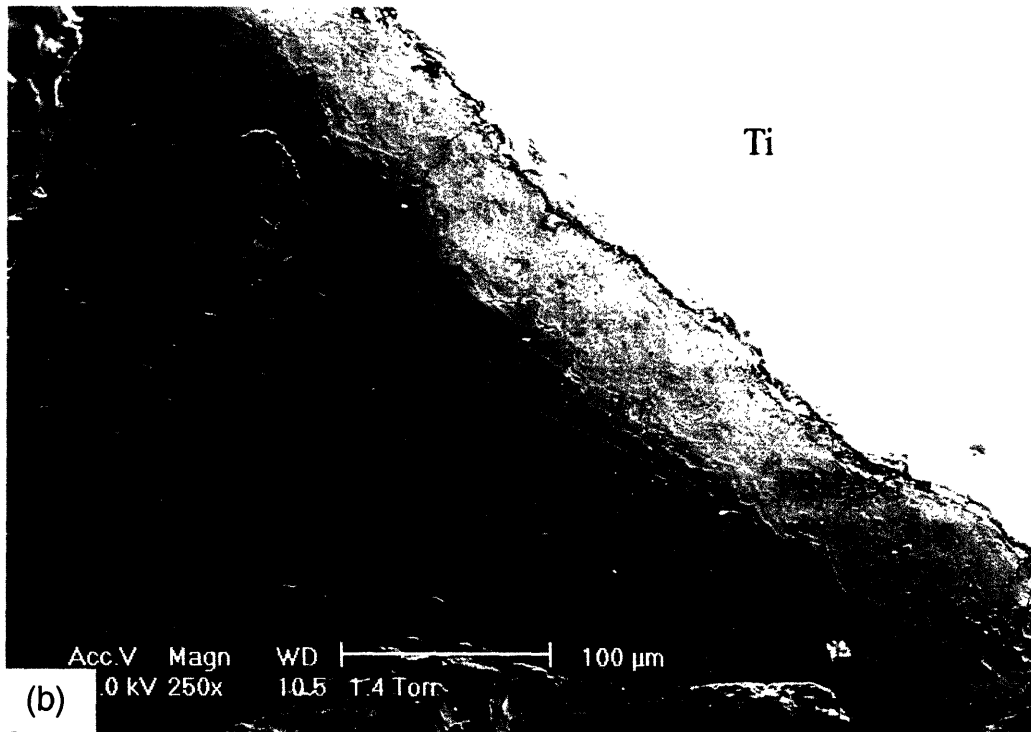
Figure 2-8 ESEM images from cross-sections through 14-day implants and adjacent bone: (a) Ti64; (b) PSHA; (c) EDHA

48
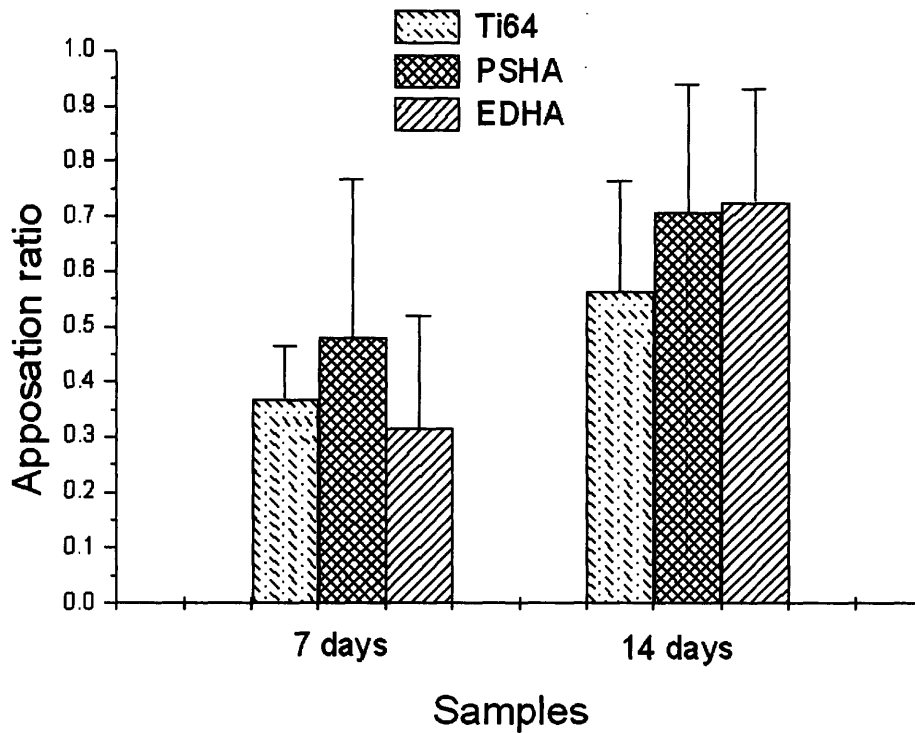
Figure 2-9 Average bone apposition ratios 7days and 14 days after implantation measured from ESEM images

The average surface bone apposition ratio for each type of sample 7 days and 14 days after implantation was calculated from the ESEM images (Figure 2-9). Student t-test analysis showed that PSHA coatings resulted in statistically higher apposition ratio than EDHA (p = 0.03) or Ti64 (p = 0.01) at 7 days. At the same time, no apparent difference was found for that of EDHA and Ti64 (p = 0.06).

At 14 days, both EDHA and PSHA had similar surface apposition ratios, around 70%, but Ti64 resulted in significantly lower surface apposition ratio, around 55%. Student t-test analysis showed the latter difference was statistically significant (p = 0.13 against PSHA, p = 0.06 against EDHA).

2.5 TEM study of the bone/coating interface

The TEM samples were prepared mechanically by cutting thin sections at room temperature in an ultramicrotome equipped with diamond knife. This method did not work for bare Ti64 samples because the metal always deformed and the metal/bone interface was destroyed. Sometimes, the cutting also broke the HA coatings, especially for PSHA coatings, because of its large thickness (more than 50 μm). However, in most cases the bone/coating interface kept intact, thanks to the embedding in Spurr's resin. Hence, ample information about the coating/interface was obtained from these samples, and the TEM study in this chapter was limited to implants with two HA coatings.

2.5.1 Six-hour Implantations

The morphologies and microstructures of both EDHA and PSHA coatings were quite different from those of biological apatite in bone (section 2.1.2). In the 6-hour PSHA implant, a thin portion of the PSHA coating (less than 5 μm) was studied (Figure 2-10(a)). One surface was confirmed to face the bone by the bone debris and blood cells nearby and trabecular bone tissue at farther distance away (not shown in the figure). The PSHA crystalline grains were very large (more than 500 nm); however, because the thickness of the sample section was only about 70 nm, the grain size and shape of PSHA coatings could not be determined by TEM alone (Figure 2-10(b)). A selected area electron diffraction pattern from the PSHA coating (inset, Figure 2-10(b)) showed single crystal character of the grains. The atom ratio of Ca/P was 1.67, matching with the stoichiometric value for HA. Higher magnification images showed a roughened surface on the coating, possibly a sign of coating dissolution (Figure 2-10(b)). Tiny HA crystals, either from reprecipitation of dissolved HA coating or from coatings loosened on implantation, were present closely to the HA coating surface.
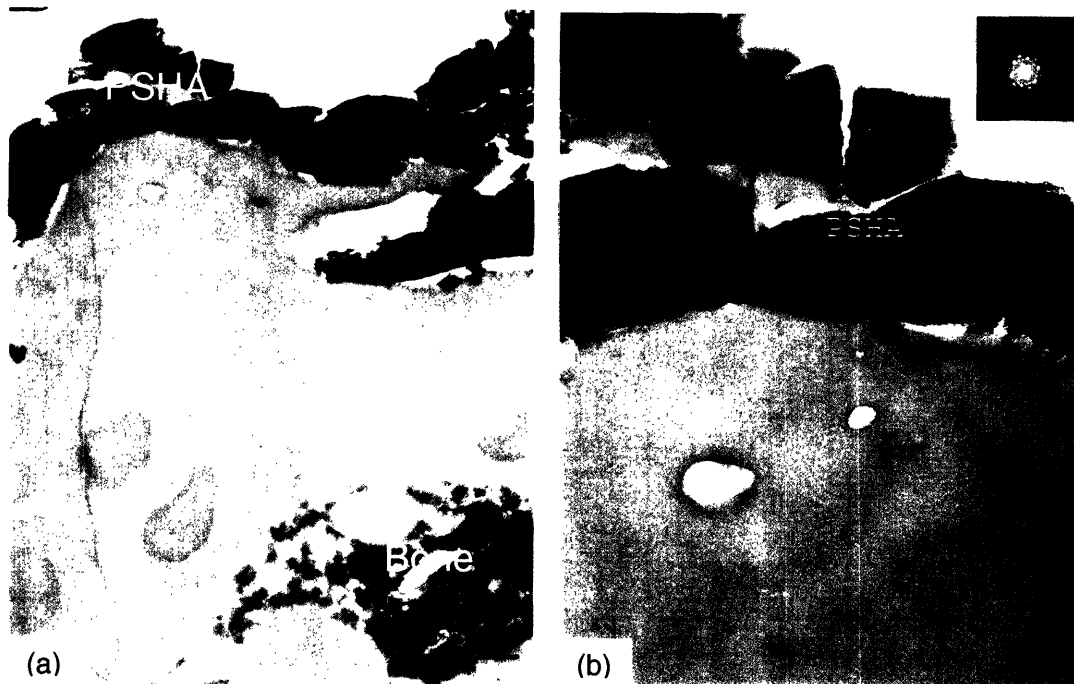
Figure 2-10 Cross section TEM micrographs of 6-hour PSHA-coated implant: (a) blood cells and bone debris visible close to the coating surface; (b) showing PSHA coating grains at coating surface

Compared to PSHA, EDHA coatings were preserved relatively intact due to their thinness (less than 5 µm) and high porosity (more resin penetrated and effectively embedded). The substrate side of the coating (far from the bone) was smooth, which suggests that the whole coating was removed from the titanium substrate, evidence that the bonding between EDHA and substrate was not very strong (Figure 2-11). A dense layer, composed of cuboidal crystals with size about 100 nm, was found at the bottom of the coating (Figure 2-12(a)). Apparently, a rapid nucleation of HA occured at the very beginning of the electrochemical deposition process, and many tiny HA crystals formed in this way; but only HA crystals in favorable orientations could further grow, and columnar crystals were formed close to the nucleation region (Figure 2-12(b)). These crystals grew until they intersected (Figure 2-13). The whole coating deposition process was reminiscent of dendritic growth. A selected area electron

51

diffraction pattern from one such crystal showed single crystal character (inset, Figure 2-13). The surface of these crystals was very smooth and no apparent sign of dissolution could be found. Elemental analysis established an Ca/P atom ratio of 1.6, close to that for HA (1.67).

Figure 2-11 Cross section TEM micrographs of 6-hour EDHA-coated implant

(a)

(b)
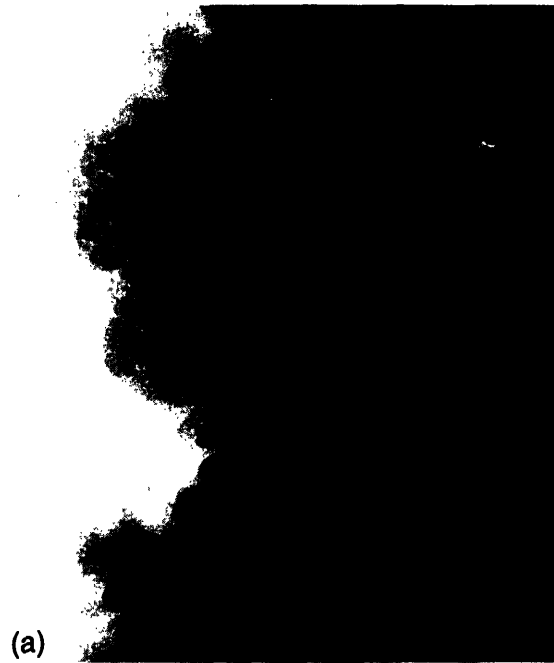
Figure 2-12 Cross-section TEM micrographs of 6-hour EDHA-coated implant: (a) the inner layer of the coating adjacent to the substrate was composed of nano-sized crystals; (b) large crystals growing on the inner layer

Figure 2-13 Cross-section TEM micrographs of 6-hour EDHA-coated implant
showed dendritic growth of the coating. The platelet crystals
exhibited single crystal character, by selected area electron
diffraction.

54

2.5.2 Seven-day Implantations

After 7 days, TEM revealed a layer of bone tissue formed on the PSHA coating surface (Figure 2-14) and mineralized "nodules" found in the region close to bone/coating interface. The size of these nodules ranges from 100 nm to about 1 μm. High magnification images of these nodules showed that they were composed of many fine fibrils, which were several hundred nm long but only several nm wide (Figure 2-15), in agreement with previous results from our group[23]. Surrounding these nodules was a very dense collagen matrix, whose fibers were characterized by the banded structure visible after lead citrate and uranyl acetate staining. Differently orientated fibrils were observed; however, their size was very uniform: the widths were consistently less than 50 nm, but the lengths could be as long as 1 μm. Elemental analysis by XEDS showed that the calcium/phosphorous atom ratio of the nodules was about 1.2, much lower than that for HA (1.67) but close to dicalcium phosphate dihydrate (DCPD, 1.0), octacalcium phosphate (OCP, 1.33), and amorphous calcium phosphate (ACP, 1.5). Hence, it is likely that at least one of these calcium phosphates also forms in early bone mineralization. For comparison, the calcium/phosphorous ratio of the coating was about 1.6, while in the non-mineralized region (including the collagen) the calcium content was very low (less than 1% atom ratio) and phosphorous was not detectable. The selected area electron diffraction pattern showed broad polycrystalline rings in the new bone region (inset, Figure 2-16), reflecting the formation of nano-sized HA crystals (Figure 2-17).

An osteoblast was observed close to the coating surface (Figure 2-18). The high activity of this cell could be deduced from its large nucleus, prominent Golgi, and endoplasmic reticulum. A close view showed that a layer of collagen fibers (about 500 nm thick) was present between the HA coating and the osteoblast, the axis of the collagen fibers parallel with the coating surface. The collagen layer didn't directly contact the coating. Instead, there was a thin electron-dense layer, about 50 nm thick, between the collagen and the coating surface.
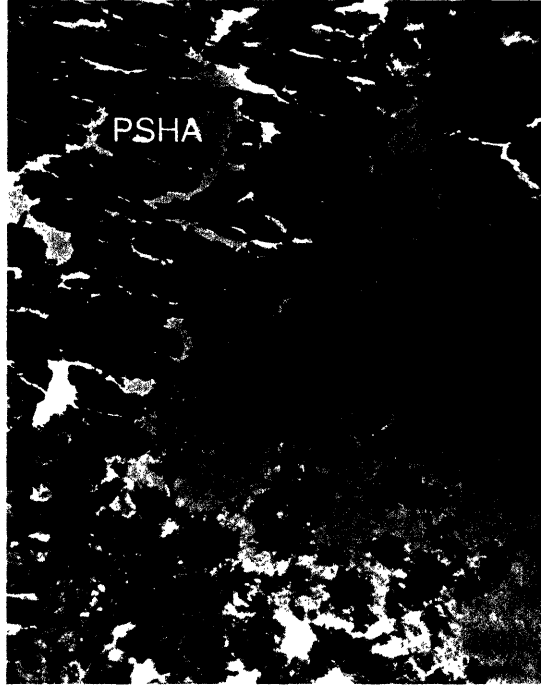
Figure 2-14 TEM cross section micrograph of 7-day PSHA implant, stained with uranyl acetate and lead citrate.

Figure 2-15 Mineralized nodules formed close to the PSHA coating 7 days after implantation, stained with uranly acetate and lead citrate.
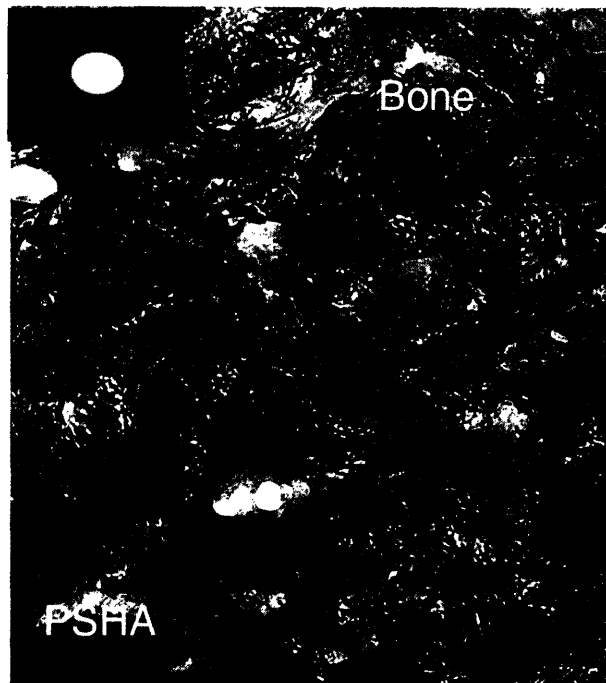
Figure 2-16 Close bonding between new bone tissue and PSHA coating after 7 days implantation. The selected area electron diffraction pattern (inset) exhibited broad polycrystalline rings
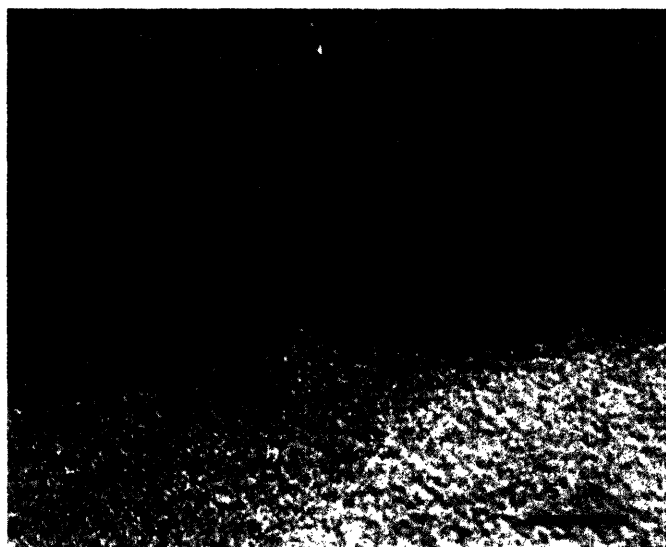
Figure 2-17 Nano-sized HA crystals found in new bone tissue at the interface with PSHA coating 7 days after implantation, TEM high-resolution lattice-fringe image, no objective aperture.
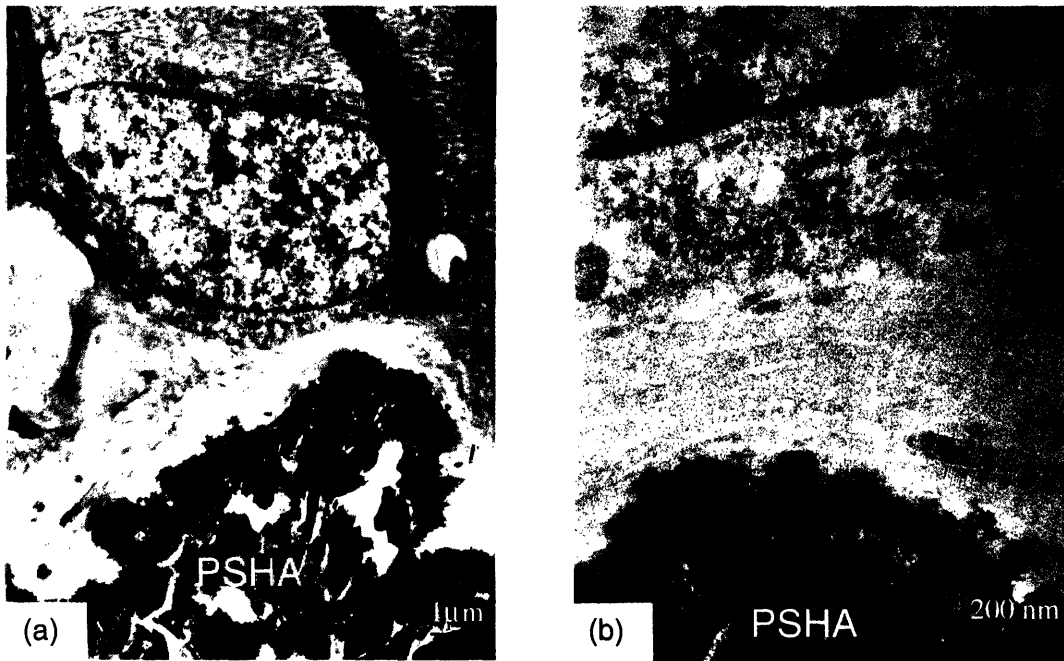
Figure 2-18 An osteoblast found close to the PSHA coating surface after 7 days'
implantation: (a) The cell is characterized by its large nucleus,
prominent Golgi, and endoplasmic reticulum; (b) a collagen layer
and an electron-dense layer were found at the PSHA coating surface.
TEM cross-section stained with uranyl acetate and lead citrate.

Interestingly, osteoclasts could also be found on the PSHA coating surface after 7 days' implantation (Figure 2-19). The osteoclast cell directly contacted the coating surface with no intervening gap. It seems that the cell was digesting the coating, and HA debris was found inside it.
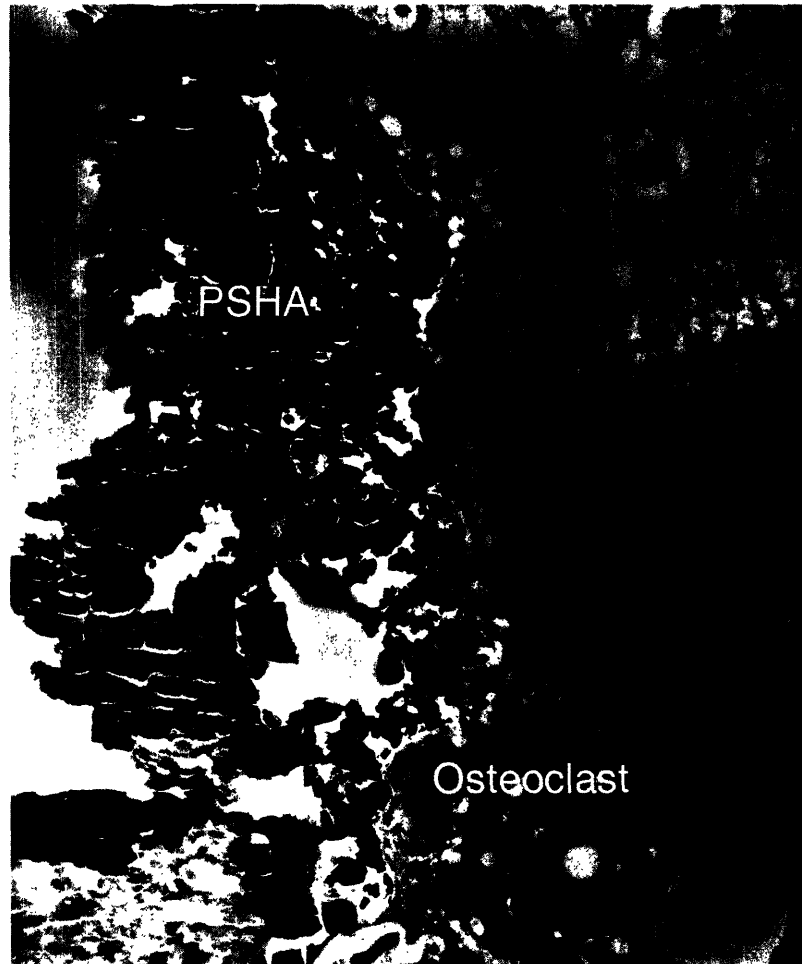
Figure 2-19 Osteoclast found on the PSHA coating surface after 7 days implantation: the osteoclast was in close contact with the coating surface, without any gap; some HA debris was found inside the cell. TEM cross-section stained with uranyl acetate and lead citrate.

By contrast, little tissue development was seen near the EDHA coating surface 7 days after implantation. Osteobalst-like cells were found in some regions stationed close to (10~15 μm) the coating surface (Figure 2-20). The coating surface, despite one week in implantation, was still similar to the 6 hour one (Figure 2-21).

Figure 2-20 No new bone tissue visible on the EDHA coating surface after 7 days implantation, though bone cell observed 10~15 μm from surface. TEM cross section stained with uranyl acetate and lead citrate.
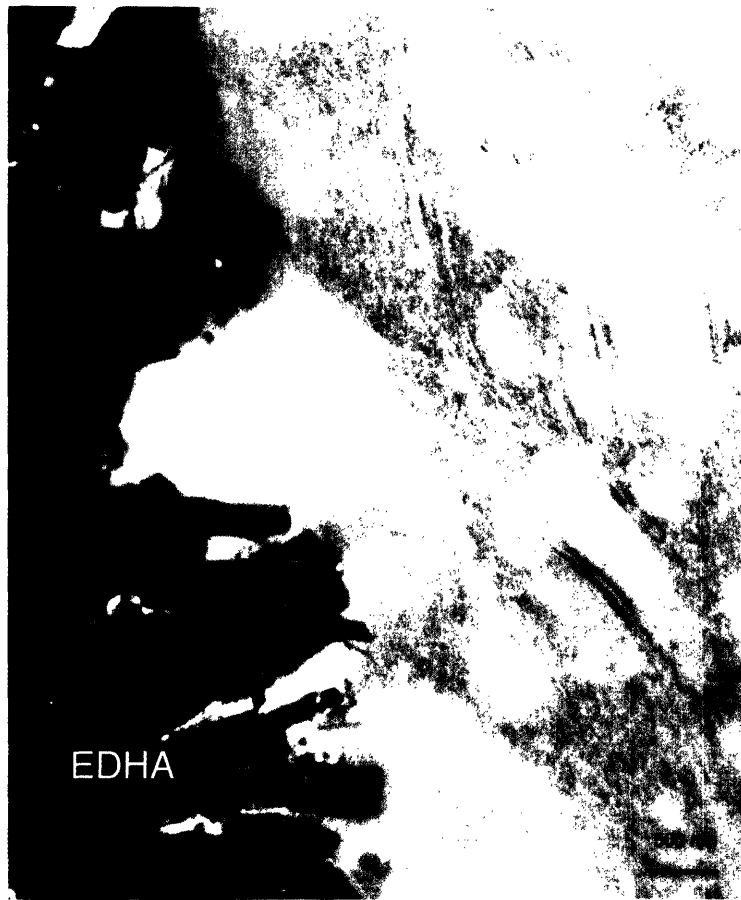
Figure 2-21 The EHDA coating surface 7 days after implantation. TEM cross
section stained with uranyl acetate and lead citrate.

2.5.3 Fourteen-day Implantations

At 14 days, the new bone tissue layer on the PSHA became much thicker
and covered almost the whole surface (Figure 2-22). The characteristic band
structure of mineralized collagen could be seen already in the new bone tissue
layer. The calcium/phosphorous atom ratio increased to nearly 1.7.

Figure 2-22 TEM micrograph for PSHA coating at 14 days. TEM cross section
stained with uranyl acetate and lead citrate.

Compared to PSHA, implanted EDHA changed much more dramatically from 7 days to 14 days (Figure 2-23). Much new bone tissue was found on the EDHA surface and closely integrated with the coating. The calcium/phosphorous ratio of the new bone tissue was close to 1.7. The increase in bone apposition noted matched the increase in bone apposition ratio already documented in SEM observations.

Figure 2-23 TEM micrograph for EDHA coating at 14 days. TEM cross section stained with uranyl acetate and lead citrate.

2.6 Discussion

Both EDHA and PSHA coatings used in this study were predominantly composed of HA and had the same nominal compositions. However, they were distinct in surface morphologies and microstructures, which appear to have resulted in differing solubilities, i.e, in their ability to initially release calcium and phosphorus into the environment. The solubility test showed that PSHA dissolved much more readily than EDHA. The former reached saturation in distilled water in two days, while the latter occasioned a very low Ca concentration after 10 days. It is suspected the difference in their solubility has resulted in the different early bone formation kinetics on these two coatings.

EDHA showed the low bone apposition ratio at 7 days, close to that of Ti64 at 7 days. And at 14 days, the EDHA bone apposition ratio increased markedly, to that observed for PSHA, much more than that for bare Ti64. The initial low apposition ratio can be explained by the low EDHA solubility. In the first seven days, the coating made almost no contribution to bone apposition, so it had almost the same apposition ratio as Ti64. For PSHA, with its partial amorphous content and higher consequent solubility, results in a much higher local concentration of calcium and phosphorus, which could assist and accelerate local mineralization of new bone. However, the differing solubilities serve to contribute only at most a short-term difference in mineralization behavior. By 7 days, the surface apposition ratio of EDHA increased sharply and caught up with that of PSHA, suggesting that the dissolution of EDHA also reached a threshold value and hence began to accelerate the new bone formation. Similar behavior had been observed before in our group on annealed and unannealed PSHA coatings[23].

At 7 days, new bone tissue, which was mainly composed of clustered nano-fibers, was observed only on PSHA coatings. Collagen fibers, visible after staining, were also present close to the coating surface; however, they were not yet mineralized. At 14 days, for both coatings, the new bone tissue was very well developed, and mineralized collagen fibers could be found in this bone tissue.

64

Many proteins, including osteocalcin, osteopontin, and fibronectin, have hypothesized to be the substrate for HA to deposit on. However, in this study, the early mineral deposits observed were actually long fibrils, different from the morphologies of the proteins mentioned. The mineral fibrils were only about several nm in width, but 300 nm in length, very close to the size of a single collagen molecule (1.5 nm diameter and 300 nm length). It is well known that the collagen molecules are secreted by osteoblasts and then self-assemble into collagen fibers by cross-linking with each other. It has been demonstrated that collagen fibers alone don't have the ability to initiate mineral deposition. However, collagen molecules before self-assembling into fibers might have the ability to nucleate mineral formation, a phenomenon recently observed *in vitro* by Cui's group[28]. Hence, the mineral fibers observed 7 day after implantation at PSHA coating surface could be mineral nucleating on individual collagen molecules. This explanation has never been advanced before and still remains a hypothesis. More experiment is needed to prove or disprove it.

Another interesting observation was the low calcium/phosphorus atom ratio in the early mineral deposits. It strongly suggests that HA may not be the only calcium phosphate phase involved in early-stage mineralization. It has been observed *in vitro* that ACP and OCP, which have more favorable formaton kinetics than HA, were deposited before HA. This study has shown that the same may occur for bone formation in vivo. Theories of protein control of bone mineralization have mainly focused on the shape match between proteins and the HA unit cell. For example, Hoang et al., deducing the crystal structure of osteocalcin by X-ray diffraction, claim that they revealed a negatively charged protein surface that coordinates five calcium ions in a spatial orientation that is complementary to calcium ions in the HA crystal lattice[25]. Sarig also hypothesized that aspartic acid nucleates the apatite crystallites of bone in such a way that the aspartic acid is enclosed inside a carbonated, calcium-deficient unit, without changing its external appearance, and is able to start assemblage of regular apatite units[29]. However, the present observations in this study

suggests that the role of proteins in nucleating other non-apatitic calcium phosphates, such as ACP and OCP, could be initially more important.

Electrochemically-deposited HA, as a potential substitute for plasma-sprayed HA, confers some advantages, such as low processing temperature and deposition on complicated shapes. However, two shortcomings of EDHA coatings compared to PSHA were observed in this study: (1) slower bone apposition; and (2) lower bonding strength between coating and substrate. The first problem is attributed to the low solubility of the coating. It has been reported that nano-phase HA could be formed directly from electrochemical deposition[20]. If the main component of the coating can be controlled to nano-sized HA, the solubility will doubtless increase, which could accelerate the bone formation kinetics. The second problem can be solved by introducing chemical bonding between coating and substrate. Chemically-treated titanium, exposed to NaOH, H_2O_2, or other chemicals, has a higher ratio of basic hydroxyl Ti-OH, which facilitates the nucleation of calcium phosphate by formation of chemical bonds to the coating. If the substrate can be treated chemically before deposition, chemical bonding can occur between coating and the substrate to increase the bonding strength. Such substrate treatment could be a future direction for EDHA coating technology.

2.7 References

1. Overgaard, S., *Calcium Phosphate coating for fixation of bone implants.* Acta Orthop Scand, 2000. **71**(Suppl. 297): p. 1-74.

2. Soballe, K., E.S. Hansen, B.R. H, P.H. Jorgensen, and C. Bunger, *Tissue ingrowth into titanium and hydroxyapatite-coated implants during stable and unstable mechanical conditions.* J Orthop Res, 1992. **10**(2): p. 285-99.

3. Thomas, K.A., S.D. Cook, R.J. Haddad, Jr., J.F. Kay, and M. Jarcho, *Biologic response to hydroxylapatite-coated titanium hips. A preliminary study in dogs.* J Arthroplasty, 1989. **4**(1): p. 43-53.

4. Davies, J.E., R. Chernecky, B. Lowenberg, and A. Shiga, *Deposition and Resorption of Calcified Matrix Invitro by Rat Marrow-Cells.* Cells and Materials, 1991. **1**(1): p. 3-15.

5. Linder, L., T. Albrektsson, P.I. Branemark, H.A. Hansson, B. Ivarsson, U. Jonsson, and I. Lundstrom, *Electron microscopic analysis of the bone-titanium interface.* Acta Orthop Scand, 1983. **54**(1): p. 45-52.

6. Steflik, D.E., A.L. Sisk, G.R. Parr, L.K. Gardner, P.J. Hanes, F.T. Lake, D.J. Berkery, and P. Brewer, *Osteogenesis at the dental implant interface: high-voltage electron microscopic and conventional transmission electron microscopic observations.* J Biomed Mater Res, 1993. **27**(6): p. 791-800.

7. Steflik, D.E., R.S. Corpe, F.T. Lake, T.R. Young, A.L. Sisk, G.R. Parr, P.J. Hanes, and D.J. Berkery, *Ultrastructural analyses of the attachment (bonding) zone between bone and implanted biomaterials.* J Biomed Mater Res, 1998. **39**(4): p. 611-20.

8. de Groot, K., R. Geesink, C.P. Klein, and P. Serekian, *Plasma sprayed coatings of hydroxylapatite.* J Biomed Mater Res, 1987. **21**(12): p. 1375-81.

9. Gerdeman, D.A. and N.L. Hecht, *Arc plasma technology in materials science.* Applied mineralogy ; 3. 1972, New York,: Springer-Verlag. x, 206 p.

10. Wen, H.B., J.R. de Wijn, F.Z. Cui, and K. de Groot, *Preparation of calcium phosphate coatings on titanium implant materials by simple chemistry.* J Biomed Mater Res, 1998. **41**(2): p. 227-36.

11. Suchanek, W. and M. Yoshimura, *Processing and properties of hydroxyapatite-based biomaterials for use as hard tissue replacement implants.* Journal of Materials Research, 1998. **13**(1): p. 94-117.

12. Luo, Z.S., F.Z. Cui, and W.Z. Li, *Low-temperature crystallization of calcium phosphate coatings synthesized by ion-beam-assisted deposition.* J Biomed Mater Res, 1999. **46**(1): p. 80-6.

13. Spoto, G., E. Ciliberto, and G.C. Allen, *A New Synthetic Route to Hydroxyapatite Coatings.* Journal of Materials Chemistry, 1994. **4**(12): p. 1849-1850.

14. Russell, S.W., K.A. Luptak, C.T.A. Suchicital, T.L. Alford, and V.B. Pizziconi, *Chemical and structural evolution of sol-gel-derived hydroxyapatite thin films under rapid thermal processing.* Journal of the American Ceramic Society, 1996. **79**(4): p. 837-842.

15. Tucker, B.E., C.M. Cottell, R.C. Auyeung, M. Spector, and G.H. Nancollas, *Pre-conditioning and dual constant composition dissolution kinetics of pulsed laser deposited hydroxyapatite thin films on silicon substrates.* Biomaterials, 1996. **17**(6): p. 631-7.

16. Ducheyne, P., S. Radin, M. Heughebaert, and J.C. Heughebaert, *Calcium-Phosphate Ceramic Coatings on Porous Titanium - Effect of Structure and Composition on Electrophoretic Deposition, Vacuum Sintering and Invitro Dissolution.* Biomaterials, 1990. **11**(4): p. 244-254.

17. Shirkhanzadeh, M., *Calcium-Phosphate Coatings Prepared by Electrocrystallization from Aqueous-Electrolytes.* Journal of Materials Science-Materials in Medicine, 1995. **6**(2): p. 90-93.

18. Shirkhanzadeh, M., *Bioactive Calcium-Phosphate Coatings Prepared by Electrodeposition.* Journal of Materials Science Letters, 1991. **10**(23): p. 1415-1417.

19. Redepenning, J. and J.P. McIsaac, *Electrocrystallization of Brushite Coatings on Prosthetic Alloys.* Chemistry of Materials, 1990. **2**(6): p. 625-627.

20. Shirkhanzadeh, M., *Direct formation of nanophase hydroxyapatite on cathodically polarized electrodes.* Journal of Materials Science-Materials in Medicine, 1998. **9**(2): p. 67-72.

21. Rosen, V.B., L.W. Hobbs, and M. Spector, *The ultrastructure of anorganic bovine bone and selected synthetic hyroxyapatites used as bone graft substitute materials.* Biomaterials, 2002. **23**(3): p. 921-8.

22. Porter, A.E., L.W. Hobbs, V.B. Rosen, and M. Spector, *The ultrastructure of the plasma-sprayed hydroxyapatite-bone interface predisposing to bone bonding.* Biomaterials, 2002. **23**(3): p. 725-33.

23. Benezra, V.I., Electron microscopic investigation of interfaces in materials for orthopedic applications, Thesis Ph.D. --Massachusetts Institute of Technology Dept. of Materials Science and Engineering 1998.

24. Hunter, G.K. and H.A. Goldberg, *Nucleation of hydroxyapatite by bone sialoprotein.* Proc Natl Acad Sci U S A, 1993. **90**(18): p. 8562-5.

25. Hoang, Q.Q., F. Sicheri, A.J. Howard, and D.S. Yang, *Bone recognition mechanism of porcine osteocalcin from crystal structure.* Nature, 2003. **425**(6961): p. 977-80.

26. Couchourel, D., C. Escoffier, R. Rohanizadeh, S. Bohic, G. Daculsi, Y. Fortun, and M. Padrines, *Effects of fibronectin on hydroxyapatite formation.* J Inorg Biochem, 1999. **73**(3): p. 129-36.

27. Feng, Q.L., H. Wang, F.Z. Cui, and T.N. Kim, *Controlled crystal growth of calcium phosphate on titanium surface by NaOH-treatment.* Journal of Crystal Growth, 1999. **200**(3-4): p. 550-557.

28. Zhang, W., S.S. Liao, and F.Z. Cui, *Hierarchical self-assembly of nano-fibrils in mineralized collagen.* Chemistry of Materials, 2003. **15**(16): p. 3221-3226.

29. Sarig, S., *Aspartic acid nucleates the apatite crystallites of bone: a hypothesis.* Bone, 2004. **35**(1): p. 108-13.

Chapter 3 Quantitative study of osteoblast-like cell mineralization with Tc-99m-MDP *in vitro* labeling

3.1 Introduction

In chapter 2, the *in vivo* canine model was used to study the ultrastructure of the interface between bone and implants. The early bone formation process and the bone apposition ratios for different implant materials were discussed. The *in vivo* experiments proved to be very effective in the study of implant materials. However, for both ethical and financial reasons, animal experiments should be strictly restricted (3R principles: replacement, reduction and refinement), so it is desirable to establish alternative methods to at least partially replace animal experiments[1].

In vitro cell-culture experiments, as a promising substitute for *in vivo* experimentation, are increasingly gaining more and more attention. Osteoblasts and osteoblast-like cells are widely used in the *in vitro* study of biomaterials to be employed as permanent implants in bone and for bone tissue engineering [2]. Normally, these cells are cultured on biomaterials prepared as two-dimensional surfaces or as porous three-dimensional scaffolds. After selected time periods, the cell cultures are terminated for analysis of the cell behavior (*e.g.*, synthesis of extracellular matrix). This methodology has provided a relatively simple approach for the study of the interaction between cells and biomaterials and has been used as an important screening step before proceeding to *in vivo* experimentation [3, 4]. Furthermore, the experiment conditions in *in vitro* environments are easier to control. Consequently, the relationships between particular elements of the system can be purposely designed and investigated. Another advantage of *in vitro* experiment is the relatively low cost. More samples can be obtained, which makes statistical study easier and more reliable[5].

3.1.1 Cell source

Choosing the right cell source is a necessity in an *in vitro* experiment. The cell source used in *in vitro* study should be stable, reproducible, easy to obtain, and most important, able to duplicate the *in vivo* process researchers are interested in. Commonly used osteoblast cell sources include: collagenase digestion of fetal or neonatal rat or mouse calvaria, cloned cell lines, organ culture, and bone marrow stromal cells.

As early as 1964, Peck et al. begun to use bacterial collagenase to remove the fibrous connective tissue in fetal or neonatal rat calvaria and harvest viable osteoblasts[6]. Bard et al. further applied this method to adult human bone[7]. The cells harvested by this method are actually a mixture including osteoblast, preosteblast, osteoclast, fibroblast, and blood cells. Using appropriate digestion solutions and proper digestion procedures, preosteoblast and osteoblast can be obtained as the dominant types. Centrifuging and culturing on tissue culture polystyrene (TCPS) can help to remove the included blood cells. This method can provide young and active osteoblast cells in large quantity. The potential problem for this method is that collagenase digestion can damage the osteoblast cells and influence their normal functions.

Osteoblast cell lines were first introduced by Majeska and his colleagues in 1980, by enzymatically dispersing rat osteogenic sarcoma cells[8]. In 1982, Kodama *et al.* cloned a new immortal cell line from newborn mouse calvaria, which they named the MC3T3 cell line[9]. MC3T3 cell line is one of the most often used cell lines for osteoblast study. While these cell lines are only transformed cells and not osteoblasts, they can mineralize under proper condition and can be useful tools for the study of specific osteoblast functions. Such model systems are relatively homogenous and easy to maintain, so the results are easier to reproduce compared to other cell sources.

In the 1970s, Jones and Boyde described the migration of osteoblasts from rat calvaria onto various artificial or natural materials[10]. This study proved

that organ culture of bone can also be used to test bioactivity of implant materials. In this method, osteoblasts migrate in a more natural way without the mechanical or chemical separation from the matrix. These osteoblasts are believed to be less damaged than those by other methods, and the interaction between cells and substrates can be in a way more similar to that in vivo. However, it takes a longer time for cells to grow out from the bone organ, and other cells, such as fibroblasts and blood cells, can mix and interfere with osteoblasts.

In 1976, Friedenstein and his colleagues identified in the adult bone marrow a cell population with strong osteogenic potential[11]. They observed that cells attached to the plastic appeared fibroblastic in shape and were actively proliferating; if implanted in vivo, these cells were able to form bone and hematopoiesis-supportive stroma, reconstituting a complete bone/bone marrow organ[12]. They called this type of cells bone marrow stromal cells (BMSCs). The ease of harvest from donor bone marrow, together with the ability to form bone in vivo, make BMSCs ideal for clinical applications. However, these BMSCs have to be expanded in vitro to get enough quantity for in vivo experiment or clinical use. The investigation of the expanded BMSC population led to the observation that in vitro expansion appears a limiting passage: cells tend to senesce and lose their multidifferentiation potential with time in culture[12], so more investigation is necessary before the safe and effective use of BMSCs can be achieved.

3.1.2 Tc-99m-MDP as a quantitative analysis method

Bone-forming cells are characterized by their synthesis of a type I collagen matrix that mineralizes. The compatibility of a biomaterial with this process (i.e., its enhancement or inhibition of the process) can thus be characterized, in part, by the amount of mineral produced by the cells cultured on its surface. Currently, several methods are being employed to assess the mineralization associated with the growth of osteoblasts and osteoblast-like cells on biomaterials: histology employing Von Kossa staining [13]; scanning electron microscopy (SEM) [14, 15] and energy-dispersive x-ray microanalysis (XEDS) [15, 16]; transmission electron microscopy (TEM) [15, 17-19]; x-ray diffraction [15]; and calcium radioisotope

71

(^{45}Ca) uptake [19]. While these methods have yielded valuable findings, all have one or more of the following shortcomings: (1) harmful to the cells, not allowing for further experimentation; (2) time consuming; and (3) only qualitative, which makes comparison of the osteoblast mineralization response to different biomaterials very difficult. A particular problem for calcium-based biomaterials is that it is difficult to distinguish the substrate materials from the newly formed mineral. The need for a non-destructive and quantitative method for the evaluation of the mineral deposition associated with the activity of osteoblast-like cells on biomaterials, including those which contain calcium, prompted this investigation of a novel use of a calcium-binding radionuclide agent used for many years in diagnostic imaging.

Technetium-methylene diphosphonate (Tc-99m-MDP) has been used for many years in nuclear medicine [20, 21] for the diagnosis of abnormalities in bone formation and remodeling, including osteogenic tumors [22]. Tc-99m-MDP is preferentially adsorbed by newly produced mineral by a mechanism that yet remains to be completely understood. The half-life of Tc-99m is 6.01 hours, and it decays by gamma emission of 140 KeV photons, which are suitable for imaging with a gamma camera. Areas with high osteogenic activity are highly Tc-99m-MDP avid and can be detected with high sensitivity with the use of scintillation cameras. In addition to being used for clinical imaging, Tc-99m-MDP has been utilized *in vivo* to study the bone response to implants and to osteogenic cytokines [23-26]. The advantages of this tracer are: (1) its safety with little or no influence on cell behavior, and its prospective use in following mineralization with time in the same culture without interfering with the process; (2) its method of detection, which is non-destructive, thus allowing for continuous study of the sample; (3) mineral uptake that occurs within a short period of time, and imaging that is accomplished in minutes; (4) results that can be quantified, facilitating comparative studies. Moreover, due to the specificity of uptake, Tc-99m-MDP is able to distinguish newly formed calcium-phosphate mineral from a pre-existing calcium-containing substrate. This study presents the first use of Tc-99m-MDP

as a quantitative tool for evaluating *in vitro* the mineralization associated with bone cell activity.

The principal objective of this chapter was to determine the utility of the non-destructive labeling of newly-formed mineral with Tc-99m-MDP for the scintigraphic quantification of the amount of mineral formed in cultures of osteoblast-like cells on tissue culture polystyrene (TCPS). The radionuclide findings were validated qualitatively by von Kossa staining and light microscopy and by XEDS used in conjunction with SEM. The quantitative validation was accomplished using a destructive method for the determination of the calcium content of the cultures: inductively coupled plasma (ICP) emission spectroscopy [27, 28]. A second objective was to determine how effectively the scintigraphic method could be used to quantify the mineral deposition mediated by osteoblast-like cells cultured on photon-attenuating substrates, such as titanium-6 aluminum- 4 vanadium (Ti-6Al-4V) disks. A related aim was to determine if there were differences in the mineralization process on Ti-6Al-4V surfaces with polished and matt finishes.

3.2 Selecting the right cell source

3.2.1 Cell harvesting

(1) Human osteoblast cells

Human cancellous (metaphyseal) bone fragments from patients undergoing total knee arthroplasty were harvested under sterile conditions within 2 hours of surgery. The outside soft connective tissue was carefully removed; then the bone was cut into small pieces (2-4 mm^3). After intensive rinsing (phosphate buffered saline (PBS) supplemented with 1% antibiotic solution), these small bone specimens were incubated in 75-ml culture flasks using a medium comprising α-minimum culture medium (α-MEM), 10% fetal bovine serum (FBS), 1% antibiotic solution, and 25 μg/ml ascorbic acid (hereafter called Standard Medium) under standard culture conditions (37 °C, 5% CO_2, and 95% humidity). Cells were harvested by trypsinization after they reached confluence.

Cells were counted by a hemocytometer and then used for further experiment. Extra cells were frozen and stored at -80 °C.

Cells were cultured on TCPS at a density of $4 \times 10^8 / m^2$ in Standard Medium with 50 mM glycerol phosphate and 10 nm dexametasone added (hereafter called mineralization medium) under standard culture conditions (37 °C, 5% CO_2, and 95% humidity). The culture medium was changed every 3 days.

(2) Neonatal mouse osteoblast cells

The calvaria from neonatal mice were excised, stripped of soft tissue, rinsed by PBS solution, and subjected to a series of four 30-min digestions with 0.2% sterilized collagenase aqueous solution. The cells from the first digestion were mostly fibroblasts and osteoclasts, and were discarded. Cells from the remaining three digestions were pooled, washed, and collected. They were then cultured in the Standard Medium under standard culture conditions (37 °C, 5% CO_2, and 95% humidity). Cells were harvested by trypsinization after they reached confluence. Cells were counted by a hemocytometer and then used for further experiment. Extra cells were frozen and stored at -80 °C.

Cells were cultured on TCPS at a density of $4 \times 10^8 / m^2$ in Mineralization Medium under standard culture conditions (37 °C, 5% CO_2, and 95% humidity). The culture medium was changed every 3 days.

(3) Stem cells from canine bone marrow

The marrow was harvested from both the distal anterior femoral metaphysic and the proximal anterior tibial metaphysis. Bone marrow biopsy needles were used to penetrate the cortex of the bone, and 5 ml of marrow was aspirated into a 20ml syringe containing 2 ml Dulbecco's modified Eagle's medium / F12 (DMEM/F12) medium with1000 unit/ml heparin. Three to six 20ml syringe volumes were obtained from each animal. The aspirate from each animal was resuspended with 15 ml of PBS solution and centrifuged at 300 rpm for 5 minutes to remove red blood cells, then centrifuged at 1500 rpm for 15 minutes to

obtain a cell pellet. The pelleted cells were resuspended in 15 ml of PBS and the foregoing process repeated twice. After this procedure, the pelleted cells were resuspended in 15 ml complete medium (DMEM/F12 medium supplemented with 20% fetal bovine serum, 50 µg of ascorbic acid/ml, 1% antibiotics/antimycotics). The cells were cultured at 5% CO_2, 95% humidity, and 37°C in 75 cm^3 flasks. Media were first changed after 3 days, and every other day afterwards. With this method, most of the non-adherent hematopoietic cells were removed. Only the adherent cell population was cultured subsequently. The adherent cell population grew as symmetric colonies. Cells from sub-confluent cultures were detached and collected after approximately 10 days, using aqueous solution of 0.05% trypsin and 0.52 mM EDTA for 5 minutes, and then passed into flasks. Cells were counted by hemocytometer and then used for further experiment. Extra cells were frozen and stored at -80 °C.

Cells were cultured on TCPS at density of 4×10^8 / m^2 in Mineralization Medium under standard culture conditions (37 °C, 5% CO_2, and 95% humidity). The culture medium was changed every 3 days.

(4) MC3T3 cell lines

MC3T3 cells were courteously provided by Dr. Louis Gerstenfeld of Boston University. The cells were first cultured in Standard Medium under standard culture conditions (37 °C, 5% CO_2, and 95% humidity). After reaching confluence, cells were harvested by trypsinization. Cells were counted by hemocytometer and then used for further experiment. Extra cells were frozen and stored at -80 °C.

Cells were cultured on TCPS at density of 4×10^8 / m^2 in Mineralization Medium under standard culture conditions (37 °C, 5% CO_2, and 95% humidity). The culture medium was changed every 3 days.

3.2.2 Cell culture and storage

Normally, cells were cultured in two media: (a) Standard Medium, which is α-MEM, 10% FBS, 1% antibiotic solution, and 25 μg/ml ascorbic acid; and (b) Mineralization Medium, which is Standard Medium plus 50 mM glycerol phosphate and 10 nm dexametasone. The Standard Medium was used to multiply the number of cells to get the quantity needed for the experiment; and the Mineralization Medium was used when cell mineralization wss needed.

Cells were sacrificed and fixed in 1 ml of 2.5% glutaraldehyde aqueous solution for one hour, air dried, and then observed with an environmental SEM (ESEM, XL30, FEI/Philips, Hillsboro, OR). XEDS was performed using the x-ray detector attached to the XL30 ESEM. The detection energy windows were set for calcium, phosphorus, and oxygen in order to produce two-dimensional maps of the location of these elements to superimpose on the secondary electron image.

A storage medium was formulated by adding 10% dimethyl sulfoxide (DMSO) to α-MEM. Cells were stored at a density of 2×10^6/ ml. The container was kept at -20 °C for 3 to 4 fours and then moved to -80 °C. Cells were normally stored at -80 °C for not more than two months, and otherwise discarded.

When frozen cells were needed to be thawed for further use, the cell container was dipped into 37 °C water for about 30 seconds to melt the outer layer of ice. Then, about 1 ml of culture medium was added to the container drop by drop, 5 seconds between each. This slow process was followed to avoid any sudden change of the cell environment. After the ice was thawed, 10 ml of culture medium was added and the whole centrifuged to pellet the cells. Cells were resuspended in 10 ml of culture medium and the centrifuge-resuspension process repeated twice more to remove DMSO. Cells were normally cultured on TCPS for three days to allow for recovery before any further use.

3.2.3 ICP

Inductively Coupled Plasma (ICP), first employed in the early 1960's, is an analytical technique used for the detection of trace metals in environmental samples. The primary goal of ICP is to get elements to emit characteristic wavelength-specific light which can then be measured. This can be achieved by passing the aqueous solution of the tested element through plasma generated with inert gas, whereupon the light emitted by the atoms of the element in the ICP is converted to an electrical signal that can be measured quantitatively. In theory, ICP is able to identify and quantify all elements except argon, which is used for plasma generation. Additionally, ICP is suitable for all concentrations from ultratrace levels to major components. Detection limits generally can range as low as several parts per billion (ppb) to as high as 1 - 100 g / L, depending on the element. One of the largest advantages of employing ICP when performing quantitative analysis is the fact that the analysis can be accomplished very rapidly and with very little sample. A complete multielement analysis can be undertaken in a period as short as 30 seconds, consuming only 0.5 ml of sample solution[29, 30].

ICP was used in this experiment to measure the concentration of calcium in cell culture samples. In detail, 1 ml of 2N nitric acid was added to each dish and then shaken at 4°C overnight. The solution was carefully collected and diluted to 10 ml with distilled water. Then the calcium concentration was tested in an ICP spectrophotometer (Spectro FMD-07). Standard calcium solutions (0, 1, 3, 5, 10, 20, 30, 50 µg/ml) were made by diluting standard calcium solution for ICP (Sigma-Aldrich). A calibration curve obtained from these standard samples is shown in Figure 3-1. Linear fit analysis shows an R value of 0.99996 ($P <$ 0.0001). However, the fitted line didn't go through the origin point (when concentration was zero, the count number was not exactly zero), which implies there was some background noise by the instrument or the sample.
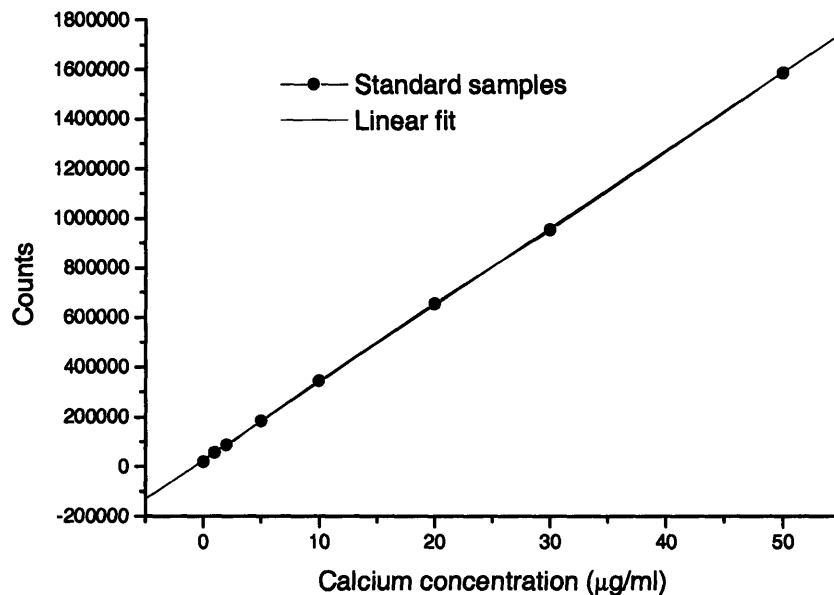
Figure 3-1 ICP calibration curves for calcium standard

3.2.4 Cell comparisons

(1) Mineralization ability and rate

As shown in Figure 3-2(a), after culturing about 6 weeks in the Standard Medium, the cells spread out from the bone and covered the whole culture dish. Cells near the bone were spindle-like and radiated away from the bone. The cells were collected by trypsinization and then cultured in Mineralization Medium. Mineral nodules around 10 μm were formed by these cells on the culture dish after about 4 weeks (Figure 3-2(b)). XEDS and von Kossa staining showed that the nodules were composed of calcium and phosphorus.

This culture method provided a feasible way to obtain human osteoblast cells, and the cells were able to mineralize under proper culture condition. However, the main shortcoming of this method was the long culture time it took for the cells to grow out. The quality of the cells also depends on the patient's age, gender, and health status. Because most patients from whom samples were

derived were seniors undergoing knee or hip surgeries, the activity of these cells was also very limited. This problem was partially addressed by using mouse bone instead bone from human patients. However, the long culture time remained a problem.

In contrast, stem cells demonstrated an ability to multiply quickly. At the very beginning, the cells were scattered on the culture dish floor with a very low density and could scarcely be found under a light microscope. But they multiplied very quickly, and within 10 days the cells reached confluence in the whole culture dish. These cells then were cultured in Mineralization Medium, and they became mineralized within two weeks, as shown in Figure 3-3. Due to their fast multiplication and mineralization ability, stem cells proved a good candidate for the cell culture study.

However, some mineral deposits with anomalous shape were found in the stem cell culture, as shown in Figure 3-4(a). These deposits were large in size (around 20 µm), and higher magnification in Figure 3-4(b) showed them to be composed of many smaller mineral particles, each about 0.5 µm. These mineral particles were constrained within a net of fiber-like tissues. The shape and structure of these deposits were quite different from the mineralization morphology in bone, and also quite different from that produced by other cells in the present study. The anomalous mineralization could be the result of the rapid multiplication of stem cells. The result underscores the fact that the induction of stem cells into osteoblast-like cells is still very hard to control. Bone growth factors and other bone proteins such as bone morphogenetic protein (BMP) could be needed for better control of stem cells.

(a)   (b)
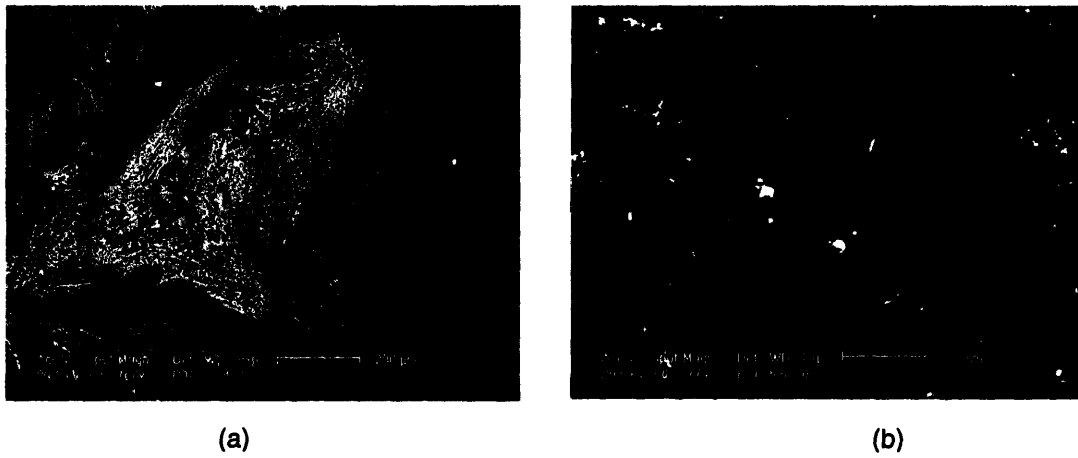
Figure 3-2 (a) ESEM micrographs of outgrown cells from cultured bone; (b) mineralized deposits induced by bone cells cultured on TCPS.
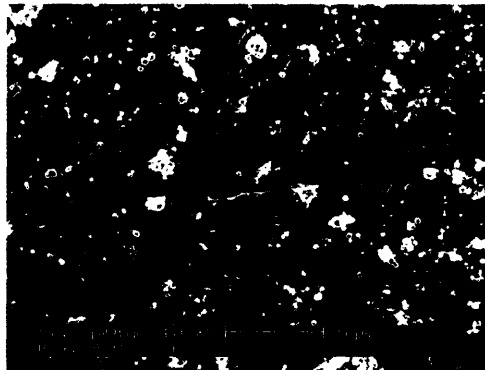
Figure 3-3 ESEM micrographs of mineralized deposits induced by bone marrow stromal cells.

(a)   (b)
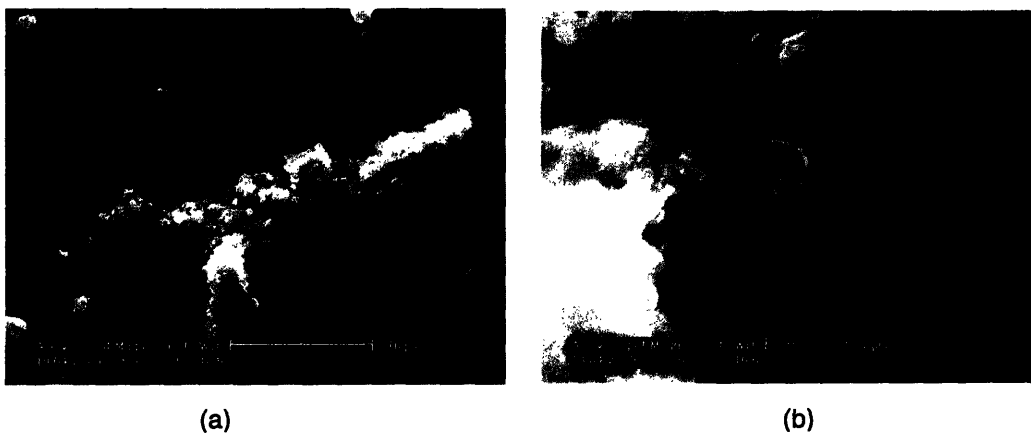
Figure 3-4 Anomalous mineralization induced by bone marrow stromal cells: (a) 3,500X; (b) 20,000X. ESEM micrographs.

Mouse osteoblast cells obtained from collagenase digestion of neonatal mouse calvaria also showed very rapid mineralization. After about two weeks In the Mineralization Medium, mineral nodules, similar to those seen in human osteoblast culture, were found on the culture dish floor (Figure 3-5). Von Kossa staining and SEM study showed that these nodules contained calcium.

MC3T3 cells were supplied frozen in vials and were expanded in Standard Medium. The cells were harvested by trypsinization when confluent and then cultured in Mineralization Medium. Extra cells were stored at -80 °C for future use. The cells began to form mineral nodules after about 3 weeks in culture, as shown in Figure 3-6. The deposits were similar to those seen in human and mouse osteoblasts.

(2) Phenotype stability

Because of their relatively fast mineralization and abundant mineral production, mouse osteoblast cells and MC3T3 cells were selected for further study. The purpose of the further study was to establish the stability of sub-passage cells, to see whether the cell source was stable between different passages and reliable for longer term research.

In the stability study, the amount of calcium produced by these cells was measured by ICP. For primary mouse osteoblast cells, ICP confirmed the observations using SEM. There was a latency period for about one week, in which calcium concentration remained at a very low level and didn't change too much with time. After about one week, the calcium concentration began to increase and attained a high value in about two weeks (Figure 3-7(a)).From a single 35-mm diameter Petri dish, the amount of calcium was as high as 160 µg. However, for the sub-confluent passages, even for the first passage, no significant increase of calcium concentration was seen even after 35 days (Figure 3-7(b)). The total amount of calcium remained lower than 0.1 µg. This result implied that these cells lost their osteoblast phenotype. A possible reason is that the mouse osteoblasts obtained by collagenase digestion were actually a mixture

of different cells, including non-osteoblastic cells like fibroblasts, which might have become the dominant type of cells in the sub-confluent passages.

By contrast, MC3T3 cells were already sub-confluent types, and their mineralization ability didn't change much in different passages. The ICP result for MC3T3 mineralization was similar to that for the primary mouse osteoblasts, only on a different time scale. The latency period for MC3T3 was about 2 weeks, and the calcium concentration reached the peak value at about 5 weeks (Figure 3-8). The total amount of calcium in a single Petri dish was as high as 350 µg . No significant difference was found in the mineralization behavior between different passages.

After comparison of the four cell sources, MC3T3 cells were chosen as the cell source for a quantitative study, because of their normal mineralization behavior, stability, and reasonable mineralization time, as shown in Table 3-1.

Table 3-1 Comparison of four types of cell source.

Cell type	Harvest	Mineral time	Mineral type	stability
Human osteoblast	4~6 weeks	6 weeks	Normal	Not tested
Human stem cells	Complicated process	2 weeks	Anomalous	Not tested
Mouse osteoblast	Collagenase digestion	2 weeks	Normal	Not stable
MC3T3 cells	Gift	3 weeks	Normal	stable
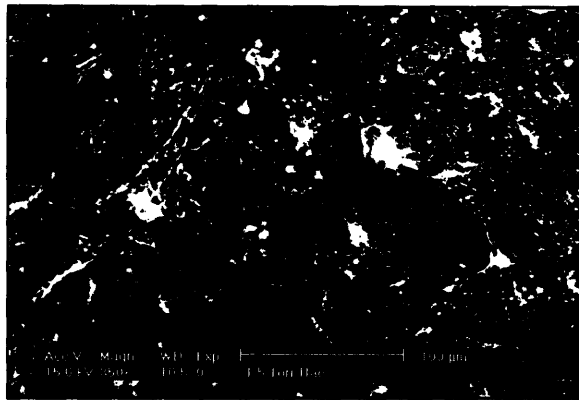
Figure 3-5 Mineralization induced by mouse osteoblast cells on TCPS. ESEM micrographs.

Figure 3-6 Mineralization induced by MC3T3 cells on TCPS. ESEM micrographs.
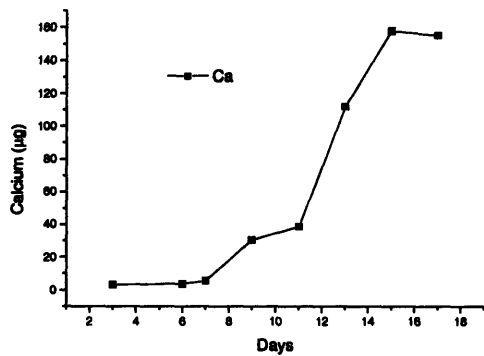
(a)
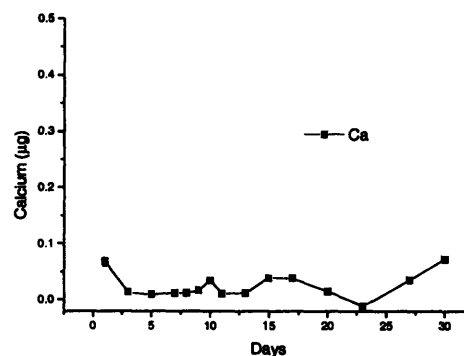
(b)

Figure 3-7 Change in calcium concentration in mouse osteoblast cell cultures on TCPS: (a) primary; (b) passage P1.
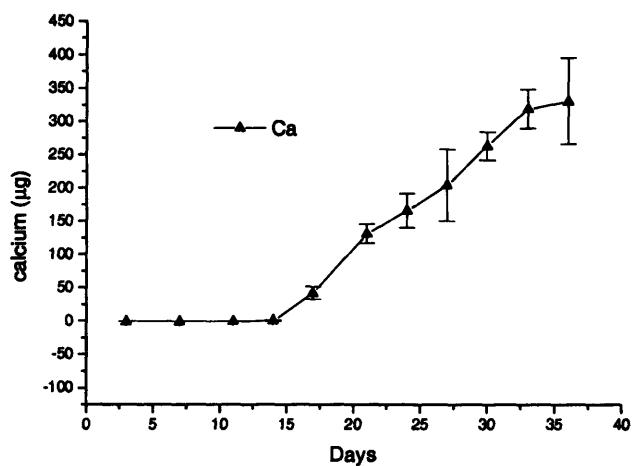
Figure 3-8 Change in calcium concentration in MC3T3 cell cultures on TCPS.

3.3 Quantitative study by Tc-99m-MDP labeling

3.3.1 Qualitative study

MC3T3 cells were seeded onto TCPS dishes (Petri dish, BD Biosciences, San Jose, CA), 35 mm in diameter, with a density of 4×10^8 / m^2 and then cultured in Mineralization Medium at 37°C in 5% CO_2 humidified atmosphere for 3 (n=8), 10 (n=5), and 17 (n=5) days. The culture medium was changed every three days.

At the time of Tc-99m-MDP labeling, culture medium was removed and the TCPS dishes were carefully washed with phosphate buffered saline (PBS). The activity of Tc-99m-MDP was assayed with a dose calibrator (CRC-15R, Capintec, Ramsey, NJ), and a total of 100 μCi Tc-99m-MDP (Bracco, Princeton, NJ) was added to each TCPS dish, diluted to 2 ml with saline and then incubated at room temperature for 2 hours. The Tc-99m-MDP solution was then carefully removed, and the TCPS dishes were washed with PBS solution again three times (for approximately one hour) to remove the unbound radiotracer. The TCPS dishes were placed onto a gamma camera (ECAM Variable, Siemens Medical Solutions, Hoffman Estates, IL) and imaged. Images were analyzed using Siemens software (ESOFT 2.0).

After imaging, cells were fixed in 1 ml of 2.5% glutaraldehyde aqueous solution for one hour. The cells were washed with PBS solution and stored at 4°C for 60 hours to allow for Tc-99m to decay to background levels.

The von Kossa method for revealing calcium deposits in the light microscope utilizes a silver nitrate solution. The calcium in the sample is reduced by strong light and replaced with silver deposits, which are visualized as metallic silver. The unreacted silver ions are removed by sodium thisosulfate. For the von Kossa staining, 1 ml of 5% silver nitrate solution was added to each TCPS dish and the dishes placed in front of a 100-watt lamp for one hour. Samples were then rinsed with distilled water, and 1 ml of 5% sodium thiosulfate was

added for 2 minutes. After rinsing, samples were stained with nuclear fast red solution. Images were taken with a digital camera attached to an Olympus light microscope.

Cell-seeded dishes that did not receive Tc-99m-MDP or von Kossa stain were fixed in 1 ml of 2.5% glutaraldehyde for 1 hour, air dried, and then observed with an environmental SEM (ESEM, XL30, FEI/Philips, Hillsboro, OR). XEDS was performed using the x-ray detector installed on the XL30 ESEM. The detection energy window was set for calcium, phosphorus, and oxygen in order to produce two-dimensional maps of the location of the elements to superimpose on the secondary electron image.

3.3.2 Quantitative study

MC3T3 cells were cultured on TCPS dishes in the mineralizing medium using the same density as in the qualitative study for 7, 14, 17, 20, 23, 26, 29, and 35 days, with n=4. MC3T3 cells were also seeded on TCPS dishes and cultured for 7, 14, 21, 28, and 35 days, with n=4, in a Standard Medium (α-minimum culture medium with 10% fetal bovine serum, 1% antibiotics, and 100 mM ascorbic acid only). The mineralizing and non-mineralizing cultures were imaged using the same methodology as in the qualitative study. A circle was superimposed on the digital images from the gamma camera to select regions of interest (ROI), and theTc-99m uptake was calculated as the average counts/pixel in each ROI.

After imaging, the cell cultures were fixed in glutaraldehyde and stored at 4°C for 60 hours. One ml of 2M nitric acid was added to each dish and the dishes shaken overnight at 4°C. The solution was carefully collected and diluted to 10 ml with distilled water. The calcium concentration was determined using an ICP spectrophotometer (FMD-07, Spectro, Germany). Standard calcium solutions (0, 1, 3, 5, 10, 20, 30, and 50 μg/ml) for calibration of the ICP were made by diluting a standard calcium solution for ICP test (Sigma-Aldrich).

A second experiment was performed for determination of the calcium content only of MC3T3 cells cultured on TCPS for 7, 14, 17, 20, 23, 26, 29, and 35 days, with n=4.

Data are reported as the mean ± standard error of the mean. Statistical analyses were performed using StatView (SAS Institute, Cary, NC).

3.3.3 Study of influence of surface roughness on mineralization

Ti-6Al-4V ELI grade (ASTM F136-92) rod stock (Titanium Industries, Parsippany, NJ), 16 mm in diameter, was machined into 1 mm thick disks. The disks were divided into two groups for surface grinding: one group was ground by 120 grit silicon carbide (SiC) paper only, and another group was ground by a series of SiC papers and finished with 4000 grit SiC polishing paper. These disks were ultrasonically cleaned in ethanol and distilled water. The surface roughness of these disks was measured by a surface profilometer (P-10, Tencor, San Jose, CA). The R_a of the "matt" surface was 300 nm, and for the "polished" surface the R_a was 50 nm.

MC3T3 cells were seeded on the Ti-6Al-4V disks in a density of 4×10^8 / m^2 and then cultured in mineralization medium at 37 °C and 95% CO_2 atmosphere for 7, 14, 17, 20, 23, 26, 29, and 35 days, with n=4. The cells were imaged and then analyzed as described above.

3.3.4 MDP-99m labeling results

One of the samples of the MC3T3 cells cultured on the TCPS in the Mineralization Medium for 29 days was omitted from analysis due to infection.
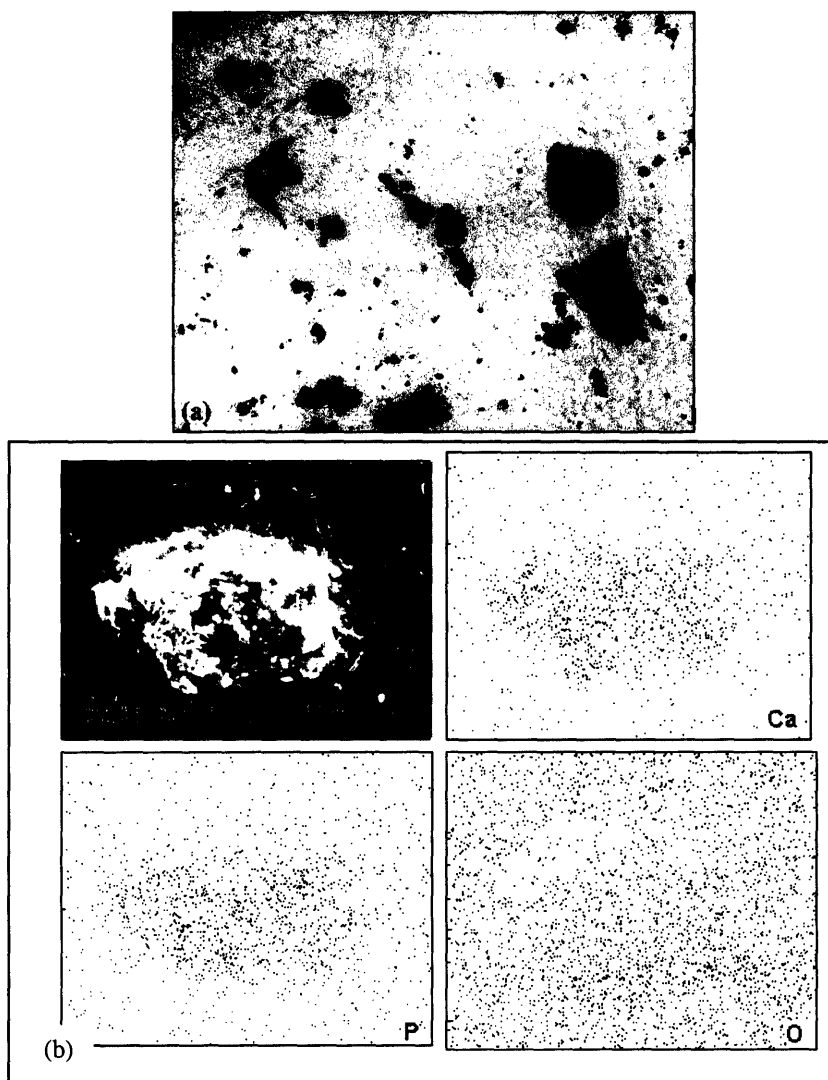
Figure 3-9 Mineralization qualification for a 17-day *in vitro* sample containing
osteoblast-like cells cultured on TCPS: (a) von Kossa staining (100X);
(b) ESEM image (upper left) and corresponding XEDS maps (Ca,
calcium; P, phosphorus; O, oxygen).

The von Kossa staining results (Figure 3-9(a)) showed that MC3T3 cells
cultured on TCPS produced a mineralizing matrix after 17 days of culture in the
Mineralization Medium, confirming prior work with this culture system and method
of staining [31]. Mineral nodules (represented by the opaque silver deposits
using the von Kossa stain method), with maximum extent of about 1 millimeter,
were scattered in the cultures (Figure 3-9(a)). The von Kossa-staining nodules

displayed an irregular surface with a lobulated appearance at higher magnification in the ESEM Spherical features a few micrometers in diameter were found protruding from the surface of the nodules. XEDS confirmed the identity of the nodules as a calcium and phosphorus containing substance. The ubiquitous distribution of oxygen in the sample and supporting platen was demonstrated by XEDS (Figure 3-9(b)).

Tc-99m-MDP scans of the osteoblast-like cells on the TCPS clearly showed an increase in the uptake of the radionuclide with time in culture (Figure 3-10(a)). After 3 days, some uptake was seen principally along the periphery of the dishes (third and fourth rows in Figure 3-10(a)). Single "hot spots" (black spots in the images) could be found in 2 of the 8 samples. By 10 days, there was substantial uptake of the Tc-99m-MDP, with all of the samples showing multiple hot spots distributed through the dish (second row in Figure 3-10(a)). The intensity of uptake increased in the 17-day samples (first row in Figure 3-10(a)), with the hot spots appearing to coalesce to form uniformly labeled areas. There appeared to be a preferential localization of the radionuclide peripherally in all of the samples.
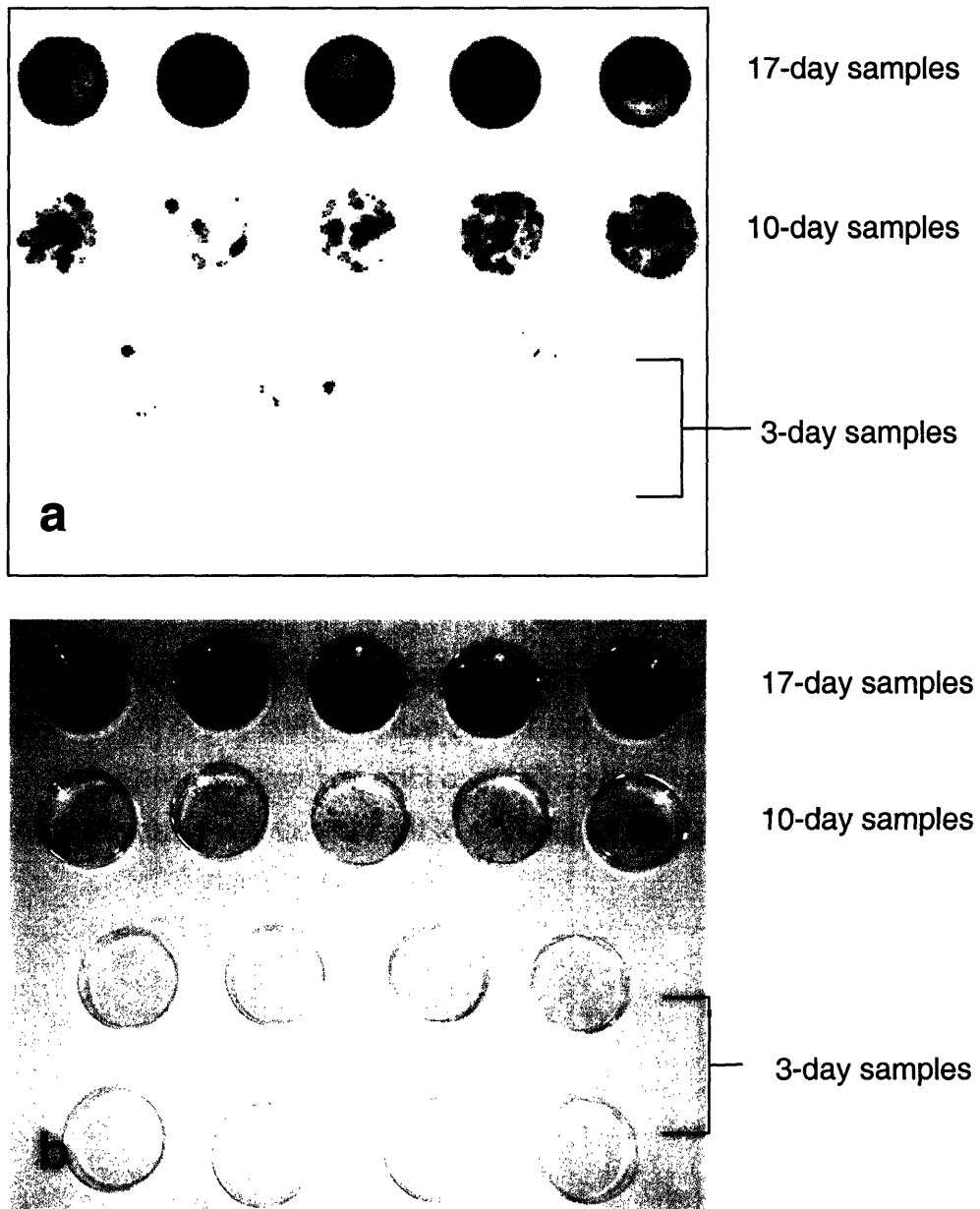
Figure 3-10 (a) Gamma camera images of Tc-99m-MDP uptake by selected
samples for MC3T3 cells cultured on TCPS. From top to bottom, first
row, 17-day samples (5 total); second row, 10-day samples (5 total);
and the third and fourth rows 3-day samples (8 total).
(b) von Kossa staining imaged captured by a digital camera. The
sample identities are the same as in (a).

The von Kossa staining of the 3-, 10-, and 17-day samples for the MC3T3 cells cultured on TCPS also showed an increase in mineralized matrix with culture time (Figure 3-10(b)). At day 3, there was almost no mineral formation (third and fourth rows in Figure 3-10b). By day 10, mineral deposits were evident in all of the cultures (second row in Figure 3-10(b)). The deposits were distributed throughout the dishes with no apparent preference for the periphery as was seen in many of the radionuclide images. After 17 days, there was a substantial increase in the amount of von Kossa staining of the cultures (first row in Figure 3-10(b)).

The kinetics of mineralization, for MC3T3 cells cultured on TCPS (Figure 3-11) and Ti-6Al-4V disks with two surface topographies (Figure 3-13), were determined by evaluating the uptake of Tc-99m-MDP. These data were validated by using the destructive ICP method for measurement of the calcium content of the cultures. As expected, the calcium content of the MC3T3-TCPS cultures grown with the non-mineralizing medium was virtually zero as determined by ICP after 7, 14, 21, 28, and 35 days of incubation (Figure 3-11(a)); the cells achieved confluence after about 2 weeks in culture but did not mineralize. The calcium content was low, with the highest value being about 1.0 µg, two orders of magnitude lower than that in cultures incubated in the Mineralization Medium (see below). In the cultures maintained with the Standard Medium there was no meaningful uptake of the radionuclide (Figure 3-11(a)). The low Tc-99m-MDP signal that was recorded was likely due to background from nonspecific adsorption.
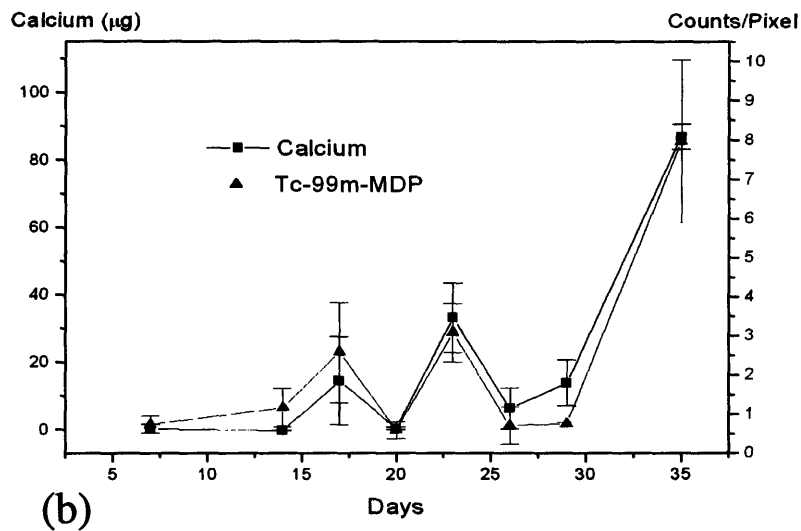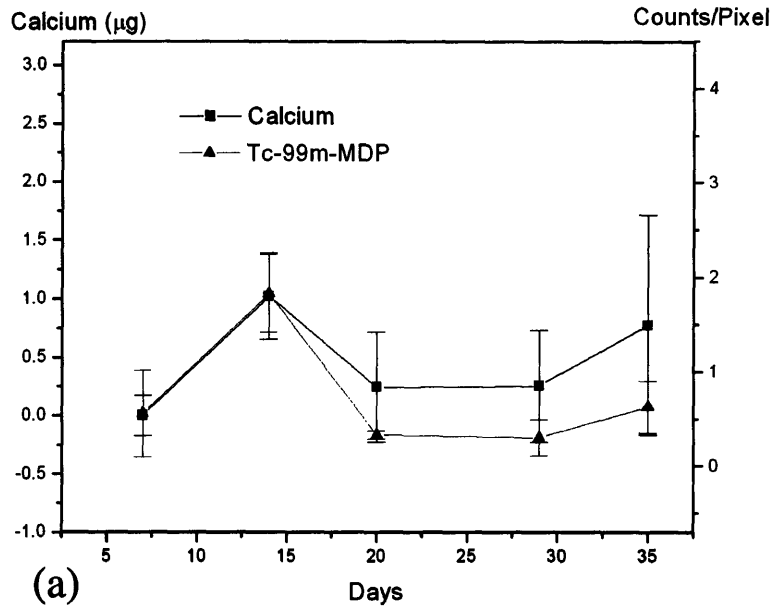
Figure 3-11 Calcium content induced by MC3T3 cells cultured on TCPS. The left vertical axis shows the value of calcium content (in μg) determined by ICP, and the right vertical axis (in a and b) the activity of gamma radiation (in counts/pixel) from Tc-99m-MDP.
(a) Culture in Standard Medium.
(b) Culture in Mineralization Medium.
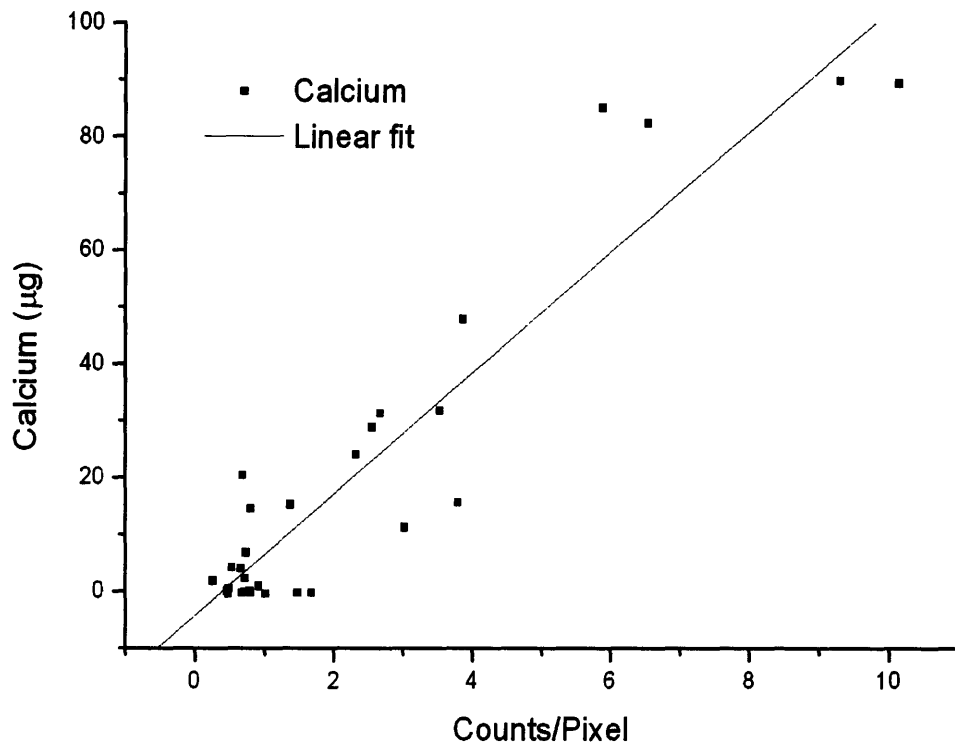
Figure 3-12 Linear regression analysis of the ICP and radionuclide data derived from MC3T3 cells cultured on TCPS in mineralizing medium.
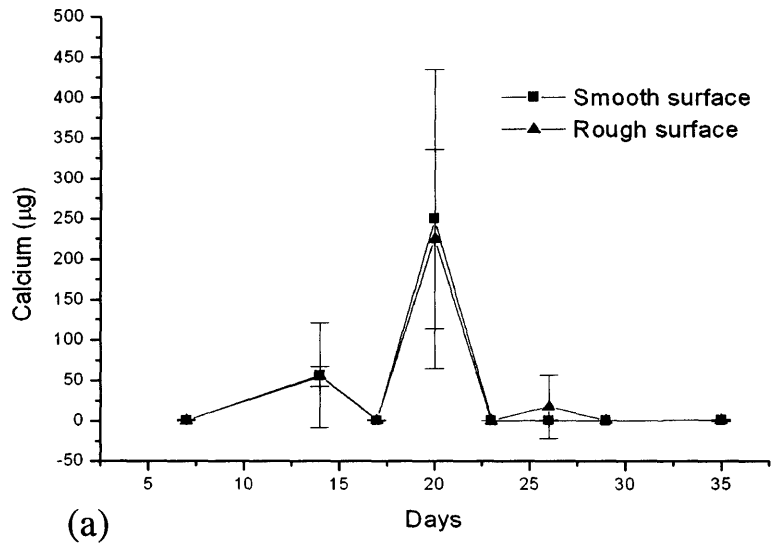
(a)
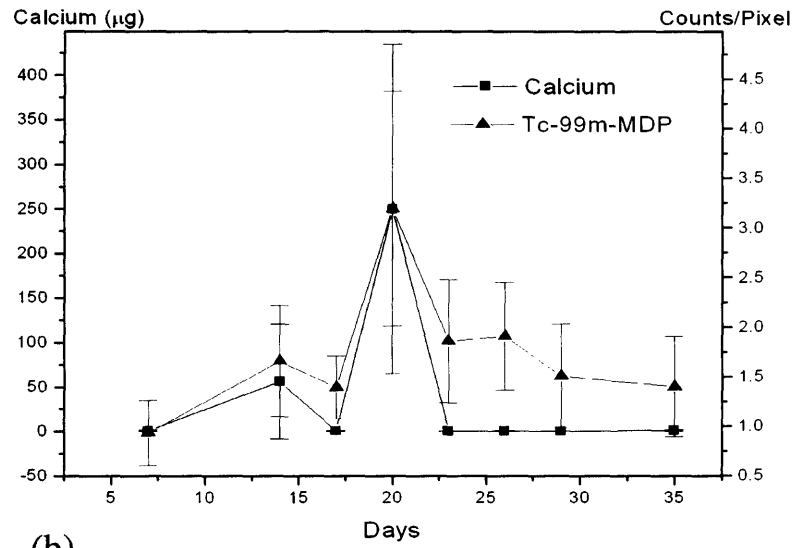
(b)
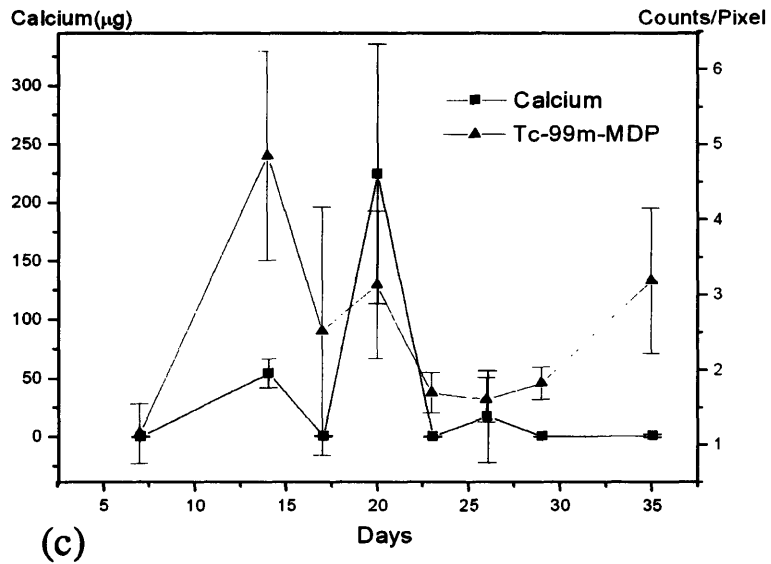
Figure 3-13 Calcium content induced by MC3T3 cells cultured on Ti-6Al-4V disks in Mineralization Medium. The left vertical axis shows the value of calcium content (in μg) determined by ICP, and the right vertical axis (in b and c) the activity of gamma radiation (in counts/pixel) from Tc-99m-MDP.
(a) Calcium content of the cultures on Ti-6Al-4V alloy disks with polished and matt finishes.
(b) Calcium content and radionuclide uptake in cultures on polished Ti-6Al-4V alloy disks.
(c) Calcium content and radionuclide uptake in cultures on the Ti-6Al-4V disks with a matt finish.

In contrast to the cultures in non-mineralizing medium, there was a gradual increase in the calcium content of the cultures grown with the mineralizing medium over the 35-day course of the experiment (Figure 3-11(b)). Of interest was the cyclic nature of the kinetics with reductions in the calcium contents seen at 20 days and then again at 26-29 days (Figure 3-11(b)). One-factor analysis of variance (ANOVA) showed that there was a statistically significant effect of time on the calcium content of the cultures ($p<0.0001$; power=1). Post-hoc testing with Fisher's protected least squares differences (PLSD) demonstrated that the rise in calcium content at 17 days was statistically significant when compared to the 14-day results ($p=0.0055$). The decrease in calcium content at 20 days was also found to be significant by post-hoc testing ($p=0.0076$), as was the subsequent increase at 23 days ($p<0.0001$). This rising and falling of the calcium content of the MC3T3 cultures was not generally seen in previous experiments using this cell line, in which there is normally a gradual increase in the calcium content with no intermittent decreases (Figure 3-8).

Of importance was the fact that the Tc-99m-MDP uptake paralleled the results of the ICP calcium determination, including the cyclic pattern of the results (Figure 3-11(b)). As with the ICP data for calcium content of the cultures, one-factor analysis of variance (ANOVA) showed that there was a statistically significant effect of time in culture on the radionuclide uptake ($p<0.0001$; power=1). Post-hoc testing with Fisher's PLSD showed that the increase in uptake at 17 days was statistically significant when compared to the 14-day results ($p=0.049$). The reduction in Tc-99m-MDP uptake at 20 days was also found to be significant by post-hoc testing ($p=0.0076$), as was the subsequent increase at 23 days ($p=0.0013$).

There was a robust linear correlation between the radionuclide uptake and the calcium content of the cultures. The coefficient of determination, R^2, from linear regression analysis of the calcium content from ICP and the Tc-99m-MDP uptake was 0.88 ($p < 0.0001$; Figure 3-12). The meaningfulness of the

correlation was enhanced by the fact that there was a distribution of values over the range of calcium content up to 100 μg (Figure 3-12). The mathematical expression for the relationship between calcium content determined by ICP and Tc-99m-MDP uptake was:

$$[Ca] = -4.31 + 10.7 \times [\gamma]$$

where [Ca] is the calcium concentration (in μg) and [γ] is the gamma signal (in counts/pixel).

At low calcium concentrations the relation is not likely to be useful, because of the background counts arising from nonspecifically adsorbed Tc-99m-MDP. When the calcium content increases, however, the effect of background is less, and the linear relation between calcium content and radionuclide uptake becomes clear.

The kinetics of the mineral deposition in the MC3T3 cultures on the Ti-6Al-4V disks (Figure 3-13) were different from those found with TCPS. The changes in time of the calcium contents of the cultures on the Ti-6Al-4V disks with the polished and matt surfaces were virtually identical (Figure 3-13(a)). The calcium content of these cultures increased to a peak value at 20 days and then decreased (Figure 3-13(a)). Two-factor ANOVA revealed a significant effect of time in culture on the calcium content ($p<0.0001$; power=1), but no effect of surface finish ($p=0.971$; power=0.05). Fisher's PLSD post-hoc testing confirmed that the increase in calcium content from 17 to 20 days was statistically significant ($p<0.0001$), as was the decrease in calcium content from 20 to 23 days ($p<0.0001$). The radionuclide uptake data for the polished Ti-6Al-4V disks followed a pattern similar to that seen for the calcium content (Figure 3-13b), with an increase in the value from 17 to days of cultured, followed by a decrease in the uptake. One-factor ANOVA revealed that there was a significant effect of time on the uptake of the Tc-99m-MDP ($p=0.038$; power=0.958). Post-hoc testing demonstrated that the rise in the signal from the radionuclide from 17 to 20 days and the decrease from 20 to 23 days were statistically significant ($p=0.0006$ and $p=0.012$, respectively). The absolute scintigraphic values

97

obtained for the cultures using the Ti-6Al-4V disks (Figure 3-13(b)) were lower than those from the cultures on TCPS (Figure 3-11), reflecting the effects of the metal in attenuating the radionuclide signal. This attenuating effect of the metal resulted in a different linear regression expression for the correlation between the radionuclide uptake and the calcium content. The correlation between the radionuclide uptake and the calcium content for the titanium disks (R^2= 0.55) was less robust than for the TCPS surface.

The Tc-99m-MDP uptake in the cultures prepared using the Ti-6Al-4V disks with the matt surface was different from that obtained with the polished metallic samples and did not parallel the ICP data for calcium content (Figure 3-13(c)). The peak value for the uptake occurred at 14 days, and after the subsequent fall in the radionuclide signal there appeared to be an increase again from 29 to 35 days. There was no apparent correlation between the Tc-99m-MDP signal and the ICP results for the cultures prepared using the titanium alloy disks with the matt finish.

3.4 Discussion

The notable finding of this study was that Tc-99m-MDP labeling of mineralizing cultures of osteoblast-like cells could be validated as a useful non-destructive tool to quantify changes in calcium content with time *in vitro*. The linear relationship between the recorded radionuclide uptake and the calcium content as determined by ICP was highly statistically significant (R^2=0.88). This method relies on the adsorption of the radionuclide to the surface of newly formed mineral, and thus may not be of use for the determination of the amount of accumulated mineral after a certain mass (as yet undetermined) is achieved. In the present work the fact that the uptake was so closely correlated with the calcium content would indicate that this mass was not yet achieved.

There are several issues, however, that could limit the utility of this scintigraphic method for certain studies of mineralizing processes *in vitro*. There may be differences in the binding affinities of the radionuclide to the various

forms of calcium phosphate, in addition to hydroxyapatite, that could comprise the deposits *in vitro*, such as amorphous calcium phosphate, octacalcium phosphate, and dicalcium phosphate (brushite). In addition, the secondary attenuation of the gamma photons emitted by the Tc-99m-MDP by selected biomaterials (*viz*, metals) confound interpretation of the quantitative data, and the absolute determination of the calcium content. The effects of the metallic attenuation of the radionuclide signal may explain in part the absence of a high correlation between the calcium content and Tc-99m-MDP uptake from the titanium alloy cultures in the present study.

Since Tc-99m is metastable with a half-life of only 6 hours, Tc-99m-MDP dosage, incubation time, washing procedure, and scanning time need to be accurately controlled if a correlation between uptake and calcium content is to be employed. In addition to being used to calculate the calcium content of newly mineralizing samples, the Tc-99m-MDP labeling may also be of value to quantitatively compare the results from the culture of osteoblast-like cells on different materials. If cells can be cultured equally on various biomaterials and the same labeling and scanning procedures followed, the biomaterials can be compared directly by relying on the gamma signal without knowing the calcium concentration. Special attention also needs to be paid to the washing procedure. Moreover, at low calcium concentration, the background noise from nonspecifically adsorbed Tc-99m-MDP could be an issue.

The finding of rising and falling calcium contents with time for the TCPS cultures (Figure 3-3b) may be explained by a loss of some of the cells and associated mineral deposits with changes of the medium. This behavior is not generally seen with MC3T3 cultures, and probably specific to this particular experimental run. The fact that it did occur, however, was of value in demonstrating how well the radionuclide results followed the changing calcium contents.

There was no effect of the surface roughness of the Ti-6Al-4V disks, in the range evaluated, on the calcium deposition as determined by the ICP method (Figure 3-13a). The loss of calcium after the peak reached at 20 days may have been due to the dislodgement of the cells and mineral and their removal from the cultures during the medium change, as mentioned above. While the Tc-99m-MDP uptake by the cultures on the polished metal specimens paralleled the calcium content, there was no such correlation on the disks with the matt finish. It is possible that mineral was dislodged during the process of fixation and handling after the cultures were terminated and in preparation for collecting the sample for ICP.

The qualitative comparison of von Kossa staining and radionuclide labeling of cultures did not show a clear correlation in the distribution of mineral. Prior work has demonstrated the limitations of the von Kossa method [13] for studies of the mineralization of MC3T3 cultures. In the present study Tc-99m-MDP uptake of cultures appeared to be more sensitive than von Kossa in detecting the earliest mineral deposits.

The scintigraphic technique employed in this study enables several interesting experimental directions. Mineralizing cultures can be labeled and scanned at intervals over a period of time. Information about the mineralization process at different time points can be acquired from the same sample. This could deepen our understanding of mineralization kinetics. Another important study involves the investigation of the effects of selected biomaterial substrates, including calcium-containing materials on the mineralization process. The newly formed crystallites could be distinguished from the pre-existing mineral by Tc-99m-MDP. This information is very difficult to obtain using other methods.

The results of this study support the continued investigation of Tc-99m-MDP for the study of mineralization processes *in vitro*. This radionuclide has been demonstrated to be of great value as a diagnostic imaging tool in the clinic. Its value as a laboratory method warrants further consideration.

3.5 References

1. Flecknell, P., *Replacement, reduction and refinement.* Altex, 2002. **19**(2): p. 73-8.
2. Service, R.F., *Tissue engineers build new bone.* Science, 2000. **289**(5484): p. 1498-500.
3. Beresford, J.N., S.E. Graves, and C.A. Smooothy, *Formation of mineralized nodules by bone derived cells in vitro: A model of bone formation?* American Journal of Medical Genetics, 1993. **45**: p. 163-178.
4. Elgendy, H.M., M.E. Norman, A.R. Keaton, and C.T. Laurencin, *Osteoblast-like cell (MCC3T3-E1) proliferation on bioerodible polymers: an approach towards the development of a bone-bioerodible polymer composite material.* Biomat., 1993. **14**(4): p. 263-269.
5. Kudelska-Mazur, D., M. Lewandowska-Szumiel, and J. Komender, *Human osteoblast in contact with various biomaterials in vitro.* Ann Transplant, 1999. **4**(3-4): p. 98-100.
6. Peck, W.A., S.J. Birge, Jr., and S.A. Fedak, *Bone Cells: Biochemical and Biological Studies after Enzymatic Isolation.* Science, 1964. **146**: p. 1476-7.
7. Bard, D.R., M.J. Dickens, A.U. Smith, and J.M. Zarek, *Isolation of living cells from mature mammalian bone.* Nature, 1972. **236**(5345): p. 314-5.
8. Majeska, R.J., S.B. Rodan, and G.A. Rodan, *Parathyroid hormone-responsive clonal cell lines from rat osteosarcoma.* Endocrinology, 1980. **107**(5): p. 1494-503.
9. Kodama, H.A., Y. Amagai, H. Koyama, and S. Kasai, *A new preadipose cell line derived from newborn mouse calvaria can promote the proliferation of pluripotent hemopoietic stem cells in vitro.* J Cell Physiol, 1982. **112**(1): p. 89-95.
10. Jones, S.J. and A. Boyde, *The migration of osteoblasts.* Cell Tissue Res, 1977. **184**(2): p. 179-93.
11. Friedenstein, A.J., *Precursor cells of mechanocytes.* Int Rev Cytol, 1976. **47**: p. 327-59.
12. Friedenstein, A.J., R.K. Chailakhyan, and U.V. Gerasimov, *Bone marrow osteogenic stem cells: in vitro cultivation and transplantation in diffusion chambers.* Cell Tissue Kinet, 1987. **20**(3): p. 263-72.
13. Bonewald, L.F., S.E. Harris, J. Rosser, M.R. Dallas, S.L. Dallas, N.P. Camacho, B. Boyan, and A. Boskey, *von Kossa staining alone is not sufficient to confirm that mineralization in vitro represents bone formation.* Calcif Tissue Int, 2003. **72**(5): p. 537-47.
14. Boyde, A., *Scanning electron microscopic studies of bone.* Second ed. The Biochemistry and Physiology of Bone, ed. G.H. Bourne. Vol. 4. 1976, New York, NY: Academic Press. 580.
15. Maniatopoulos, C., J. Sodek, and A.H. Melcher, *Bone formation in vitro by stromal cells obtained from bone marrow of young adult rats.* Cell Tissue Res, 1988. **254**(2): p. 317-30.

16. Squire, M.W., J.L. Ricci, and R. Bizios, *Analysis of osteoblast mineral deposits on orthopaedic/dental implant metals.* Biomat., 1996. **17**: p. 725-733.

17. Basdra, E.K. and G. Komposch, *Transmission and scanning electron microscopic analysis of mineralized loci formed by human periodontal ligament cells in vitro.* J Orofac Orthop, 1999. **60**(2): p. 77-86.

18. Yamamoto, M., K. Kato, and Y. Ikada, *Ultrastructure of the interface between cultured osteoblasts and surface-modified polymer substrates.* J Biomed Mater Res, 1997. **37**(1): p. 29-36.

19. Layman, D.L. and R.C. Ardoin, *An in vitro system for studying osteointegration of dental implants utilizing cells grown on dense hydroxyapatite disks.* J Biomed Mater Res, 1998. **40**(2): p. 282-90.

20. Davis, M.A. and A.L. Jones, *Comparison of 99mTc-labeled phosphate and phosphonate agents for skeletal imaging.* Semin Nucl Med, 1976. **6**(1): p. 19-31.

21. Blake, G.M., S.J. Park-Holohan, G.J. Cook, and I. Fogelman, *Quantitative studies of bone with the use of 18F-fluoride and 99mTc-methylene diphosphonate.* Semin Nucl Med, 2001. **31**(1): p. 28-49.

22. Rees, C.R., A.R. Siddiqui, and R. duCret, *The role of bone scintigraphy in osteogenic sarcoma.* Skeletal Radiol, 1986. **15**(5): p. 365-7.

23. Spector, M., W.B. Wigger, and M.G. Buse, *Radionuclide bone imaging of femoral prostheses with porous coatings.* Clin Orthop, 1981(160): p. 242-9.

24. McCracken, M., K. Zinn, J.E. Lemons, J.A. Thompson, and D. Feldman, *Radioimaging of implants in rats using Tc-99m-MDP.* Clin Oral Implants Res, 2001. **12**(4): p. 372-8.

25. Lynch, S.E., G.R. de Castilla, R.C. Williams, C.P. Kiritsy, T.H. Howell, M.S. Reddy, and H.N. Antoniades, *The effects of short-term application of a combination of platelet-derived and insulin-like growth factors on periodontal wound healing.* J Periodontol, 1991. **62**(7): p. 458-67.

26. Aspenberg, P., M. Tagil, C. Kristensson, and S. Lidin, *Bone graft proteins influence osteoconduction. A titanium chamber study in rats.* Acta Orthop Scand, 1996. **67**(4): p. 377-82.

27. Boumans, P.W.J.M., *Inductively coupled plasma-emission spectroscopy.* 1987, New York: John Wiley & Sons.

28. Bagambisa, F.B., U. Joos, and W. Schilli, *Mechanisms and structure of the bond between bone and hydroxyapatite ceramics.* J. Biomed. Mater. Res., 1993. **27**: p. 1047-1055.

29. Traci Bradford, M.N.C., *Inductively Coupled Plasma (ICP)* *http://www.cee.vt.edu/program_areas/environmental/teach/smprimer/icp/icp.html.*

30. Boumans, P.W.J.M., *Inductively coupled plasma emission spectroscopy.* Chemical analysis, v. 90. 1987, New York: Wiley. v.

31. Fratzl-Zelman, N., P. Fratzl, H. Horandner, B. Grabner, F. Varga, A. Ellinger, and K. Klaushofer, *Matrix mineralization in MC3T3-E1 cell cultures initiated by beta-glycerophosphate pulse.* Bone, 1998. **23**(6): p. 511-20.

Chapter 4 Computer simulation of long-term bone loss caused by implantation

4.1 Introduction

Early stages of bone formation on different implant materials were discussed in chapters 2 and 3. For an orthopedic surgery to be successful, it is necessary that strong bone bonding occurs soon after implant. However, even after a successful implant, bone formation and remodeling continues and affects the long term (ten years or more) implant reliability. A serious consideration is the stress distribution on the implant-bone system where "stress shielding" (i.e., regions of the implant-bone systems are under-loaded) causes localized bone loss[1]. A primary cause of stress shielding is the elastic modulus mismatch between implant and bone. Common stem materials have large elastic moduli (e.g, Ti-6Al-4V, 105 GPa, and stainless steel, 200 GPa) compared to the cortical bone surrounding the implant which has a modulus of 30 GPa, and the trabecular bone at the ends of the femur has a modulus of only 3 GPa. After implantation, most of the loading is transferred through the implant instead of the abutting bone material. With stress shielding, the reduced mechanical stress on the bone tissue results in the reduced activity of osteoblasts, the cells in charge of producing new bone material, and a relatively smaller effect on osteoclasts, the cells that destroy existing bone material. In the presence of normal bone resorption by osteoclasts, this reduced osteoblastic activity results in a net loss of bone mass. The decrease in bone density leaves the patient under the risk for both bone fracture and prosthesis failure, which could necessitate a revision arthroplasty to replace the prosthesis[2].

Evidently, the long term reliability of orthopedic surgery will be greatly benefited if the adaptive changes around prostheses could be predicted. Such predictions would result in prostheses designed to be compatible with stresses in the surrounding bone, and thereby to utilize the bone remodeling (the dynamic process in which bone material is destroyed and produced simultaneously) potential of trabecular bone to achieve long term implant fixation. The

103

microscopic stress patterns in bone/prosthesis structures are determined by the external loading conditions and the geometry and material properties of the bones and the prosthesis. Given adequate quantitative descriptions of loading, geometry, material properties and boundary conditions in the structure, the degree of bone-stress abnormality relative to the intact bone can be predicted by computer simulation[3].

Total hip joint replacement is one of the most popular orthopedic surgeries. In this surgery, both the hip socket (acetabulum, a cup-shaped bone in the pelvis) and the head of the femur are replaced by man-made materials[4]. Most bone remodeling happens at the femoral head side because there is more trabecular bone in this side. In this chapter, bone remodeling in the femoral head will be used as an exemplary structure for discussion of bone remodeling.

The structure of the femur, as well as other long bones, is characterized by a dense outer shell and a porous interior (Figure 4-1). The dense shell, called dense or cancellous bone, has a density higher than 90%. The less dense porous interior is trabecular bone, so-called because it consists of a three dimensional network of connected "beams" (trabeculae) whit characteristic lengths of 200 μm. Load transfer within trabecular bone is determined by the density and configuration of the trabeculae with respect to the bone's external load. Dynamic density redistribution or trabecular structural reconfiguration is known as remodeling. Wolff's law, which states that bone will remodel to adapt to environmental loading changes, has been known for 100 years[5].

With the development of computational physics within the last 30 years, many attempts have been made to simulate bone loading and remodeling with the finite element method (FEM)[3, 6-10]. Using ad-hoc optimization algorithms, the FEM simulations could generally reproduce density structures similar to real bone and demonstrate that Wolff's law is consistent with an optimal structure. However, the FEM models treat bone as a continuum and an empirical power-law constitutive relation between bone density and its mechanical properties was

used. This method qualitatively matches experimental results but is necessarily limited to the creation of bone density pattern only. In other words, it can only capture the average stress in a local domain. The stress distribution that pertains to real bone structures would be expected to differ from the continuum treatment, and simulations of bone remodeling that depend on the scale of trabeculae must resolve the stress distribution on the trabecular scale. An accurate determination of trabecular stresses would require that the trabecular microstructural data act as input to a simulation. Such bone architectural data reconstruction could be obtained by either automated serial sectioning[11] or microfocus X-ray computed tomography (μCT) [12]. However, such a reconstruction is practically limited by the numerical cost of the large number of elements required. For example, in a dog bone specimen of 27 mm size, 7.3 million elements would be necessary, so the accurate predication of stress distribution remains a computational challenge[13].
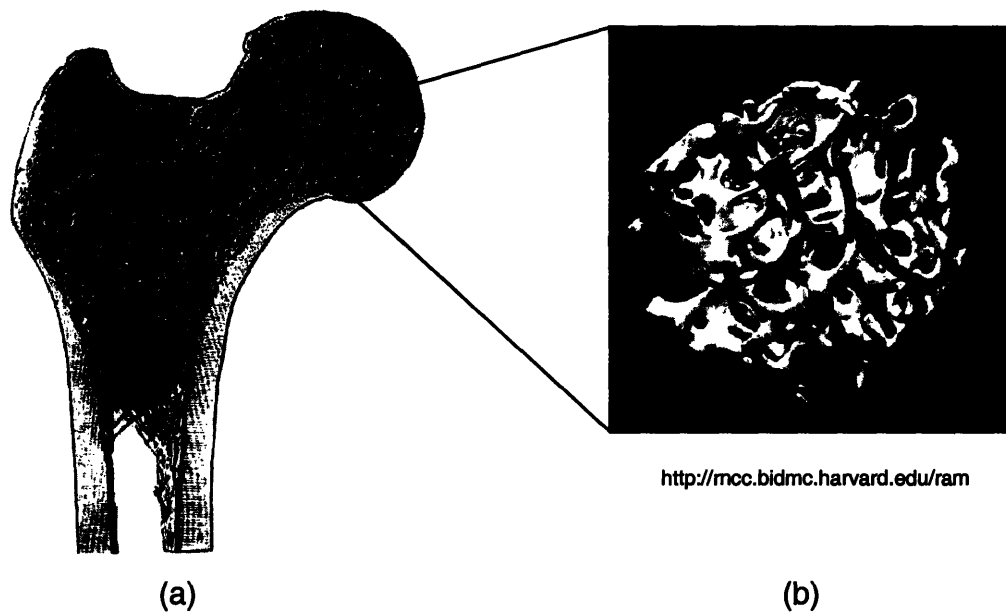

http://mcc.bidmc.harvard.edu/ram

(a)   (b)

Figure 4-1 The structure of femoral head: (a) femoral head; (b) trabeculae.

105

A method of simulating the stress distribution in bone is developed in this chapter. Truss elements are used to simulate the structural characteristics of trabecular bone. Each member of the truss structure represents a single trabecula and element size is set to the trabecular size.

Bone remodeling is reflected in changes in the truss geometry. As a first attempt to reproduce the character of Wolff's law, a strain-energy criterion was used for morphological evolution of the structure. Thus, strain energy density (SED) becomes an optimization function and, as shown below, results in density patterns that are qualitatively similar to Wolff's law and results obtained by FEM of continuum models.

After validating the model for unimplanted geometries, the SED algorithm was used to model the effect of different implant geometries. The stress screening caused by these implants, in which bone material is lost due to the loading change, was predicted by this model. The implications for different implant designs and material properties were also discussed, based on this model.

Using SED as the optimization object and the trabecular width as the optimization variable, an optimal structure with minimum SED was achieved. This structure is similar to real bone in the dense outside, porous inside, and orientation of the trabeculae. After the model reached the optimal state, implants, including total hip replacement and resurfacing, were introduced in this model and compared.

4.2 Materials and methods

4.2.1 Truss bone model

To faciliate comparison with simulation results by other methods, a femoral head with shape similar to that used in reference [14] was used, as shown in Figure 4-2. The height of the femoral head was 100 mm with an 80 mm width. 10,000 nodes were randomly initiated inside the 100 mm by 100 mm box

using the software program Qhull[15]. A closed bone shell structure was introduced into the system by connecting related nodes in the system. Then, the mesh structure was created using the program Triangle[16] by the Delaunay triangulation algorithm. The mesh was generated in such a way that only the mesh points inside the bone were involved. The points outside the bone shell were simply removed. New mesh point could be introduced to avoid concentrated stress, so that the smallest angle in each triangle was forced to be larger than 20°. In total, there were 14,149 nodes after the mesh was created. To faciliate understanding, this mesh generation process is illustrated in Figure 4-3.
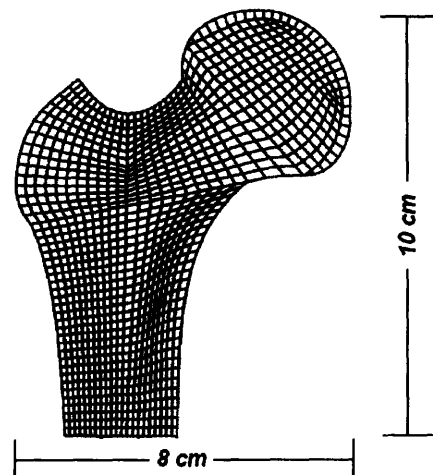
Figure 4-2 Shape of femoral head used in this study.

Each truss connecting two neighboring nodes served as an element to simulate a trabecula. The cross section of each truss element was selected as a square, according to the trabecular bone models by Gibson [17]. The cross section can be other shapes, but the choice doesn't much affect this model, since bending is not considered in this model. A further discussion about this point appears later in this chapter. The initial width of the truss element was chosen to be 50 μm.

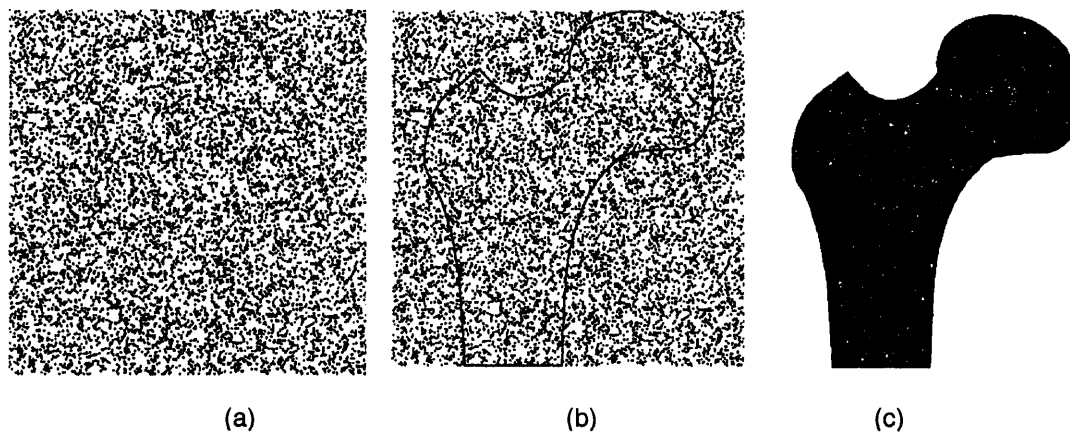(a)   (b)   (c)

Figure 4-3 The mesh generation process: (a) the initial 10,000 nodes; (b)
formation of the bone shell; (3) final truss model.

It was assumed the deformation of the bone model occured under plain strain condition, since the bone model was only a thin slice (50 μm) from the middle part of the bone. Bone's mechanical behavior in general is anisotropic, but this is mainly due to the anisotropic structure of bone. From a material point of view alone, trabecular bone and cancellous bone are the same material with isotropic mechanical properties. Because of the small deformation in normal bone, the material of each truss element was chosen to behave elastically with a Young's modulus of 18 GPa[18].

The mesh structure created in this way was called the ground structure as shown in Figure 4-4. The node at the left lower corner was fixed in both x and y directions, other nodes at the bottom were fixed in y direction and could only move in x direction, and all other nodes were able to move in both x and y directions freely.

The loading on a real bone is very complicated and changes with different activities. However, since bone remodeling is not a process with instant response (normal bone remodeling takes weeks and even months), an average loading that represents three main activities in daily life was used (Table 4-1)[14]. The loading condition used was shown in Figure 4-4.

108

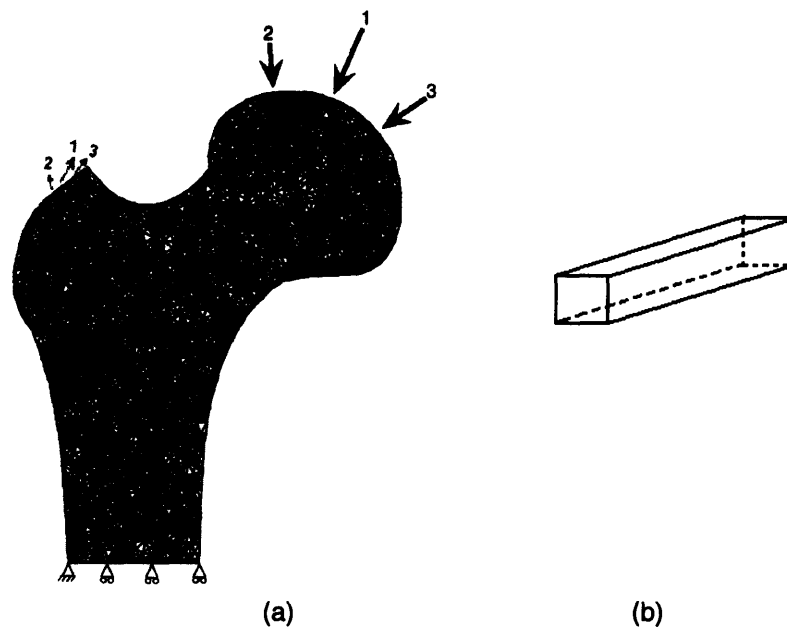The total volume of the system was kept fixed. Only the width of the truss element was a designable variable.

(a)   (b)

Figure 4-4 (a) ground structure; (b) a single truss element

Table 4-1 Loading conditions

| load case | joint reaction | | abductor reaction | |
	magnitude (N)	orientation	magnitude (N)	orientation
1	2,317	24°	703	28°
2	1,158	-15°	351	-8°
3	1,548	56°	468	35°

1. single limb stance; 2. abduction; 3. adduction.

4.2.2. Remodeling equation

The trabecular remodeling mechanism is not yet fully understood yet. However, there is ample evidence that the bone remodeling rate is closely related to the strain energy density of each trabecula. The remodeling is controlled by the activity of both osteoblasts and osteoclasts. In regions with high

strain energy density, the activity of osteoblasts is also high and net bone mass is gained, and *vice versa*. The final result of bone remodeling is that bone has a very uniformly strain energy density distribution, i.e., bone becomes an optimal structure in term of its total strain energy, which is shown in the functionalized representation (4-1)

$$\min_{u,v} \frac{1}{2} f^T u$$

subject to:

$$S(v)u = f$$

$$\sum_{i=1}^{m} v_i = V$$

$$v_i \geq 0, i = 1,...,m$$

(4-1)

Here f is the loading, u is bone's deformation, and $\frac{1}{2} fu$ is the strain energy of this system. There are m truss elements in the system, and for each element the volume is v_i ($i = 1, ..., $ m), which is non-negative. The total volume of the system is a fixed value, V. The constitutional function connects the loading and deformation of the system by the global stiffness matrix $S(v)$, which is symmetric positive semi-definite (SPSD) and a function of the volume v.

For each truss element, the stiffness matrix is S_i,

$$S_i = \frac{A_i E}{L_i} \begin{bmatrix} c^2 & sc & -c^2 & -sc \\ sc & s^2 & -sc & -s^2 \\ -c^2 & -sc & c^2 & sc \\ -sc & -s^2 & sc & s^2 \end{bmatrix}$$

(4-2)

where s and c are abbreviations for $\sin\theta$ and $\cos\theta$, respectively. θ is the angle between the truss element and x axis. Since the coordinates of nodes are fixed, so L_i and θ don't change, and E is a constant, the stiffness is only related to A_i, the cross section area. As discussed before, bending is not considered in the model, so the shape of the cross section area does not matter. As long as the cross section area is the same, for any shape, the stiffness matrix should be the same.

110

The following optimal condition is achieved, proven as in [19]:

$$u^T S_i u = \Lambda, \text{if } v_i > 0,$$
$$u^T S_i u \leq \Lambda, \text{if } v_i = 0, \qquad (4\text{-}3)$$

which means that all the beams have to have the same strain energy density Λ; otherwise, the volume of the element has to be zero. It can also be proven that the total non-zero elements for a system cannot be more than the number of degrees of freedom of the system[19].

Since the global stiffness $S(v)$ and the stiffness matrix of each element $A_i(v_i)$ are SPSD, a natural method for solving this optimal problem is:

$$\Delta v_i = R v_i (E_i - E_0) \qquad (4\text{-}4)$$

where Δv_i is the change of element i, R is a constant, and E_i is the strain energy density of element i, and E_0 is the average strain energy density of the system. This means that for a beam with a higher strain energy density than average, it will require more material to decrease the energy density (growth), and *vice versa* (resorption).

One advantage of this method is that

$$\Delta v = \sum_i \Delta v_i = \sum_i R v_i (E_i - E_0) = R \left(\sum_i v_i E_i - E_0 \sum_i v_i \right) = 0$$

The fixation of total volume is automatically satisfied.

This simple method can be proven to converge:

(I) $\sum\limits_{i=1}^{m} (v_i+\Delta v)A_i(u+\Delta u)=f$

$\sum\limits_{i=1}^{m} v_i A_i u + \sum\limits_{i=1}^{m} v_i A_i \Delta u + \sum\limits_{i=1}^{m} \Delta v_i A_i u + \sum\limits_{i=1}^{m} \Delta v_i A_i \Delta u = f.$ We know $\sum\limits_{i=1}^{m} v_i A_i u = f$, and ignore h.o.t.

$\sum\limits_{i=1}^{m} v_i A_i \Delta u = -\sum\limits_{i=1}^{m} \Delta v_i A_i u$

(II) $(u+\Delta u)^T \sum\limits_{i=1}^{m}(v_i+\Delta v)A_i(u+\Delta u) - u^T \sum\limits_{i=1}^{m} v_i A_i u$

$=2u^T \sum\limits_{i=1}^{m} v_i A_i \Delta u + u^T \sum\limits_{i=1}^{m} \Delta v_i A_i u + h.o.t.$

$=-u^T \sum\limits_{i=1}^{m} \Delta v_i A_i u$

$=u^T R \sum\limits_{i=1}^{m} v_i (E_0 - E_i) A_i u$

$=R \sum\limits_{i=1}^{m} v_i (E_0 - E_i) u^T A_i u$

$=R \sum\limits_{i=1}^{m} v_i (E_0 - E_i) E_i$

$=R \sum\limits_{i=1}^{m} v_i (E_0^2 - E_i^2) \leq 0$

and the convergence speed is:

$R\sum\limits_{i=1}^{m} v_i (E_0^2 - E_i^2)/(VE_0) \propto R$ when close to the solution $(E_i, E_0 \sim E^*)$,

However, because of higher order term, R cannot be too big.

This method can be further improved by:

Remodeling equation :
$$\Delta v_i = Rv_i(E_i^P - E_i^P)$$

The convergence speed is :   (4-5)
$$R\sum\limits_{i=1}^{m} v_i (E_0^{P+1} - E_i^{P+1})$$

Here P is a positive number. When P equals to one, it is the special case just discussed above. Since the method will converge for all positive P (with proper R), carefully choosing R and P can accurately simulate the remodeling

speed in real bone. However, due to the lack of sufficient experiment data and the complexity of bone structure and loading, the values of R and P selected in this thesis are not accurate enough to achieve this purpose. This situation can be improved upon in future simulations.

For all P not equal to one, the total volume change in every iteration can not guaranteed to be zero, so adjustment has to be made at every iteration. The volume of each beam has to be multiplied by the ratio of the original total volume to new total volume, so that the total volume still remains unchanged. This operation could be problematic, especially at the first several iterations when the volume changes dramatically, but generally does not affect the final convergence, as shown later in this chapter.

The optimal problem (4-1) can also be solved by other methods (e.g., penalty-multiplier method (PBM) [20]). However, these methods can only give the final solution to the problem and cannot illustrate the change of bone mass distribution with time; such methods were therefore not utilized in this study.

As mentioned earlier, it can be proven that at convergence for a system with n degrees of freedom the nonzero truss element cannot be more than n, and all the nonzero elements have the same strain energy density; hence, the program should not stop until every nonzero element has the same energy density. However, this is clearly not the situation for real bone. As suggested by Carter(1984), bone is assumed to be "lazy", i.e., a certain threshold in over- or under-loading must be exceeded before bone reacts to the strain energy changes. This is illustrated in Figure 4-5.
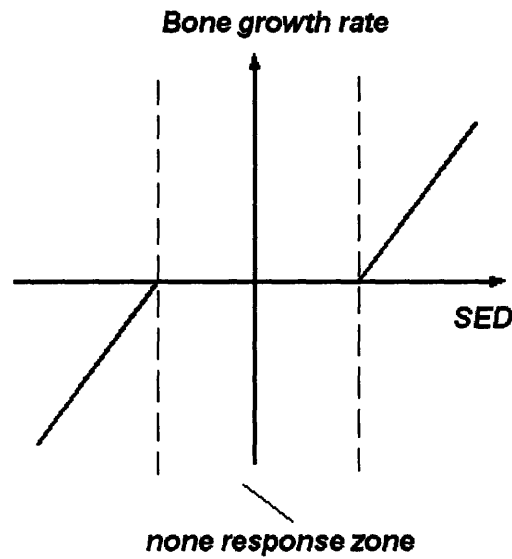
Figure 4-5 The relation between bone growth rate and SED.

For this purpose, two flag values were defined. The first, flag1, is the ratio of the lowest truss strain energy density to the average system strain energy density; and the second, flag2, is the ratio of highest truss strain energy density to the system strain energy density. But since, in this algorithm, the size of the truss element can be infinitely close to but not zero, those small volume truss elements can have very low strain energy density. Although their effect on the system may be negligible, they could have significant effect on the flag values; so a threshold value has to be used, and only the truss elements with volume larger then 1/100 of the original volume should be counted in calculating the flag values. The program stops when flag1 is larger than 0.5 and flag2 is smaller than 2, which means that all the truss elements with adequate volumes will fall in the "non-reaction" region.

4.2.3. Bone density

Although bone is a porous structure and not a continuum, for convenience bone porosity is often characterized by its density. Part of the reason is that bone under X-ray imaging appears to be a dense material, and the density can be

quantified in X-ray imaging. This is also the reason why most bone simulations are continuum models, with bone density often used as the system variable. In this simulation, in order to compare with X-ray imaging and other researchers' simulation results, the truss model has been converted into a continuous model. The method is briefly explained below (Figure 4-6).

In a triangle, for the three elements with side length a, b, and c, and the width of each element w1, w2, and w3, the volume of each side is v1, v2, and v3, respectively:

The total area $A = \sqrt{\dfrac{a+b+c}{2} \bullet \dfrac{a+b-c}{2} \bullet \dfrac{a-b+c}{2} \bullet \dfrac{-a+b+c}{2}}$

and the total volume $V \approx v1 + v2 + v3$

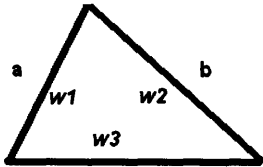The bone density $\rho = \dfrac{V}{2A}$

Figure 4-6 Density transfer from truss to continuous model.

The reason that, in calculation of the density, the area A is multiplied by 2 is that every truss is shared by two triangles.

4.2.4 Implantation

After the bone model archived the stable state, different implants were introduced into the system (Figure 4-7). In like manner to bone, the "triangle" program was used to create the mesh structure for these implants. However, because of the dense nature of these implants, triangle elements were used instead of the truss elements to represent the implant. The generation of implants includes two steps: removing old bone and forming bonding between bone and implant. All the nodes and truss elements inside the implant region were removed. For a truss element which intersects with the implant (which means one node inside the implant and another one outside the implant), the part inside the implant was cut and a new node was formed on the boundary of the implant, at the point where the truss and implant intersect. This node was shared by both

115

the bone system and the implant, by which construction a bonding between bone and implant was formed.
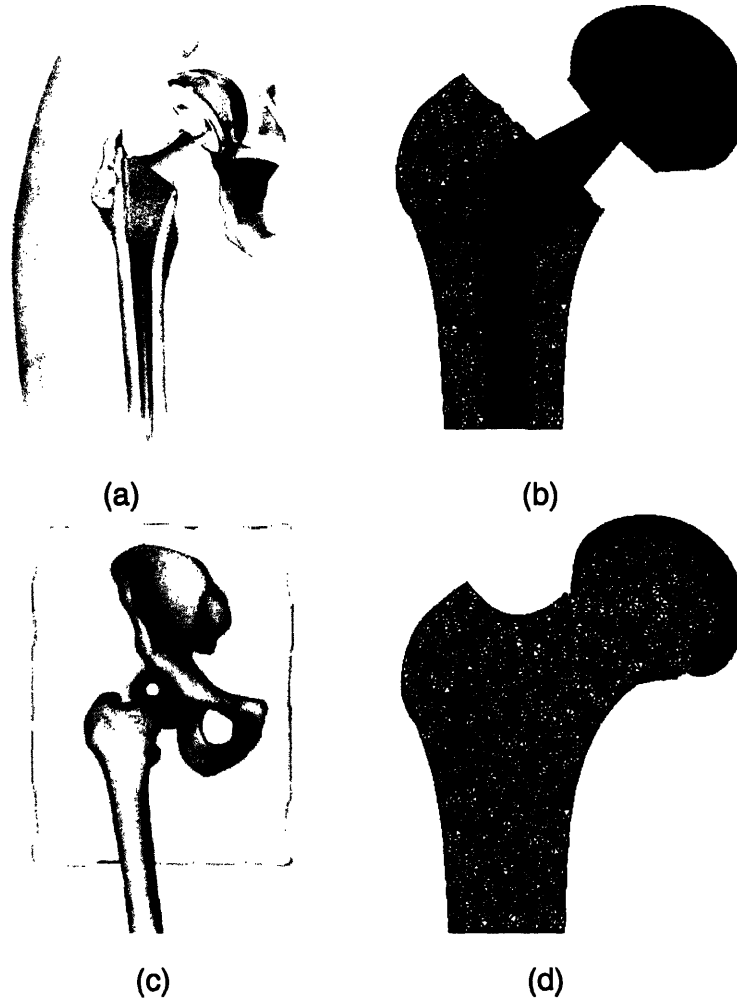

(a)

(b)

(c)

(d)

Figure 4-7 (a) Total hip replacement (THR)[21]; (b) the truss model for THR; (c) hip resurfacing[22]; (d) the truss model for hip resurfacing.

4.3. Results

4.3.1 Convergence and convergence speed

Figure 4-8 shows that the average system strain energy (and, due to the fixed volume, the total strain energy density of the system, too) decreased with the iterations when P equals 1 and R equals 0.1 E_0 (It was noticed that E_0, the average strain energy density, changed at every iteration). The average energy density dropped very quickly at the beginning, because the energy density for each beam was widely distributed and the difference to average strain energy density was large; however, after a period of time, the energy density of each beam became very similar and the change at each iteration was very small.
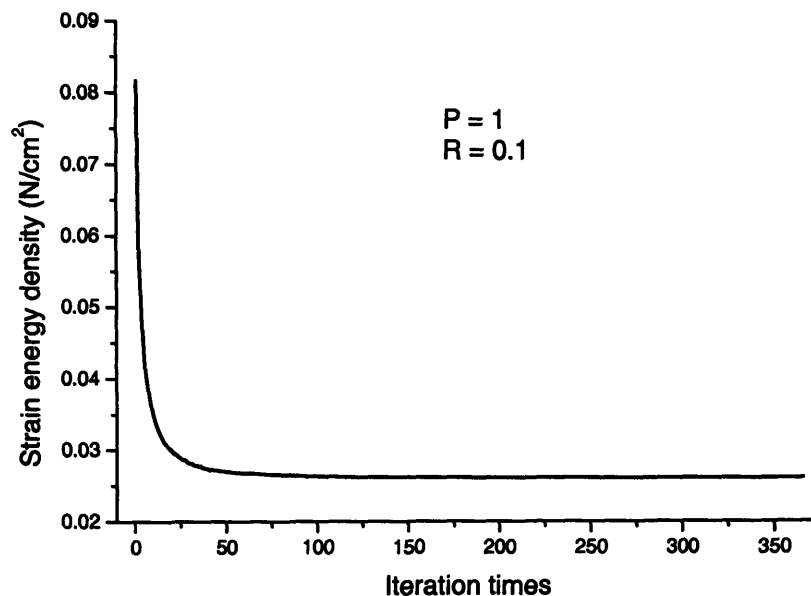
Figure 4-8 Average system strain-energy density vs. iteration time (P = 1, R = 0.1).
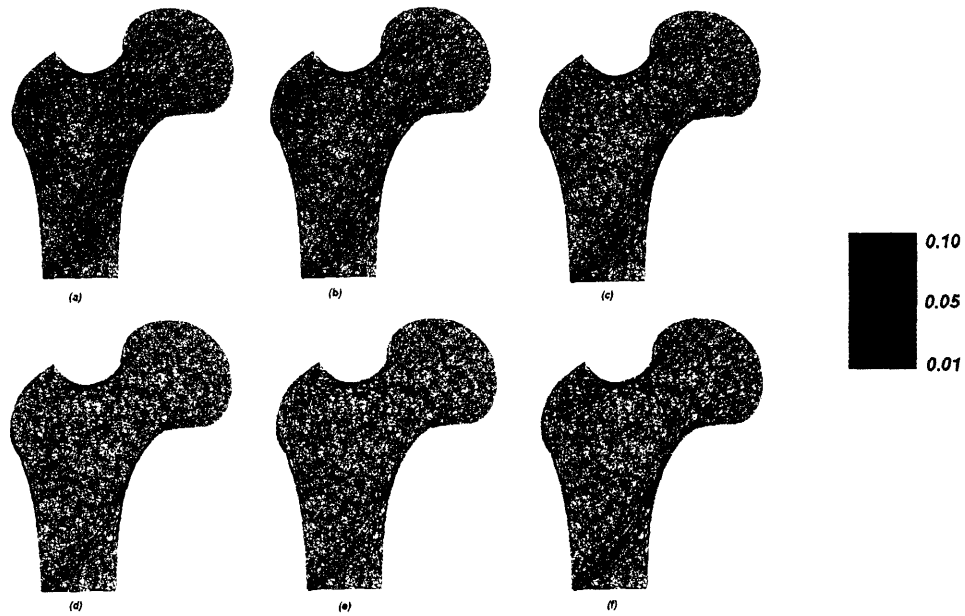
Figure 4-9 The strain-energy density distribution when average SED equals (a)
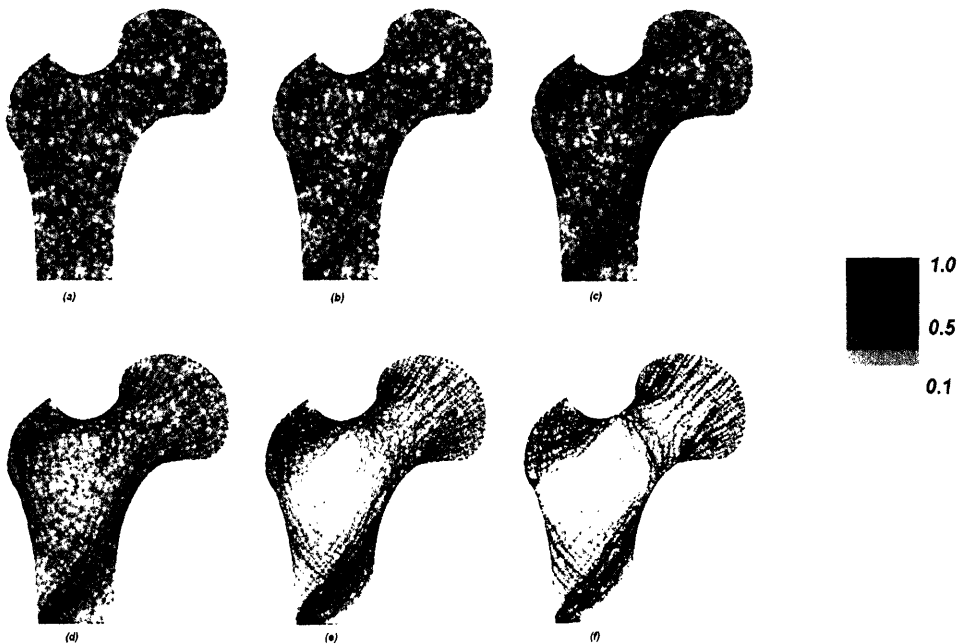0.08, (b) 0.06, (c) 0.05, (d) 0.04, (e) 0.03, (f) 0.26 N/cm^2.

Figure 4-10 The bone density distribution when average SED equals (a) 0.08, (b)
0.06, (c) 0.05, (d) 0.04, (e) 0.03, (f) 0.026 N/cm^2.

The change of the bone strain energy density is shown in Figure 4-9. It can be seen that with the decrease of the system strain energy, the strain energy density of each truss element became similar (the same color in the simulation representation). The overloaded truss elements (with a strain energy density higher than system average) were receiving more bone material to lower their energy density; and for those without enough loading, their volumes were becoming smaller to increase their strain energy density. At the final state of the calculation, a structure with very uniformly distributed stain energy density was obtained. It can also be seen that, at this time, the model had a structure very similar to that of real bone, which is characterized by a low density central portion and a dense outside shell.

This morphology is further revealed in the bone density distribution (Figure 4-10). At first, the bone density was randomly distributed (however, not uniformly; local concentrated regions can be seen), and then the regions with higher strain energy density began to receive more bone materials and became denser. The final state of the density distribution matches very well with the energy density distribution, shown in Figure 4-9. A very important characteristic of the density distribution, which also can be seen in the strain energy distribution, is that trabeculae were perpendicular to each other, following the stress conducting direction. This matches very well with "Wolff's law": the trabeculae align with the local principal stresses (which are normal to each other) to optimize the bone structure. This is the first time this phenomenon has been observed in a continuous model.
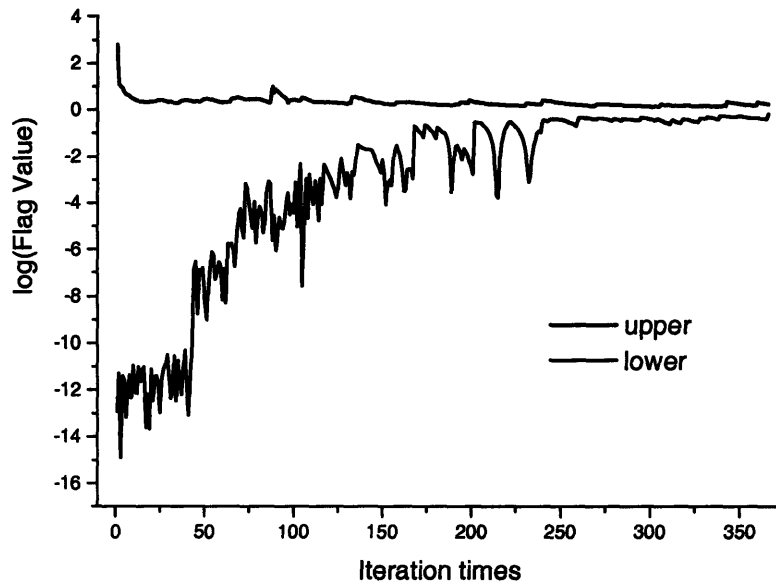
Figure 4-11 Flag values vs. iteration times.

Figure 4-11 depicts the change of flag values with iteration times. The flag1 value was extremely small ($10^{-15} \sim 10^{-11}$) at the very beginning. This is because that the volumes of these low strain energy truss elements were still larger than the threshold value, 1/100 of the original volume. Their volumes decreased by 1/10 every time (R = 0.1, and their strain energy densities were almost zero), so after about $\ln(0.01)/\ln(0.9) = 43$ iterations their volumes were smaller than the 1/100 of the original volume and dramatic increase of flag1 value could then be seen. In contrast, the flag2 value dropped very quickly from outset and soon became less than 2.0. Both of these two values approached the average system energy density after about 350 iterations, where the calculation stopped.

4.3.2 Effects of P and R

(1) P = 1

When R equals 0.01, the system converged very slowly (Figure 4-12). It took more than 2000 iterations for the system to converge (not fully shown in Figure 4-12). The convergence speeds for R = 0.1 and R = 0.2 were by contrast, very fast, with convergence at 255 and 136 iterations, respectively.
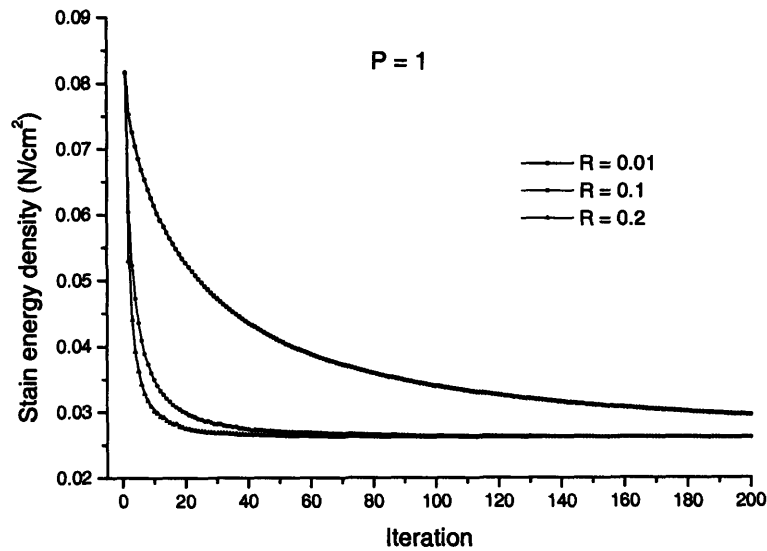

Figure 4-12 The effects of different R values (P = 1).

(2) P = 2

Compared to the P = 1 behavior, it can be seen that the convergence speed for P = 2 increased dramatically (Figure 4-13). However, for R = 0.1 and R = 0.2, the system strain energy density increased after 2 iterations. This result is caused by adjustment of the volume, as mentioned before.
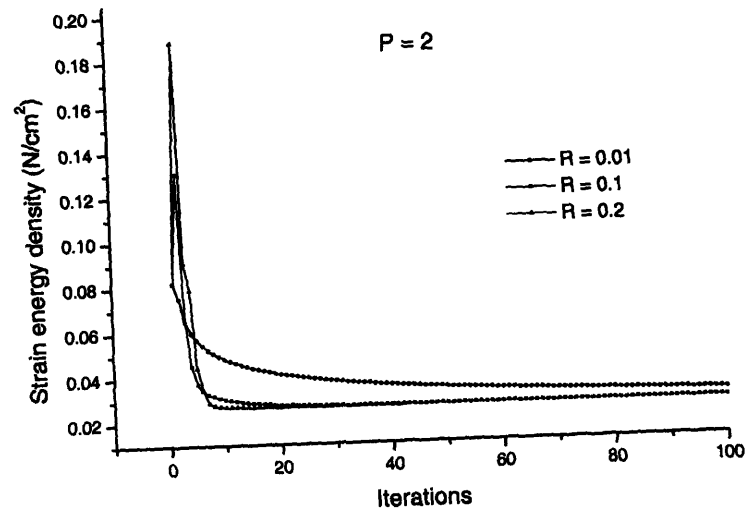
Figure 4-13 The convergence when P = 2.

(3) P = 3

When P = 3, the calculation wouldn't converge even for R = 0.001 (Figure 4-14). This failure is because the system changed too much. When R is small enough, the calculation is able to converge, however very slowly.
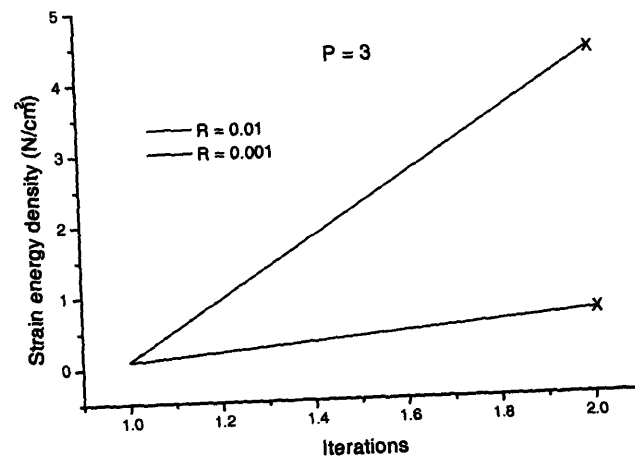

Figure 4-14 Failure of calculation to converge when P = 3.

4.3.3 Implant

After the system reached convergence, implants were introduced into the system. Here two types of implant are discussed: total hip replacement (THR) and hip resurfacing.

(1) Total hip replacement

In a total hip replacement, both the femoral head and the pelvis socket are replaced with artificial implants. But since most bone remodeling happens at the femur, only the femoral side of the total hip replacement is discussed in this chapter.

The material considered for the implant was Ti-6Al-4V alloy with Young's modulus 105 GPa. The implantation began from a stable bone structure (time 0). It can be seen from Figure 4-15 that the system strain energy jumped from 0.026 N/cm^2 to 0.21 N/cm^2, because the stress distribution was greatly changed by the implant and the bone structure now was far from its optimal state. But, thereafter the bone remodeling started, and the system strain energy kept decreasing and finally stayed stable at a value about 0.0117 N/cm^2, less than half of the value before implantation. The result clearly proved that the implant greatly affected the loading distribution on the bone. Because most of the load was conducted through the implant, the final system strain energy density was much lower than that of a normal bone.

Figure 4-16 and Figure 4-17 show how the strain energy density distribution and bone density distribution changed with iteration time. Because of the implant, the bone gained some material in the upper left part and bone material lost from the lower right region.
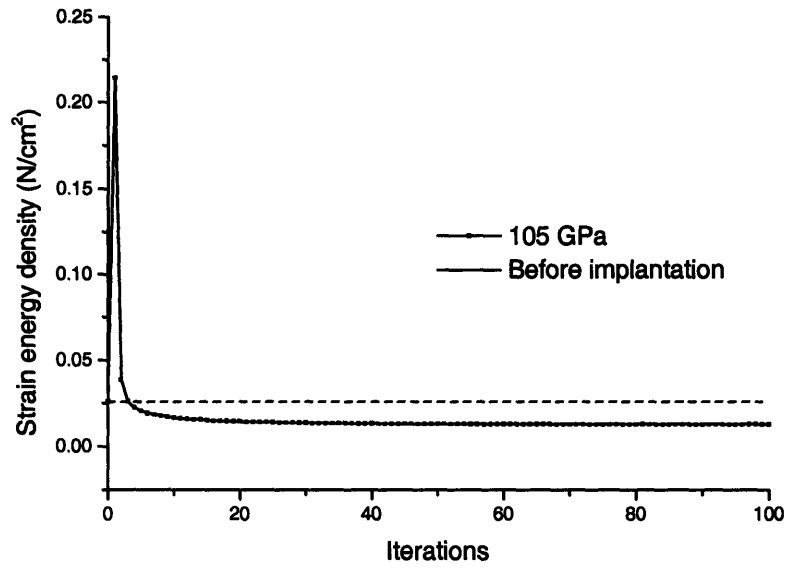
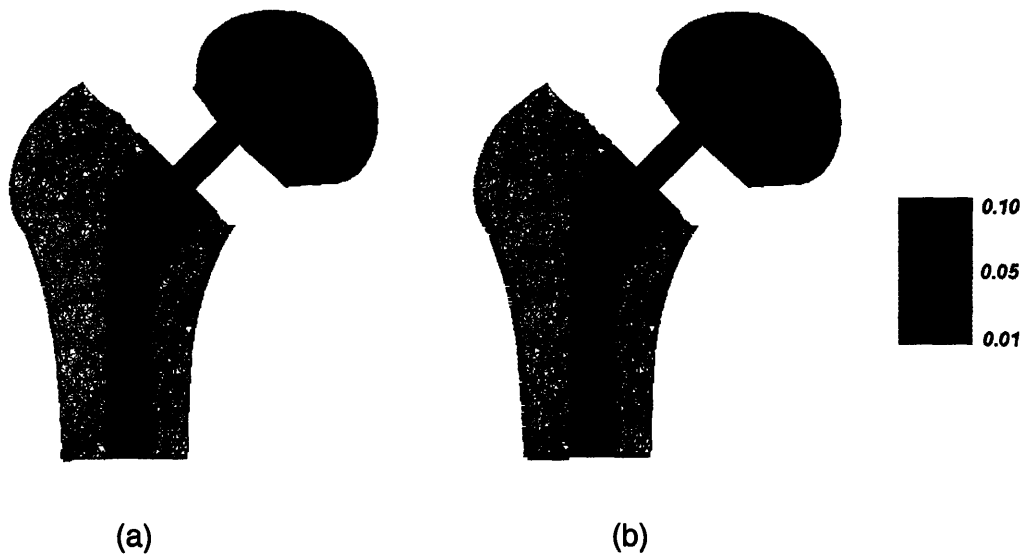**Figure 4-15** Strain-energy density vs. Iterations after implantation.

(a)   (b)

Figure 4-16 Strain-energy density distribution (N/cm^2) (a) immediately after the implantation; (b) at a late stage of implantation.
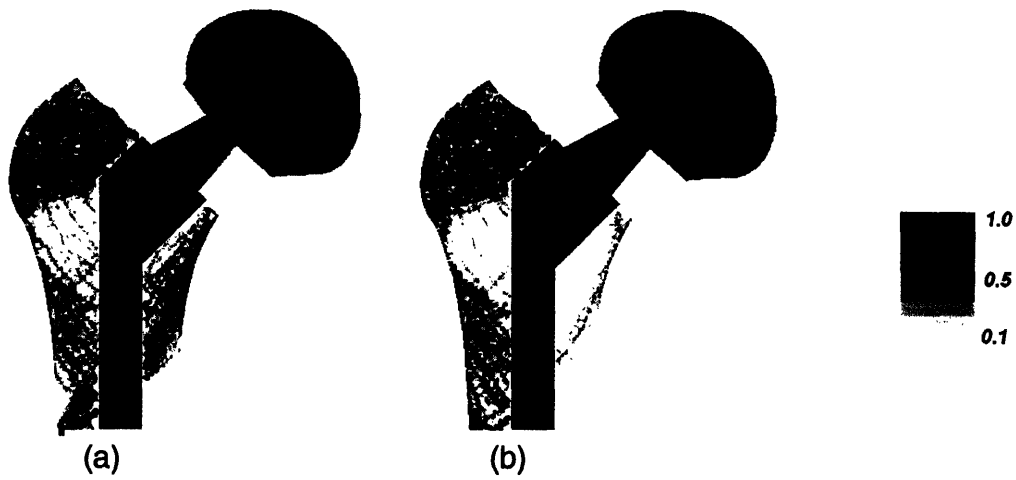
Figure 4-17 Bone density distribution (a) immediately after the implantation; (b) at a late stage of implantation.

The effects of different Young's moduli are shown in Figure 4-18. Basically, the strain energy density decreased with increasing Young's modulus. However, even when the implant had a Young's modulus equal to that of bone (18 GPa), it still had a lower SED than the bone before implantation. It is because that the implant was dense and much stiffer than the porous bone.
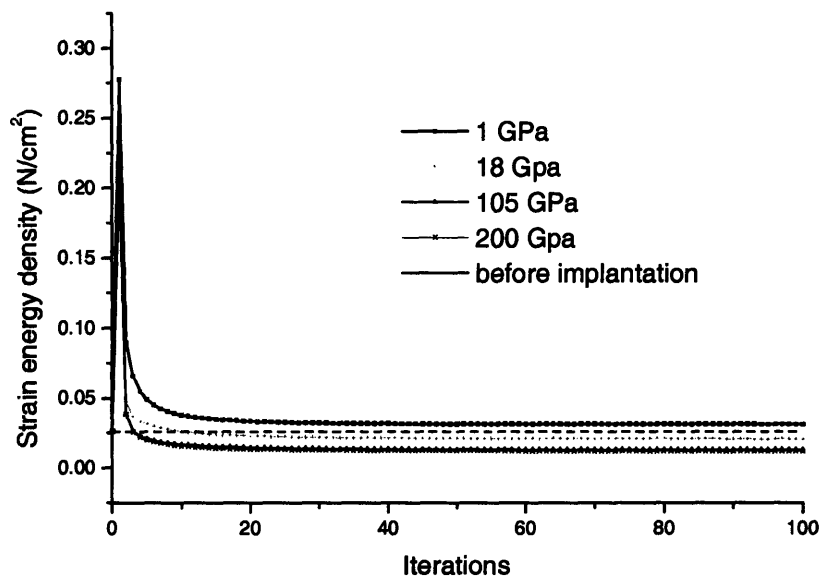

Figure 4-18 Change of SED with implants of different Young's modulus.

125

The strain energy density was calculated based on the fixed total volume. However, in real bone, after implantation, the bone will normally lose some bone mass due to lowered osteoblast activity. So, the fixed total volume assumption is not valid any more once there is an implant. In order to calculate the volume change, a new assumption, that the strain energy density remains fixed but the volume changes, was utilized. The strain energy density E_0 in function (4-4) was simply replaced by 0.026 N/cm^2,

$$\Delta v_i = R v_i (E_i - 0.026) \qquad \text{(4-6)}$$

the value of bone strain energy density before implantation. The system average energy density oscillated around and finally fixed on this value (Figure 4-19). The calculation showed that the total volume dropped dramatically, from 0.023 cm^3 to about 0.016 cm^3 (Figure 4-20), or one third of the bone materials lost due to the implant
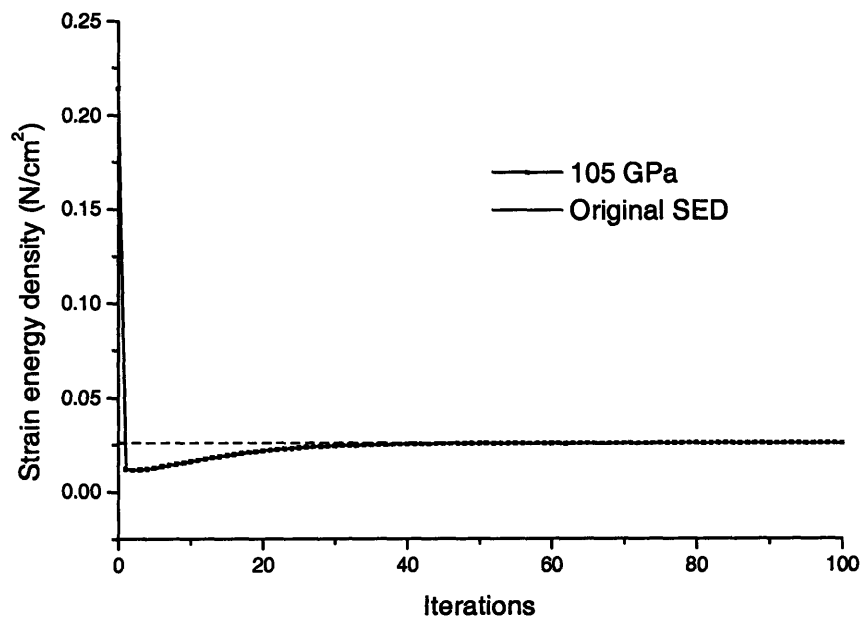
Figure 4-19 Strain energy density vs number of iterations when volume changes.

Figure 4-20 Volume change with iteration time for total hip replacement.

Young's modulus also affected the volume (Figure 4-21). Generally, the higher the Young's modulus, the lower the total volume. For a material with the same Young's modulus as bone, the total volume was still lower than the original volume. A material with Young's modulus between 1 GPa and 18 GPa is required if the original volume is to be kept.

Figure 4-21 The effects of Young's modulus on total volume.
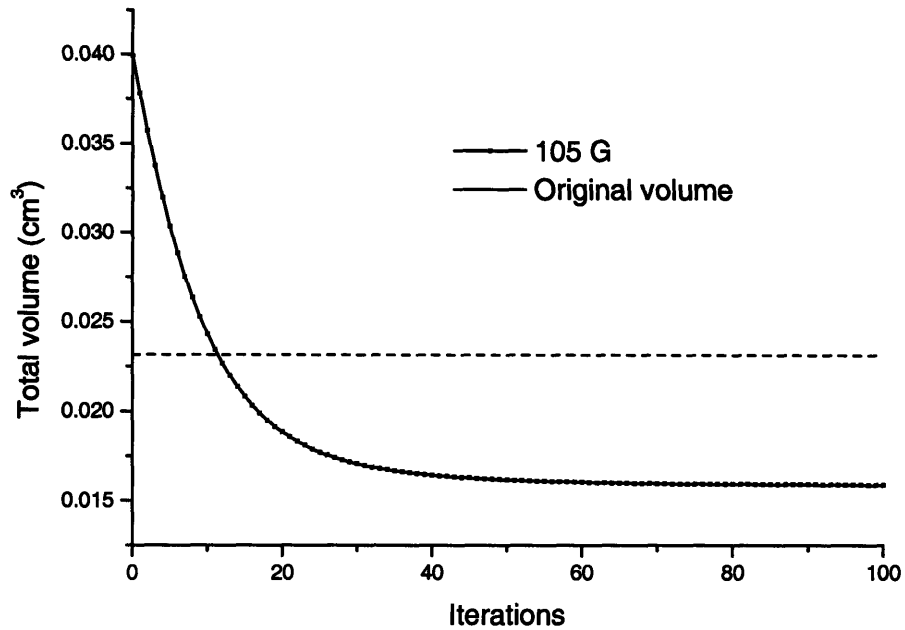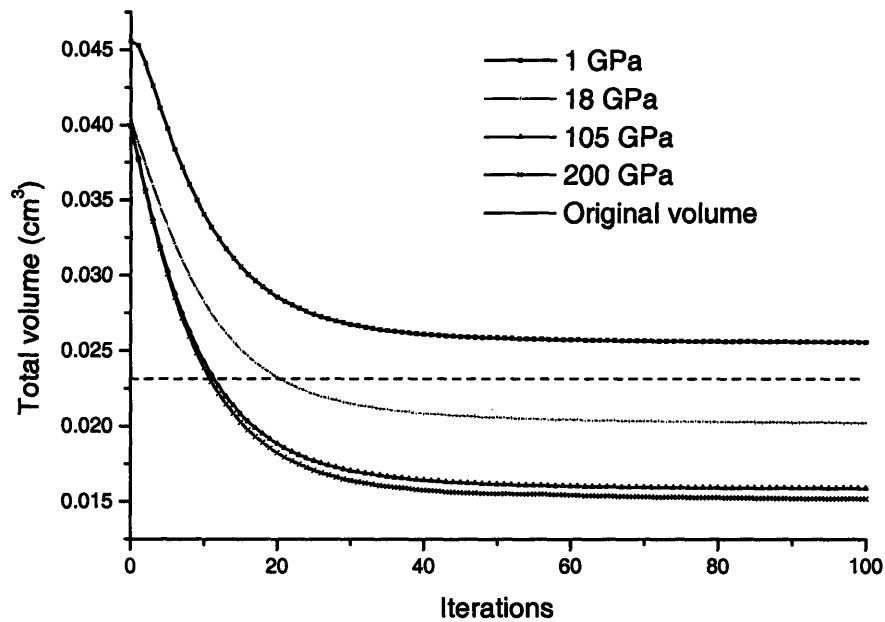
In chapter 2, bone apposition was discussed. Bone exhibits different apposition ratios on different implant materials. A higher apposition ratio means stronger bonding between bone and implants and is always a benefit. However, the question remains whether the apposition ratio affects the strain energy density or total volume after implantation. This question was studied by comparing three different apposition ratios, 50%, 80%, and 100%, in this bone model. The different apposition ratios were realized by forming a bond between the bone and the implant with corresponding probabilities of 0.5, 0.8, and 1.0, respectively. The calculation proved that the apposition did not change the total volume much, at least for apposition ratio higher than 0.5 (Figure 4-22).
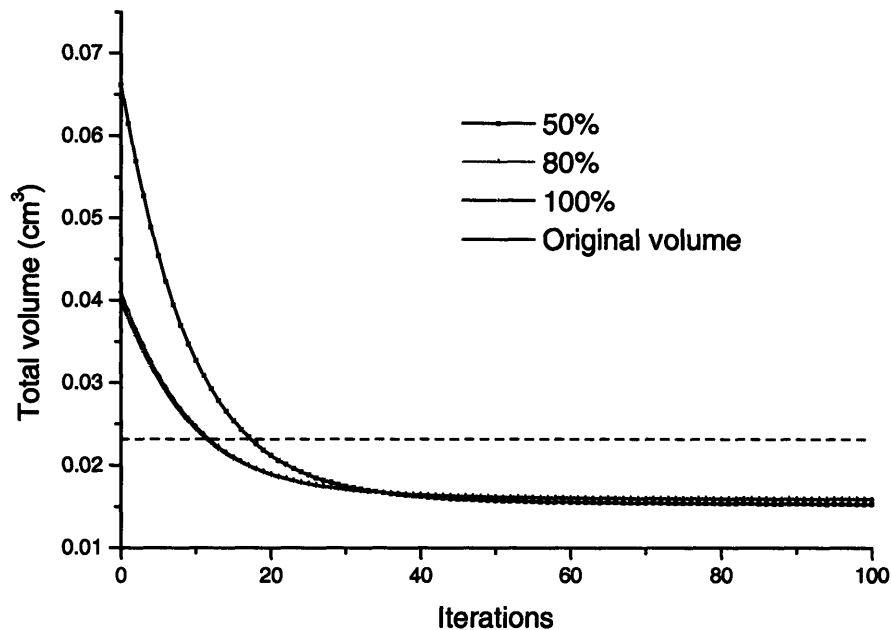
Figure 4-22 The effects of apposition ratio on total volume after implantation.

(2) Hip resurfacing

Hip resurfacing is an alternative for total hip replacement. In hip resurfacing, only the surface layer of femoral head is replaced. The benefit of hip resurfacing is that most of the patient's healthy trabecular bone is left untouched. A second surgery, if necessary, proves much easier in such cases, which is especially important for young patients. Resurfacing implantation was also studied and compared with total hip replacement.

Unlike for total hip replacement, the system average strain density after hip resurfacing was still very close to the original value (Figure 4-23), even when Young's modulus for the implant was 105 GPa, which is much different from that of bone. This means hip resurfacing does not change too much the stress distribution on the bone, so bone structure does not change too much after implantation (Figure 4-24 and Figure 4-25) This result was further evident by comparing the average system strain energy after total hip replacement and hip resurfacing (Figure 4-26).

129

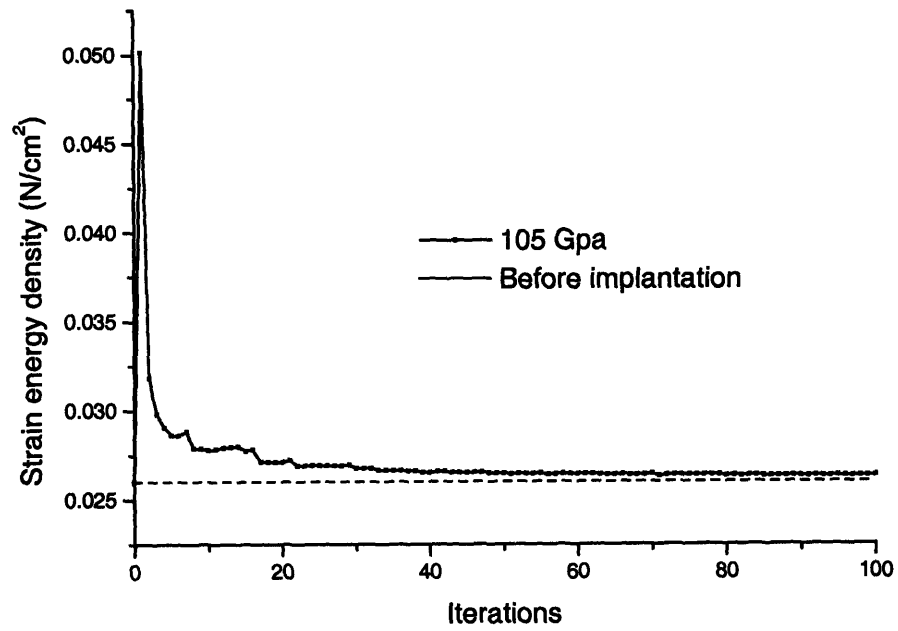**Figure 4-23** System strain-energy density *vs* iteration time when volume changes.
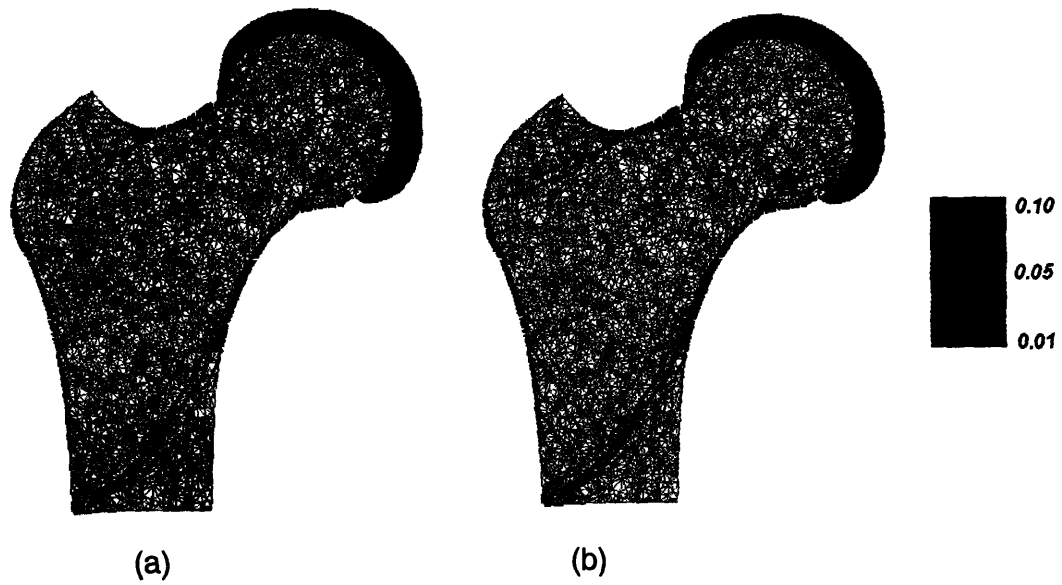

Figure 4-24 Strain-energy density distribution (N/cm²) (a) immediately after hip resurfacing; (b) at a late stage.
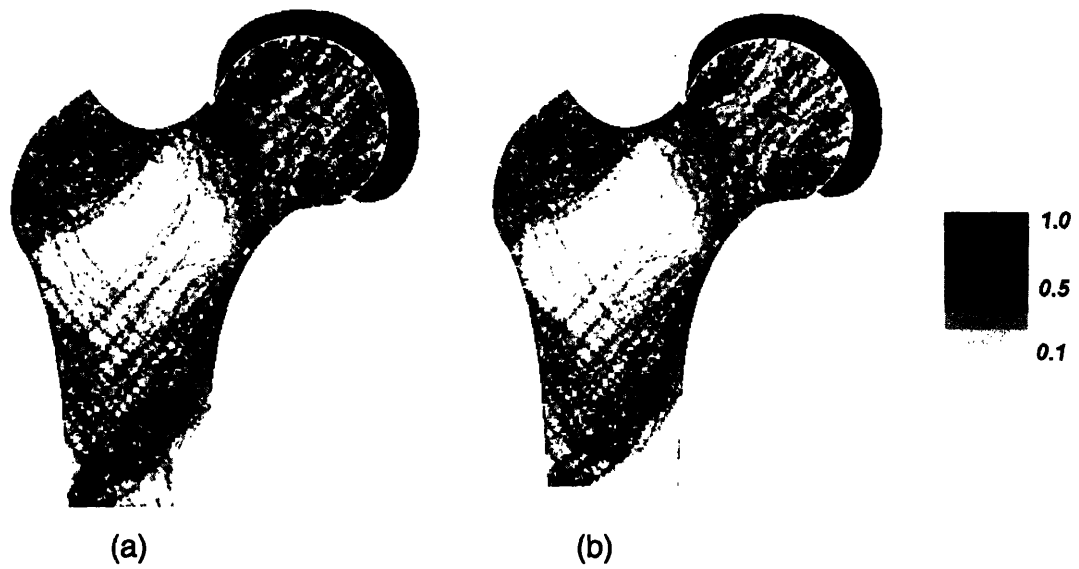
130

Figure 4-25 Strain energy density distribution (a) immediately after hip resurfacing; (b) at a late stage.
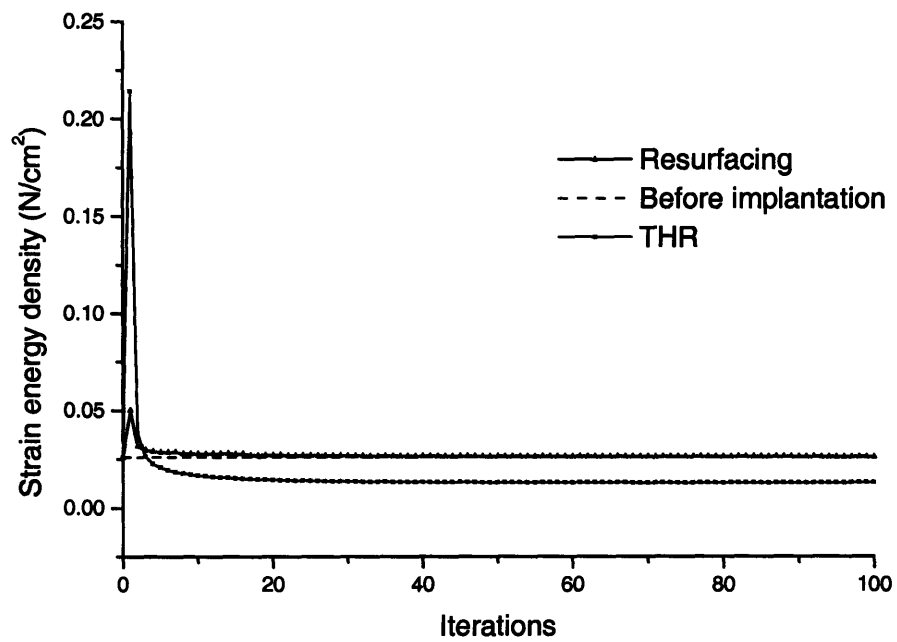
Figure 4-26 Comparison of strain-energy density after total hip replacement and hip resurfacing.

The effects of the implant's Young's modulus are shown in Figure 4-27. It is interesting to see that the best Young's modulus for hip resurfacing is between 105 GPa and 200 GPa, which is much higher than the Young's modulus of bone.
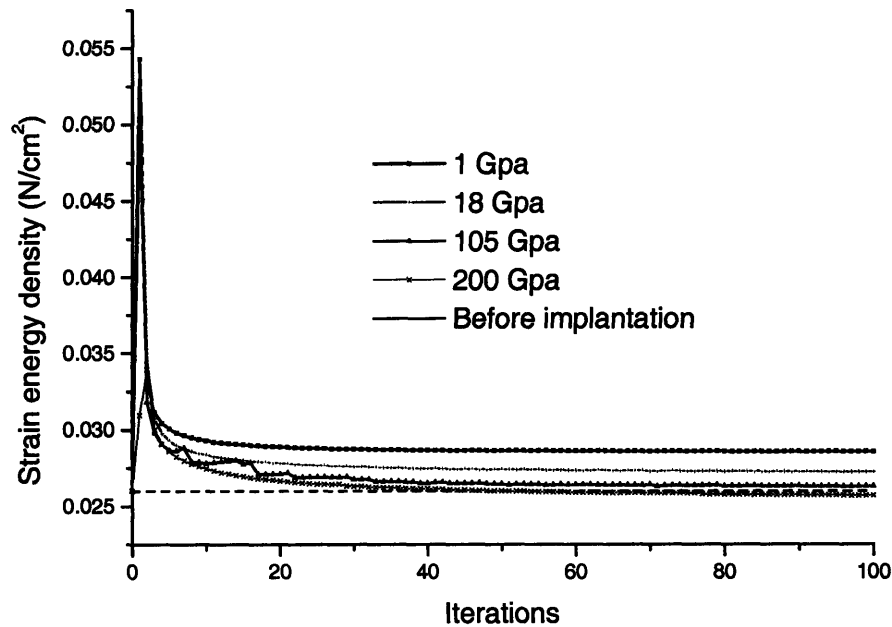
Figure 4-27 The effects of Young's modulus on hip resurfacing.

As in total hip replacement, the volume change after hip resurfacing was also studied by fixing the strain energy density. Figure 4-28 shows that the system average strain energy density stayed at 0.026 N/cm^2 after using the algorithm (4-6). The total volume fluctuated around the original volume but finally converged very closely to it (Figure 4-29). For implants with different Young's moduli, the final total volumes were not very different, and all were close to the original volume. For Young's moduli of 1 GPa and 18 GPa, the volumes were a little higher than the original volume. Again, it can be seen that the material best for hip resurfacing has a Young's modulus between 105 and 200 GPa (Figure 4-30).
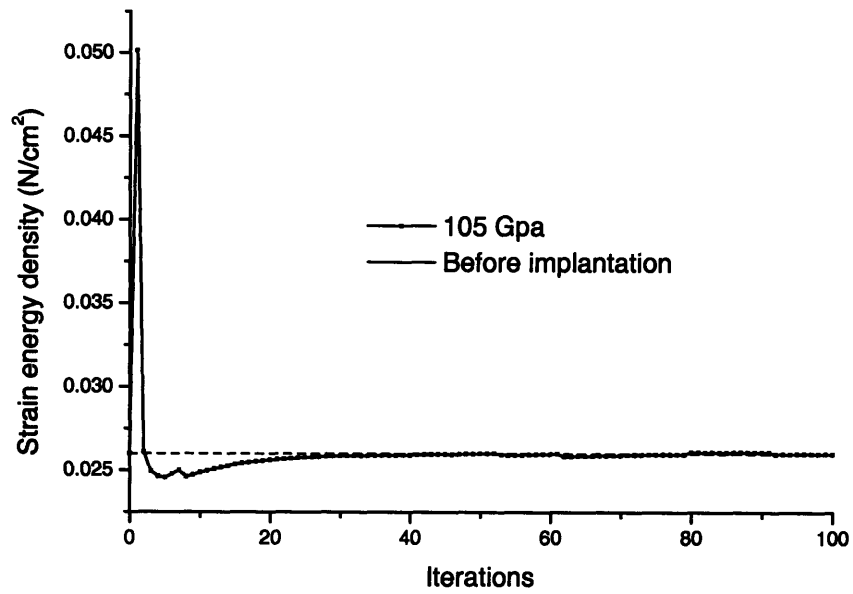
Figure 4-28 Strain-energy density vs iterations after hip resurfacing.
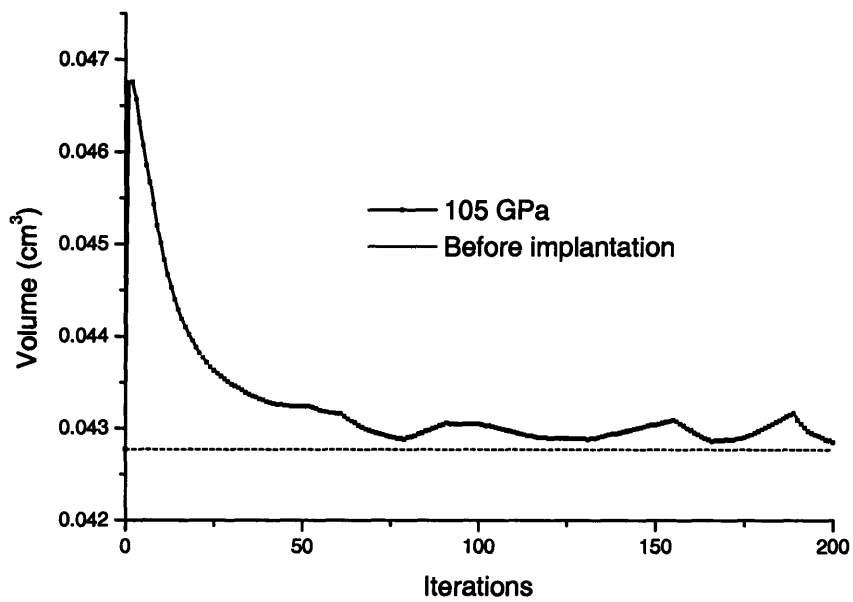
Figure 4-29 The volume change after hip resurfacing.

133
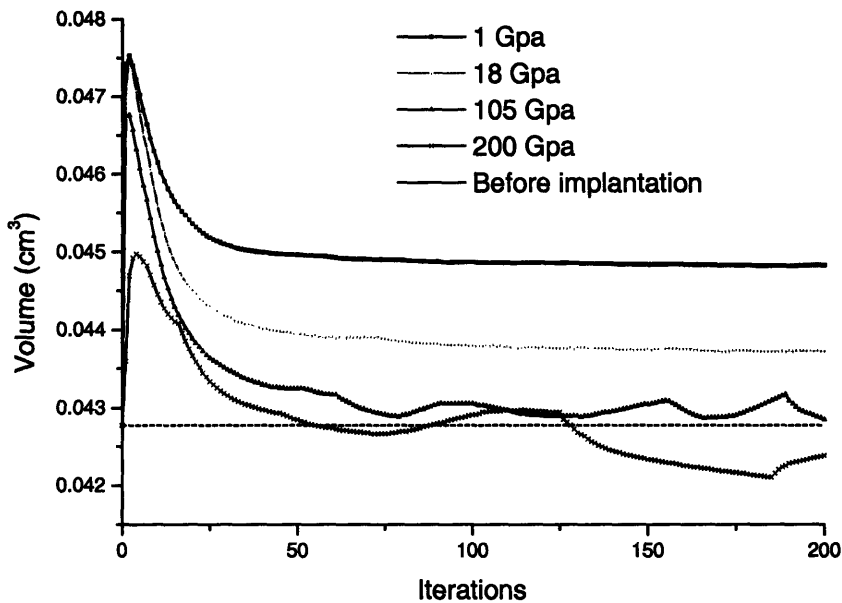
Figure 4-30 The volume change with implants of different Young's modulus.

The effects of different apposition ratios were also calculated. For 80% and 100% apposition ratios, the volumes converged very closely to the original volume. However, for 50% apposition ratio, the volume increased at the beginning, then decreased and converged to the original volume (not fully shown in Figure 4-31).

The strain energy density and bone mass distribution changed little in these three apposition ratios (figures not shown).
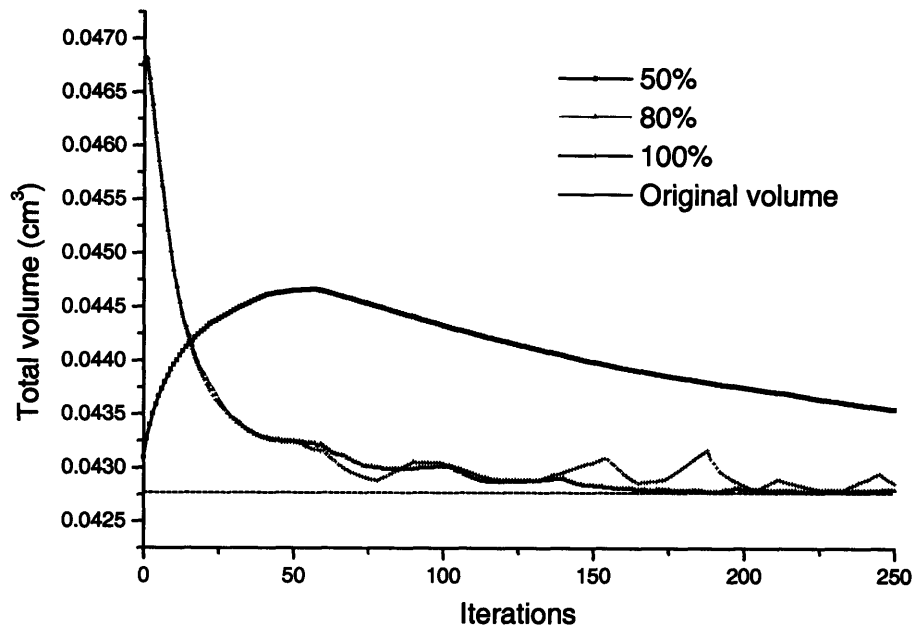
Figure 4-31 The effect of apposition ratio on total volume after hip resurfacing.

4.4. Discussion

The results in this chapter clearly prove that the truss model can be used to simulate bone remodeling. Real bone structure is complex, and it is not possible nor necessary to have a model as complicated as real bone. When studying bone loss caused by implants, only a model which behaves mechanically like real bone is needed. The truss model is simple, easy to calculate, and can be rendered on a scale similar to that of real bone trabeculae. And most important, the truss model is structurally similar to real bone, which makes it different from most continuum models and gives it special value in understanding bone remodeling.

By employing proper algorithms, the truss model can reach an optimal state in terms of minimum system strain energy density. The structure of the bone model at the optimal state resembles that of real bone in that it has a porous interior and dense outer shell. Furthermore, the neighboring truss

135

elements evolve normal to each other, which matches exactly with the arrangement of trabeculae in real bone and proves that Wolff's law, in which bone trabeculae align with local principal stresses, is conceptually correct.

The simulation also shows that total hip replacement greatly changes the stress conduction through bone after implantation. The stress shielding caused by the implant will reduce the activity of osteoblasts, and bone material will be lost. The higher the Young's modulus of the implant, the more bone resorption occurs. However, a material with Young's modulus a little lower than bone could minimize the stress shielding, so that no bone loss will happen.

Compared to total hip replacement, the effect of hip resurfacing on stress conduction is much smaller. The effect of Young's modulus mismatch is also smaller: for the implants with Young's moduli 1 GPa to 200 GPa, the final total volume of bone is similar and close to the value before implantation. Hip surfacing could be a good substitute for total hip replacement, since it entails fewer disturbances to underlying bone structure and can retain most of the healthy trabecular bone.

Despite this modeling progress, improvement is still needed for this model:

(1) A 3-D model would more closely resemble real bone. The same remodeling algorithm still applies for 3-D. However, the triangle elements used for the 2-D model have to be replaced by tetrahedral elements, which can be realized by the three-dimensional successor to the Triangle, Pyramid. Changing from 2-D to 3-D would increase the degree of freedom of each from 2 to 3, and at the same time, 3 order of magnitude more nodes are needed, which would greatly increase the difficulty to converge at each iteration and extend the calculation time. The computer calculation capacity could limit the current application of the 3-D model.

(2) In the ground structure, the position of every node is fixed. Mathematically, this makes the optimization problem (4-1) much easier to solve.

However, the modeling would greatly benefit if the position of each node were also a design variable in the system, which would make the optimization globally but not confined for the ground structure only. Some preliminary trials were made by the author, but were not very successful and hence not described in this chapter. New algorithms are needed to solve this tougher problem.

(3) The calculations need more data from experimental data. The long term purpose of this simulation is to connect with μCT scanning and computer graphic technology to reconstruct real bone architecture, which can predict the bone structure change presenting at surgery and help to design customized implants according to the patient's real bone structure.

4.5. References

1. Huiskes, R., H. Weinans, and B. van Rietbergen, *The relationship between stress shielding and bone resorption around total hip stems and the effects of flexible materials.* Clin Orthop, 1992(274): p. 124-34.
2. Harris, W.H. and C.B. Sledge, *Total hip and total knee replacement (1).* N Engl J Med, 1990. **323**(11): p. 725-31.
3. Huiskes, R., H. Weinans, H.J. Grootenboer, M. Dalstra, B. Fudala, and T.J. Slooff, *Adaptive bone-remodeling theory applied to prosthetic-design analysis.* J Biomech, 1987. **20**(11-12): p. 1135-50.
4. Branson, J.J. and W.M. Goldstein, *Primary total hip arthroplasty.* Aorn J, 2003. **78**(6): p. 947-53, 956-69; quiz 971-4.
5. Huiskes, R., *If bone is the answer, then what is the question?* J Anat, 2000. **197** (Pt 2): p. 145-56.
6. Stevens, S.S., G.S. Beaupre, and D.R. Carter, *Computer model of endochondral growth and ossification in long bones: biological and mechanobiological influences.* J Orthop Res, 1999. **17**(5): p. 646-53.
7. Huiskes, R., H. Weinans, and M. Dalstra, *Adaptive bone remodeling and biomechanical design considerations for noncemented total hip arthroplasty.* Orthopedics, 1989. **12**(9): p. 1255-67.
8. Weinans, H., R. Huiskes, and H.J. Grootenboer, *The behavior of adaptive bone-remodeling simulation models.* J Biomech, 1992. **25**(12): p. 1425-41.
9. Wong, C., P.M. Gehrchen, T. Darvann, and T. Kiaer, *Nonlinear finite-element analysis and biomechanical evaluation of the lumbar spine.* IEEE Trans Med Imaging, 2003. **22**(6): p. 742-6.
10. van der Linden, J.C., J.A. Verhaar, H.A. Pols, and H. Weinans, *A simulation model at trabecular level to predict effects of antiresorptive treatment after menopause.* Calcif Tissue Int, 2003. **73**(6): p. 537-44.
11. Odgaard, A., K. Andersen, F. Melsen, and H.J. Gundersen, *A direct method for fast three-dimensional serial reconstruction.* J Microsc, 1990. **159** (Pt 3): p. 335-42.
12. Feldkamp, L.A., S.A. Goldstein, A.M. Parfitt, G. Jesion, and M. Kleerekoper, *The direct examination of three-dimensional bone architecture in vitro by computed tomography.* J Bone Miner Res, 1989. **4**(1): p. 3-11.
13. Van Rietbergen, B., R. Muller, D. Ulrich, P. Ruegsegger, and R. Huiskes, *Tissue stresses and strain in trabeculae of a canine proximal femur can be quantified from computer reconstructions.* J Biomech, 1999. **32**(4): p. 443-51.
14. Beaupre, G.S., T.E. Orr, and D.R. Carter, *An approach for time-dependent bone modeling and remodeling-application: a preliminary remodeling simulation.* J Orthop Res, 1990. **8**(5): p. 662-70.
15. http://www.qhull.org/.
16. Shewchuk, J.R., *http://www-2.cs.cmu.edu/~quake/triangle.html.*
17. Gibson, L.J., *The mechanical behaviour of cancellous bone.* J Biomech, 1985. **18**(5): p. 317-28.

18.	Cowin, S.C., *Bone mechanics*. 1989, Boca Raton, Fla.: CRC Press. 313 p.
19.	Bendsoe, M.P., *Optimization of structural topology, shape, and material.* 1995, Berlin ; New York: Springer. xi, 271 p.
20.	Zibulevsky, M., Penalty/Barrier Multiplier Methods for Large-Scale Nonlinear and Semidefinite Programming,
21.	http://www.ortho-md.com/totalhip.htm.
22.	http://www.wmt.com/patients/hip/resurfacing.asp.

Chapter 5 Conclusions and future work

5.1 Conclusions

Three types of implants, bare Ti-6Al-4V alloy (Ti64), Ti-6Al-4V alloy with plasma-sprayed hydroxyapatite (PSHA) coating, and Ti-6Al-4V alloy with electro-chemically deposited hydroxyapatite (EDHA) coating, were implanted into canine trabecular bone for 6 hours, 7 days, and 14 days, respectively. The ESEM results showed that, at 7 days after implantation, Ti64 and EDHA implants had a lower bone apposition ratio (30%) than that for PSHA (50%); however, at 14 days, the EDHA and PSHA both had a high bone apposition ratio (70%), higher than that for Ti64 (55%). TEM study confirmed this result: at 7 days, a layer of new bone tissue already apposed PSHA coatings, but there was little new bone formation for EDHA coatings; however, at 14 days, both coatings were covered with a very thick layer (> 1 μm) of new bone. The difference of bone apposition ratio on these two coatings correlates with their differing solubilities, likely due to their morphological difference. It was also observed that the calcium/phosphorus atom ratio of newly formed minerals (7 days on PSHA) was only about 1.20, much lower than that for HA (1.67), which implies that other calcium phosphate phases appear to deposit before the deposition of HA.

Technetium-99m-methylene-diphosphonate (Tc-99m-MDP) labeling was used to quantify mineralization of cultures of MC3T3 osteoblast-like cells *in vitro*. MC3T3 cells were cultured on tissue culture polystyrene (TCPS) in mineralizing and non-mineralizing media, and then labeled by Tc-99m-MDP. The gamma signal from labeled samples was imaged with a gamma camera and compared with the calcium content in the same samples determined by inductively coupled plasma. The high correlation (coefficient of determination, 0.88) between these two values validated the radiotracer uptake method as a quantitative analytical tool for certain mineralization studies *in vitro*. There was an association between mineralization and radionuclide uptake in the MC3T3 cultures on titanium alloy, but the attenuation of the gamma photons by the metal resulted in a less robust

141

correlation. The results warrant implementation of this scintigraphic method for quantitative studies of osteoblast-mediated mineralization *in vitro*.

A 2-D truss finite element model was used to study the remodeling of trabecular bone. Using strain energy density (SED) as the optimization object and the trabecular width as the optimization variable, an optimal structure with minimum SED was achieved. The resulting structure was similar to real bone in the form of a dense outer layer, porous inner layer, and orientation of the trabeculae. The bone density distribution pattern also matched with previous results by other investigators. Different implants were introduced to simulate the replacement for the femoral head. It has been proven by the simulation that the difference in Young's modulus between bone and implant materials is the main reason for the long-term bone loss (stress screening). This problem can be alleviated by proper implant design and resurfacing instead of replacing the whole femoral head.

5.2 Future work

5.2.1 *In vivo* experiments

(1) What is the initial phase for the calcium phosphate deposit? The Ca/P atom ratio of the early mineral nodules is about 1.2, which is less than 1.67, the ratio for HA. So there must be a phase transformation from an early calcium phosphate phase to HA of a renucleation of HA. Mineralization can be observed as early as in 3 days after implantation. What is the Ca/P atom ratio at 3 days? High resolution TEM and convergent-beam electron diffraction might be helpful in identifying these early phases.

(2) Do the early minerals deposit on collagen or other bio-molecules? Immunohistochemistry staining can help to determine whether or not other precursor proteins induce the early mineralization response.

(3) What is the ultrastructure of titanium/bone interface? Fibrous tissue, instead of bone, can form on the titanium surface. It is difficult to preserve an

intact titanium/bone interface during specimen preparation for TEM study using established preparation protocol. But it would be interesting to compare this interface with an HA/bone interface, to see whether and how the calcium-phosphate coating changes the initial bone formation process.

5.2.2 *In vitro* experiments

(1) Ascertain whether Tc-99m-MDP selectively labels newly formed mineral or will also decorate the Ca-P substrate;

(2) Study bone mineralization kinetics, using the Tc-99m-MDP labeling technique to continuously study the same mineralizing sample from early culture to very late stage of mineralization.

(3) Use a higher resolution gamma camera to establish the high-resolution digital images match with images obtained by von kossa staining?

(4) Utilize Tc-99m-MDP labeling to study the effect of different media and culture chemistry on the cell mineralization behavior.

5.2.3 Computer simulation

(1) Erect a 3-D model, in which the mesh is generated 3-dimensionally, using tetrahedra can be used to replace the triangle elements. If the elements maintain the same length scale, there will be around 10^6 elements, which is two orders higher of magnitude than in the current model. A new algorithm would be needed to shorten the computation time.

(2) Investigate new implant designs, especially porous implant designs. By consquently decreasing the stiffness of the implants, the stress screening caused by the difference of mechanical properties between bone and implants could be reduced.

(3) Combine modeling with CT scanning to obtain real bone structure and predict the bone structural changes in patients by this model.

143

Appendix A Electrodeposition of Hydroxyapatite on Ti-6Al-4V

N. Eliaz and T.M. Sridhar

Biomaterials and Corrosion Lab, Dept. Solid Mechanics, Materials and Systems, Tel-Aviv University, Tel-Aviv 69978, Israel

Electrochemical deposition is a potentially attractive process for synthesizing bioceramic coatings from aqueous solutions on metallic implant surfaces. The advantages this technique include good control of coating composition and structure due to the relatively low processing temperature, the ability to deposit on porous or complex shapes, etc. Redepenning and McIsaac have reported that brushite, $CaHPO_4 \cdot 2H_2O$, can be deposited on 316L stainless steel plate or titanium mesh at room temperature from aqueous solutions saturated with $Ca(H_2PO_4)^{2-}$ [1]. Shirkhanzadeh demonstrated that thin carbonate apatite coating films could be deposited on Ti-6Al-4V electrochemically in an aqueous solution, which was prepared by dissolution of hydroxyapatite into 1M NaCl solution adjusted to pH 4.4 by the addition of hydrochloric acid [2]. Shirkhanzadeh later reported that the application of periodic potential pulse may result in uniformly deposited coatings on porous titanium substrates in acidic solution of $CaCl_2$ and $NH_4H_2PO_4$. The formation of nanophase HAP on titanium plates was also noticed at various pH. Moreover, deposits of octacalcium phosphate precipitated from acidic electrolytes along with calcium phosphate phases, consisted of plate-like crystals and deviated markedly from stoichiometry [3,4]. Vijayaraghavan and Benesalem electrodeposited HAP from a tribasic calcium phosphate solution in 1 M NaCl [5]. While only brushite was present following coating at room temperature, both brushite and whitlockite, β-Ca_3PO_4, impurities were present in addition to HAP following deposition at 55°C. Royer and Rey reported that a calcium phosphate film precipitated on a titanium cathode in solution saturated with brushite to which KNO_3 and $NaHCO_3$ were added [6].

The Ti-6Al-4V rods (medical grade) were supplied by MIT. Prior to electrodeposition, the exposed surfaces were mechanically ground on SiC paper P1000 grit (abrasive average size 18 μm), followed by 30-minutes ball milling with alumina particles 1 μm in diameter. The samples were cleaned ultrasonically in acetone. Electrodeposition was carried out by means of a standard three-electrode cell were platinum foil was used as the auxiliary (counter) electrode and saturated calomel electrode (SCE) as the reference electrode. The electrolyte used for the electrodeposition of calcium phosphate coatings was prepared by dissolving 0.61 mM $Ca(NO_3)_2$ and 0.36 mM $NH_4H_2PO_4$, both AR-grade from Merck (Darmstadt, Germany) in Millipore water (Milli-DI™, resistivity > 1 MW·cm). The pH was measured using InoLab pH/Oxi Level 3 meter from WTW and adjusted to 6.0, so that the electrolyte was saturated with calcium and phosphate ions. These concentration and pH values were determined from the solubility isotherm for hydroxyapatite in the ternary system $Ca(OH)_2$-H_3PO_4-H_2O [7]. During the electrodeposition process itself, CO_2-free nitrogen gas (99.999% purity) was continuously purged into the electrolyte to minimize the risk of contamination of the deposits with carbonates. In addition, stirring was carried out by magnetic means. A Lauda Ecoline E-220T thermostatic bath was used to maintain a constant temperature of 85±0.1°C. An EG&G/PAR 263A potentionstat/galvanostat operating in potentiostatic mode was employed to maintain the cathode potential at −1.4 V versus SCE for 2 h.

The structure of a similar batch of deposits was analyzed by X-ray diffraction (XRD). To this aim, a Θ-Θ powder diffractometer from Scintag equipped with a liquid nitrogen-cooled germanium solid state detector and Cu-K$_\alpha$ radiation source (λ=1.5406 Å) was used. The data was collected at a scan rate of 1 degree/min from 20 to 60 degrees. The morphology of the deposits after drying was observed by scanning electron microscope (SEM, Jeol model JSM-6300). The attached energy dispersive spectroscopy (EDS, Oxford Isis system) was used to estimate the Ca/P ratio as well as to identify other elements present in the deposit. Reflectance Fourier Transform Infrared (FT-IR, Bruker model Vector 200) spectroscopy of the coated samples was also used to determine the phosphate vibrations of the deposits.

A typical XRD pattern of HAP electrodeposited on pure titanium is shown in Fig. 1. This pattern was obtained from a sample coated for 2 h at 85°C. The reflections from the deposits were compared to those in the JCPDS file of HAP (#09-0432) as well as to those in the files of other calcium phosphates. No other phase except the stoichiometric, highly crystalline, HAP could be identified. The degree of crystallinity was confirmed based on the resolution of the characteristic peaks of the (002), (211), (112), (300), (202) and (310) plane reflections. In addition, preferential crystal orientation of HAP at the (002) direction is indicated by a sharp peak at ~26°, as previously reported by others for HAP on titanium substrates [5,8]. The lattice parameters of the coated hexagonal phase (a = 9.422 ± 0.002 Å, c = 6.870 ± 0.001 Å) are slightly different from those given in the JCPDS file (9.418 and 6.884 Å, respectively), and the resulting unit cell volume is slightly smaller (528.21 Å^3 for the electrodeposit versus 528.80 Å^3 in the JCPDS file). It should be noted that the apatite in the bone structure is typically needle-like and nano-sized, which results in broadening of the XRD diffraction peaks. However, the US Food and Drug Administration (FDA) requires from submissions for orthopedic and dental endosseous implants that the total crystallinity, as determined from XRD data, will be higher than 62% [9]. The coatings prepared in this work seem to satisfy this requirement.

A representative scanning electron micrograph of the surface of the titanium electrode after electrochemical deposition of is shown in Fig. 2. The outer surface was found to be uniform and free of cracks. The coating consisted of a network of uniformly arranged large granules composed of finer equiaxed nanometric crystals. The Ca/P ratio (for at%) was found to be 1.66 from EDS measurements. These results support the XRD data of formation of only the stoichiometric HAP phase.
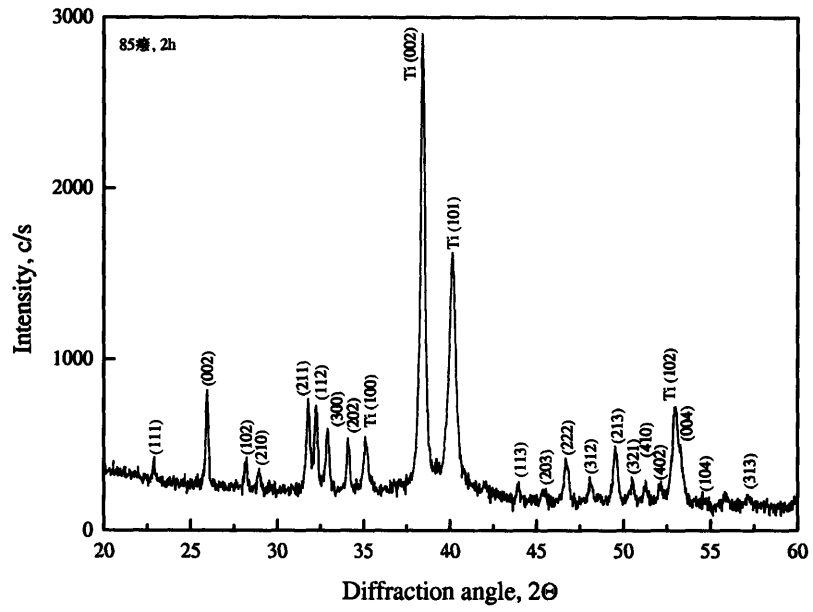
Figure 1. Typical XRD pattern from HAP-coated titanium specimen.

Figure 2. A typical SEM micrograph of HAP electrochemically deposited on titanium.

References

1. J. Redepenning, J.P. McIsaac, Chem. Mater. 2, 1990, 625.
2. M. Shirkhanzadeh, J. Mater. Sci. Lett. 10, 1991, 1415.
3. M. Shirkhanzadeh, J. Mater. Sci. Lett. 12, 1993, 16.
4. M. Shirkhanzadeh, J. Mater. Sci.: Mater. Med. 9, 1998, 67.
5. T.V. Vijayaraghavan, A. Benesalem, J. Mater. Sci. Lett. 13, 1994, 1782.
6. P. Royer, C. Rey, Surf. Coat. Tech., 45, 1991, 171.
7. W.E. Brown, US Patent 4 518 430, 1985.
8. M. Manso, C. Jiménez, C. Moran, P. Herrero, J.M. Martinez-Duart, Biomaterials, 21, 2000, 1755.
9. T.J. Callahan, J.B. Gantenberg, B.E Sands, in ASTM STP 1196: Characterization and Performance of Calcium Phosphate Coatings for Implants (Eds.: E. Horowitz and J.E. Parr), ASTM, Philadelphia, PA, 1994, p. 185